Investigation of electroforming characteristics of TiO_2 based resistance switching devices

submitted in partial fulfillment of the requirements for
the degree of
Doctor of Philosophy
in
Electrical and Computer Engineering

Mohammad N. Noman

B.S., Electrical and Computer Engineering, University of Connecticut
M.S., Electrical and Computer Engineering, Carnegie Mellon University

Carnegie Mellon University
Pittsburgh, PA

January, 2013

Abstract

Resistance switching devices based on transition metal oxides have generated significant research interest over the last decade due to the promise they hold for non-volatile memory applications. Currently they are one of the leading candidates for replacing Flash memory technology as it nears its scaling limits. Despite many years of work and many encouraging demonstrations, the physical mechanism that drives the resistance switching phenomenon remains very poorly understood. A model based on migration of oxygen vacancies is often invoked, however direct proof of this model still remains illusive.

In this thesis, we developed a kinetic model of oxygen vacancy migration. Using this model, simulations were carried out on a 1-D device to examine the resistance switching and retention dynamics. It is found that in order to achieve fast switching (100 ns) and long retention (10 years), the vacancy migration based model requires unrealistic electric field (>10 MV/cm) and temperature (>1500 K) combinations. This situation does not change even when non-linear dependence of vacancy velocity on electric field is taken into account.

A significant portion of this thesis is focused on detailed examination of the electroforming characteristics of TiO_2 based resistance switching devices. Electroforming is a step where a device is electrically stressed in order to trigger permanent changes to the oxide layer. During this process, the resistance of the device is usually lowered by 5-6 orders of magnitude. Stable resistance switching can only be obtained after performing electroforming. Most studies for this work were performed on 5 μm $\times$ 5 μm sized devices with Pt/TiO_2/Pt structure. Transient pulsed method

developed as part of this work allowed for precise determination of the voltage, time, and temperature combination that led to the onset of electroforming. Analysis of the transient data revealed that activation energy associated with electroforming decreases non-linearly with electric field. A vacancy migration based model cannot adequately explain this dependence. The experimental observations are better explained using a hole-injection model which asserts that onset of localized conduction is an electronic process rather than an ion migration based process.

Electroforming often produces pronounced morphological changes to the devices. These morphological changes are a strong function of the voltage pulse amplitude and width used to trigger electroforming. Electro-thermal simulations were used to correlate these changes with transient power dissipation during the electroforming process. The simulations indicate that electroforming did not produce extremely small conductive filaments (10-100 nm diameter) with very small resistance values (100-200 Ω), as it is sometimes reported in literature. Rather, the changes in the resistivity of the TiO_2 layer spanned over an area as large as 8-9 μm^2. Over this region, the resistivity changed gradually over 2-3 orders of magnitude. The filament(s) responsible for resistance switching can be located anywhere within this region.

Acknowledgments

This research work has been made possible by the help and involvement of many people over the course of last several years. I would like to thank my advisor professor James Bain for his support, guidance and encouragement as I have worked towards completing this degree. Since the very beginning he has provided me the flexibility to pursue my own research interests and his mentorship, on both technical and non-technical matters, has shaped my understanding and approach towards this work. I would like to thank professors Marek Skowronski and Paul Salvador for review of my work and many insightful discussions throughout the course of this research project. Also, I am grateful to professor Ed Schlesinger and professor David Ricketts for agreeing to be part of my thesis committee and for their helpful advice that helped me refine the scope of this work.

Many past and present students have contributed to this work. Thanks to Dr. Sukwon Choi, Dr. Wenkan Jiang, Dr. Yimeng Lu, Bryan Tomko, Abhishek Sharma, Ranga Kamaladasa, Dr. Mohamed Abdelmoula, Rozana Hussin, Zacharias George and Cheng-Yuan Wen for help with computer simulation, electrical testing, microscopy, and many fabrication related works. A special thanks to Gregory Slovin for volunteering his time to train me in the cleanroom and for helping me overcome numerous challenges throughout the fabrication process. I would also like to thank Chris Bowman and Carsen Kline of the Carnegie Mellon Nanofabrication Facility for their attentiveness on many matters that ensured smooth progress on fabrication related works.

I would like to thank my parents for encouraging me to pursue this degree. They have made many sacrifices in their lives so that I may have this opportunity and without their blessing and support, I would not be here today. Last but certainly not least, I would like to thank my wife for being by my side during this entire process. Her compassion, love, and support have kept my spirit high through many trying periods as I have worked to complete this degree.

This work was supported in part by the Semiconductor Research Corporation (SRC) under contract 2012-VJ-2247, by the Defense Advanced Research Projects Agency (DARPA) under grant HR0011-06-1-0047 through the Carnegie Mellon MISCIC Center, and by the AFOSR grant FA9550-10-1-0365.

Contents

List of Figures

List of Tables

Chapter 1

Introduction

As computing has moved to more mobile platforms, the need for high performance non-volatile random access memory (RAM) has increased significantly. Traditionally, fast data access has always come at the expense of non-volatility and/or storage density. For example, Dynamic RAM (DRAM) and Static RAM (SRAM) type memory cells are generally used in situations where fast random access is desired. However, both of these types of devices are volatile in nature and storage density is particularly bad in the case of SRAM due to large cell size. Non-volatile and high density storage can be achieved using hard drives where magnetic recording is used, however the inherently sequential nature of read/write operation makes them unattractive for applications where random data access is necessary. Flash memory cells, based on floating gate technology, on the other hand provide both non-volatility and random access capabilities. As a result, despite having 3-4 orders of magnitude slower read/write speed compared to SRAM and DRAM and not being able to achieve similar areal density as hard drives, they are being widely used. Due to the speed limitations, they cannot quite take the place of DRAM or SRAM, however they are increasingly replacing hard drives for mass storage applications.

Despite the ubiquity of Flash memory, this technology is facing serious challenges. Not only that they have relatively slow read/write speed (generally in the range of 100 μs), they require high operating voltages (10-15 volts for write/erase operations), and the endurance of each cell is

generally limited to around 10,000 cycles. It has become clear that this technology will not be able to keep up with CMOS scaling trends in the very near future [1, 2]. As a result, research in alternate non-volatile random access memory technologies have gained significant attention recently. Emerging technologies based on polarization change of ferroelectric materials (FeRAM), spin-transfer torque switching in magnetic tunnel junctions (STT-MRAM), thermally driven phase transition in chalcogenides (PCRAM), and redox reaction and motion of ions (ReRAM) are believed to be some of the most attractive alternative approaches. For all these devices, data storage is a result of existence of multiple stable resistance states. However, the physical mechanism that leads these states and the method for switching between them is very different from one class of devices to the next.

The 2011 International Technology Roadmap for Semiconductors (ITRS) report [3] has highlighted STT-MRAM and ReRAM based devices for accelerated development. According to ITRS projection, it is believed that ReRAM devices will be able to achieve < 10 ns read/write time, $> 10^{16}$ write cycles, < 0.5 V operating voltage, and ≈ 5 nm feature size. Whether all these performance goals will eventually be reached or not remains to be seen, but based on the demonstrations of current generation of devices, this technology seems very promising. In this dissertation, the discussion will be focused on resistance switching and electroforming characteristics of TiO_2 based ReRAM devices. In recent years, some researcher have applied the term 'Memristor' to these devices [4, 5]. This is based on the theory that the resistance states are proportional to the flux of charge passing through the device. Although rigorous proof of such theory remains illusive, many literature reports now refer to ReRAM devices as memristors. These devices generally display two distinct resistance states and electric bias can be used to switch between them. Some ReRAM devices have been demonstrated to possess more than two states [6, 7, 8], and these multiple states can be achieved by controlling the applied bias. Besides non-volatile memory application, these de-

vices hold promise for use in reconfigurable digital circuits [9, 10, 11] and in neuromorphic systems as synapses [12, 13, 14].

1.1 Resistance Switching in ReRAM Devices

ReRAM devices generally have a very simple metal/oxide/metal heterostructure as shown in figure 1.1a. The oxide thickness is usually in the range of 5-50 nm. Over the last few year, many different oxides have been found to display resistance switching characteristics. TiO_2, HfO_2 [15, 16], TaO_2 [17, 18], NiO [19, 20, 21, 22] , $SrTiO_3$ [7, 23, 24, 25, 26, 27], $SrZrO_3$ [28, 29, 30], CuO [31], Fe_2O_3 [32], Al_2O_3 [33], ZnO [34, 35], SnO_2 [36], ZrO_2 [37, 38, 39], SiO_2 [40, 41], etc. are just a few examples of this. Pt, Ti, TiN, and Al are some of the typical metals used for the electrodes. The best way to describe the resistance switching in these devices is through the aid of a schematic current-voltage (I-V) curve as shown in figure 1.1b. Here the curve labeled 'Resistance switching' shows the switching behavior of a typical system with two distinct resistance states. If the device is initially in the low resistance state (LRS), then performing a voltage sweep starting from 0 volts towards the positive direction causes an abrupt increase in resistance once a threshold voltage, ${}^{+}V_{th}$, is reached. The device stays in this high resistance state (HRS) as the voltage is swept back from the positive to the negative direction, and again abruptly switches back to the LRS when a negative threshold voltage, ${}^{-}V_{th}$, is reached. The resistance state of the device can be interrogated as long as the applied voltage is kept below these threshold voltages. This voltage driven hysteretic resistance characteristics serve as the basis for information storage in ReRAM cells. Voltage pulses, rather than continuous voltage sweeps, can also be used to trigger resistance switching as long as the pulse amplitude is kept above the switching threshold values. The threshold voltages for switching is generally found to be in the range of 0.5-2 volts. However, both the threshold voltages and the direction of resistance switching is highly dependent on the properties of the oxide film

and the metals used for the electrodes.

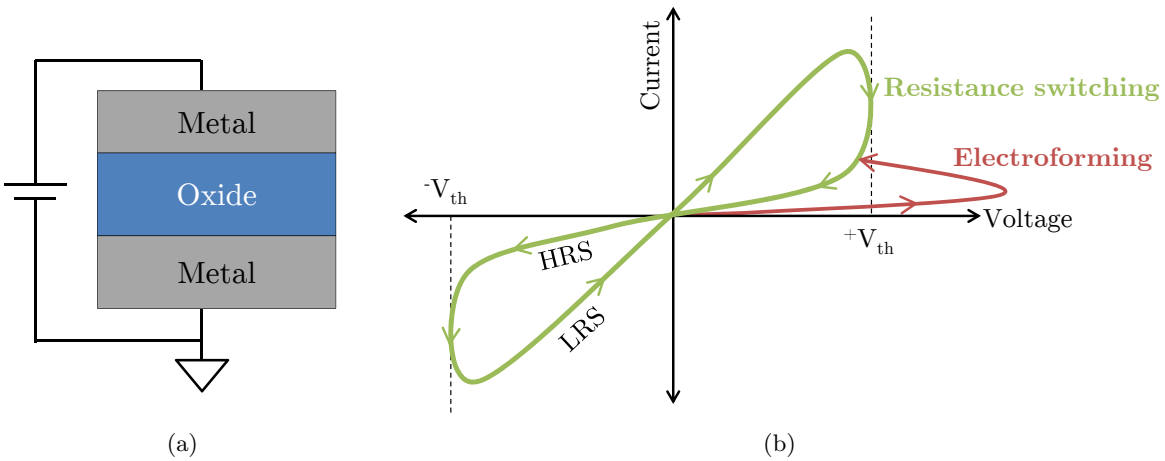

(a) (b)

Figure 1.1: (a) Metal/Oxide/Metal device structure of ReRAM cells; (b) Schematic current-voltage curve of resistance switching and electroforming.

Most ReRAM devices in fact does not exhibit stable resistance switching properties immediately after fabrication. These devices need to go through an initialization process referred to as 'forming', 'breakdown', or 'electroforming'. The I-V behavior of this process is marked as 'Electroforming' in figure 1.1b. During electroforming, a DC voltage sweep is performed where the voltage amplitude is gradually increased until a sudden resistance decrease is observed. This resistance change is often accompanied by localized morphological changes to the device, indicating physical changes to the oxide layer. The voltage at which this breakdown takes place is usually higher than the subsequent switching threshold voltages. For each device, electroforming needs to be performed only once and the resistance lowering that occurs during this step is permanent in nature. Both the HRS and LRS states have lower resistance compared to the initial device resistance prior to electroforming. Electroforming voltage polarity can either be positive or negative, and again is highly dependent of the oxide and electrode properties.

1.2 Hypothesis And Objective

Despite the abundance of resistance switching examples in many different types of oxides, much remains unknown about the fundamental physical mechanisms that drive this process. This is in stark contrast to other types of non-volatile memory technologies such as FeRAM, PCRAM, and STT-MRAM where the physical mechanisms are well understood. For vast majority of ReRAM devices, the resistance switching property is believed to originate from motion of oxygen ions (or vacancies). Oxygen vacancy motion in oxides have been extensively studied for many years [42, 43, 44, 45, 46, 47, 48]. Over the last few years, these studies have been revisited in the context of resistance switching in oxides such as $SrTiO_3$ [27, 49] and TiO_2 [50]. The process is believed to be very similar in other oxide systems as well. Oxygen vacancies act as electron donors and the presence of large concentration of vacancies can significantly alter the electrical conductivity of the oxide. Also, since vacancies are electrically charged, they can migrate within the oxide as a result of externally applied electric field. Moreover, in oxides such as TiO_2, large accumulation of oxygen vacancies can lead to phase transformation which can produce growth of more conductive magnéli phases such as Ti_4O_7.

The objective of this dissertation is to understand the dynamics of oxygen vacancies motion and to investigate the events that are involved during electroforming of TiO_2 based ReRAM devices. A long standing question regarding vacancy migration has been whether this mechanism can lead to memory devices with very fast programming times (on the order of 100 ns) and long retention time (on the order of 10 years) [51]. These times are heavily dependent on the activation energy for vacancy migration. Low activation energy (< 0.5 eV) can enable fast programming times since vacancies can be moved quickly using an electric field, however it will also lead to very small retention time since they will quickly diffuse back to their original configuration after the removal of the electric field. Large activation energy (> 1.0 eV) on the other hand will have the opposite

problem. In order to get around this dilemma, it has been hypothesized that the vacancy migration speed has non-linear dependence on applied electric field [51, 52]. This dependence is so strong that the 15 orders of magnitude difference in programming and retention times can be achieved. It postulates, under low electric field, the vacancies are kinetically immobile, but when the field amplitude is increased, they can move extremely fast. In order to investigate this phenomenon, in this dissertation, a quantitative model of this non-linear electric field dependent vacancy migration will be developed. Using this model, numerical simulations will be performed on a representative ReRAM device to explore the interplay between various parameters that dictate vacancy migration dynamics. These parameters include electric field, activation energy, and temperature. The simulations will quantitatively demonstrate the effect of each of these parameters and interrelationship among them. The extent of non-linearity of vacancy motion induced by these parameters will be examined based on the simulation results.

Another important aspect of resistance switching is the electroforming step described earlier. It is believed that filaments of more conductive phases of oxide form within the device during this step [53, 54, 55, 56]. The hypothesis is that this results from migration of oxygen vacancies as a result of application of large electric field. After electroforming, expansion and contraction of these filaments, again caused by motion of vacancies, produce the resistance switching effect. More details of this process is can be found in chapter 2. In order to gain complete understanding of the physical mechanism behind resistance switching, a thorough understanding of the electroforming process is absolutely necessary. However very few examples of such studies are found in literature. In a recent review paper on resistance switching in TiO_2, Kim *et al.* [53] has mentioned the following about electroforming:

> "Despite the importance of electroforming, systematic studies on it in various resistive switching materials are relatively lacking. ... Electroforming is considered a very complicated phenomenon including many distinct events, such as ionic migration, redox reaction (involving gas evolution) and Joule heating. These events are likely to be inter-

related and somehow synchronized, making it difficult to separate each contribution at this time."

A significant portion of this dissertation will be focused on trying to understand these multiple inter-related events that take place during electroforming. To do this, a systematic study of voltage pulse induced electroforming in TiO_2 based devices will be carried out. Electroforming will be performed using voltage pulses as short as 20 ns to as long as 100 ms. Transient characterization will show the correlation among various parameters such as time, temperature, voltage, resistance, and power. A method of extracting the contribution of Joule heating will be developed. The hypothesis that electroforming involves large migration of oxygen vacancies will be evaluated in terms of these measured values. Also, the evolution of morphological changes as a function of various pulse parameter will be examined. Electro-thermal simulations will be used extensively in order to estimate the spatial extent of resistivity change of TiO_2 layer that occurs during electroforming.

Based on the results of the pulsed electroforming experiments, it will be shown that onset of localized electrical conduction is not triggered by migration of vacancies, rather it is an electronic effect related to charge trapping. The proposed model for electroforming is schematically shown in figure 1.2. As an electric field is applied to a pristine device, Joule heating due to current conduction uniformly increases the temperature of the device. Due to temperature dependent conductivity of TiO_2, the current conduction also increases uniformly. This current conduction through the TiO_2 layer gives rise to trapped charges (most likely holes) which begin to make the electric-field and subsequent current flow non-uniform. However this non-uniformity is not permanent in nature. That is, if the electrical bias is removed, the trapped charges are eliminated, and the electrical conduction behavior of the device is not permanently modified. However, if the charge trapping process is allowed to continue, localized increase in electric field and the current flow will accelerate the trapping process. This high current flow will also create localized regions of high temperature.

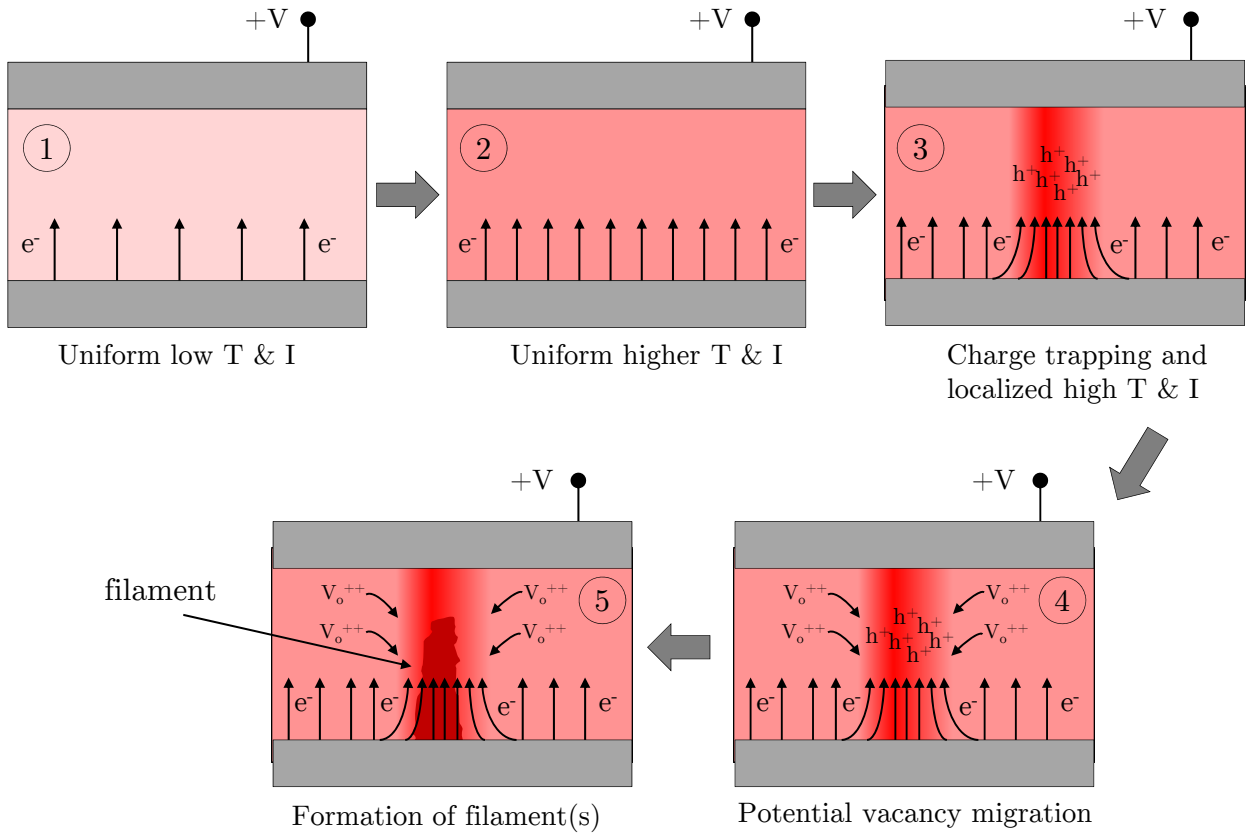

Figure 1.2: Schematic of physical events during electroforming

This self-reinforcing condition will eventually lead to permanent breakdown of the TiO_2 film and create localized morphological changes and conductive filaments that are often observed in TEM images. Oxygen vacancy migration is possible under localized high temperature, electric field, and large temperature gradients. And, it is most likely involved in the permanent filament formation process. However, the initial localization of temperature and electric field is not due to oxygen vacancy migration. This physical picture of electroforming will be verified in chapters 5 and 6.

1.3 Document Organization

The remainder of this document is organized in seven chapters. Chapter 2 provides a brief literature review of various observations related to resistance switching in TiO_2 based devices. Various proposed mechanisms of electroforming and resistance switching are also discussed. In chapter 3,

the fabrication and DC electrical testing results of TiO_2 based cross-bar type ReRAM devices are discussed. A close look is taken at the DC electroforming process that is often reported in literature, and the intricacies and drawbacks associated with this method are highlighted. In chapter 4, a model for oxygen vacancy motion that includes non-linear dependence of vacancy velocity on electric-field is developed. This drift-diffusion based model of vacancy migration is then used to simulated the programming and retention time of a $SrTiO_3$ based device. The main objective of this simulation work is to understand how parameters such as electric field, temperature, activation energy, vacancy ionization level affect the dynamic of vacancy motion. Chapters 5 and 6 are focused on pulsed electroforming studies. In chapter 5, the experimental setup and results from various types of pulsed electroforming experiments are described. The transients associated with electroforming and the effect of subjecting a device to single vs. multiple pulses are examined closely. In chapter 6, a method is presented that allows for extraction of device temperature rise due to Joule heating as a function of time as a result of the power dissipation during electroforming. This extracted temperature is compared with predictions from electro-thermal simulations in order to obtain a precise estimate of the temperature prior to the onset of permanent resistance change. The voltage, time, and temperature relationships are then used to judge several different oxide breakdown models, including the vacancy migration based model. In chapter 7, morphological changes that result from various types of electroforming pulses are examined. The goal of this chapter is to better understand physical extent of the resistivity change of the TiO_2 film across the entire device area. An electroformed device is cut into several pieces in order to get a better understanding of the resistivity change of the TiO_2 film in various regions of the device in relation to the observed morphological changes. Electro-thermal simulations are used to evaluate several conductive filament geometries in order find the most plausible and consistent explanation for all the morphological changes corresponding to various types of electroforming pulses. Finally

in chapter 8, a brief summary of all the findings are presented.

Chapter 2

Overview Of Resistance Switching

Non-volatile resistance switching effect is a commonly observed phenomenon in many different material systems. In most cases, externally the switching effect is controlled by the application of electrical stress. However the exact physical mechanism behind switching varies widely from one material system to the next, including chemical effects, electronic effects, changes in molecular configurations, temperature induced phase transitions, etc. Classification of different types of materials into various groups based on physical mechanism is in general a very difficult task. Due to a very active research community in this field, new material system with unique switching characteristics are often discovered and it is not always clear exactly what physical mechanisms are at play. However, in order to gain a broader perspective on resistance switching and to understand the commonalities among various material systems, classification is necessary. In recent years, some efforts have been made in this regard.

2.1 Classification Of Switching Devices

Waser *et al.* [51], has recently grouped various types of resistance switching devices into several families based on their known/proposed switching mechanisms. While this grouping does not necessarily encompass all possible mechanisms, it greatly helps to frame the discussion about various families of devices. Devices for which switching originates from electronic phenomena, such

as charge trapping/de-trapping [57, 24], polarization reversal, etc. [58], have been grouped under 'Electrostatic/Electronic Effect'. Devices for which resistance switching effect comes about as a result of a switch between crystalline and amorphous phases have been classified as 'Phase Change Memory Effect' (PCM). Besides these two groups, there is a broader class of materials where resistance switching comes about as a result of chemical effects. These have been classified as 'Electrochemical Metallization Effect' (ECM), 'Thermochemical Memory Effect' (TCM), and 'Valence Change Memory Effect' (VCM). Most oxide based resistance switching devices are usually classified under one of these three categories.

The similarity between ECM, TCM and VCM type devices is that all three rely on manipulation of some form of conductive filaments through an insulting oxide layer in order to explain resistive switching. The operation of ECM cells are dependent on electrochemically active metal electrodes where migration of metal cations in response to electrical bias gives rise to the various resistance states. It is believed that metal ions form conductive filaments through the insulating oxide layer and these filaments can be manipulated by the application an electric field. A continuous connection of metal ions between the two electrodes generates the low resistance state, whereas a break in the filament produces the high resistance state. Example of such systems include Ag/Ag-As_2S_3/Au [59] and Cu/SiO_2/Pt [41] based devices.

For TCM cells on the other hand, it is believed that controlled Joule heating during electroforming initiates oxide breakdown which creates the conductive filaments. The reason behind this is attributed to local redox reaction due to motion of oxygen ions (frequency discussed in terms of oxygen vacancies) in a temperature gradient resulting from localized heating. Excessive Joule heating can cause these filaments to rapture and controlled heating can cause them to grow, thereby producing multiple resistance states. In practice, the level of power dissipation in controlled by limiting the current flow through the device during the switching operation. Because of the ther-

mal nature, these devices do not depend on the polarity of the electric bias, and as a result, often referred to as 'unipolar' or 'nonpolar' devices. A very widely studied example of this type of system is NiO based devices [22, 21, 60].

The third and final category is the VCM cell which relies on migration of anions under the influence of electrical bias. Transition metal oxides such as TiO_2, HfO_2, TaO_2 and $SrTiO_3$ [26, 17, 18, 27, 61] based devices are few examples of this type of systems. In these materials, motion of large number of oxygen vacancies in response to applied electric field can lead to significant non-stoichiometry. This can cause filaments of more conductive phases of the oxide to form. The shape and size of these filaments can be modified since the direction of motion of vacancies is dependent on the direction of applied electric field. This gives rise to the resistance switching effect. Because of the voltage polarity dependence, these devices are often referred to as 'biploar' type. The name 'Valence Change' originates from the change of valence of transition metal ions that occur as a result of motion of oxygen vacancies, which generally results in the filaments having higher electrical conductivity than the pristine oxide film.

While these classifications are helpful, they can also be misleading to some degree. This is specially true for the TCM and the VCM type devices. For both of these categories, resistance switching is attributed to redox reaction as a result of motion of oxygen vacancies. The cause of this motion is localized Joule heating for the TCM case and electric field for the VCM case. In practice, rarely can these two effects be separated from each other. This is because application of voltage (or electric field) on most of these devices causes Joule heating. Also, some devices exhibit both unipolar and bipolar resistance switching characteristics depending on how they are exercised. For example, TiO_2 based devices are often reported to exhibit such dual behaviors [62]. In fact, while Waser *et al.* have characterized TiO_2 based devices to be of VCM type, in a more recent review paper Kim *et al.* [53] have characterized them to be of TCM type. Regardless of the trigger

mechanism, the motion of oxygen vacancies is considered to play a major role in resistive switching in TiO_2. The following sections provide a brief review of literature that highlights observations related to resistance switching and the current state of understanding of the mechanism.

2.2 Resistance Switching And Related Observations In TiO_2 Based Devices

Due to recent works by Yang *et al.* [63, 64, 56], Szot *et al.* [50] and others [65, 66, 67, 68], there exists a large number of experimental observations of resistance switching in TiO_2 based devices. As mentioned previously, the device structure is usually a simple metal/oxide/metal stack, with a typical oxide layer thickness of less than 100 nm. While the exact behavior tends to vary depending on the metals used for the top and bottom electrode and the nature of the TiO_2 film, a representative current-voltage sweep of two switching devices are shown in figure 2.1. In this work, Yoshida *et al.* [8] have shown that it is possible to achieve both bipolar (figure 2.1b) and unipolar (figure 2.1c) resistance switching on the same device structure by controlling the compliance current during voltage sweeps. Using the bipolar switching case, they have demonstrated that these devices can be switched using voltage pulses as short as 5 ns for as many as 2×10^6 cycles. Scalability of this type of devices has been demonstrated by Yang *et al.* [56, 69], who have reported devices as small as 50 nm $\times$ 50 nm in size with excellent switching characteristics.

Resistance switching in TiO_2 based devices is often attributed to electrical conduction through filaments that penetrate the film. It is believed that these filaments are created during the electroforming process. Subsequent modification of these filaments as a result of electrical stress gives rise to the resistance switching effect. The physical mechanism behind creation and modification of these filaments will be discussed in the next section.

One of the first evidences that pointed towards the theory of filamentary conduction is signs of localized morphological changes on the top electrodes of the switching devices. Figure 2.2a shows

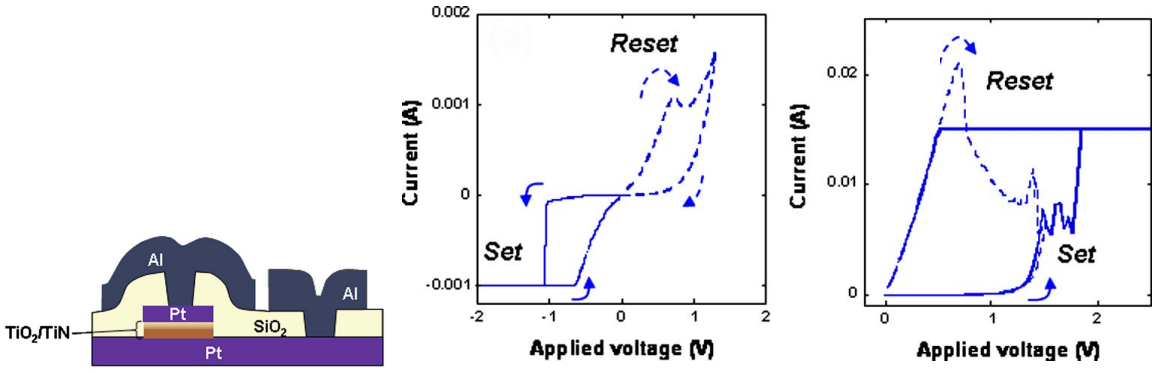

(a) (b) (c)

Figure 2.1: Bipolar and unipolar resistance switching in 20 × 20 μm^2 TiO_2 based devices reported by Yoshida *et al.* [8]; (a) Cross section schematic view showing the Pt top electrode and TiN bottom electrode; (b) Bipolar switching behavior; (c) Unipolar switching behavior.

an example this on a Pt/TiO_2/Pt device [70]. The extent of the morphological changes are usually limited to only a small fraction of the device area. High-resolution transmission electron microscopy (HRTEM) revealed filaments composed of Ti_4O_7 and Ti_5O_9 phases near the areas where morphological changes were first observed [71] (figure 2.2b). These phases have much higher electrical conductivity compared to stoichiometric TiO_2. The diameter of these filaments is estimated to be on the order of 10 nm with a distance between them varying from 0.1 to 5 μm. Filaments of this type were identified over a large region corresponding to the area affected by the morphological changes. The nature of the changes to the electrode metal indicate the possibility of large temperature excursion due to localized power dissipation. Thermal micrography performed by Lu *et al.* [30] on similar devices showed that such morphological changes are indeed associated with localized high temperature regions during resistance switching operation, as shown in figure 2.3. These hot-spots appeared repeatedly during every switching cycle.

In order to investigate the nature of the TiO_2 film under the deformed top electrode, Huang *et al.* [72] performed conductive atomic force microscopy (C-AFM) studies near the morphologically altered region after removal of the top electrode. From the C-AFM scans, shown in figure 2.4,

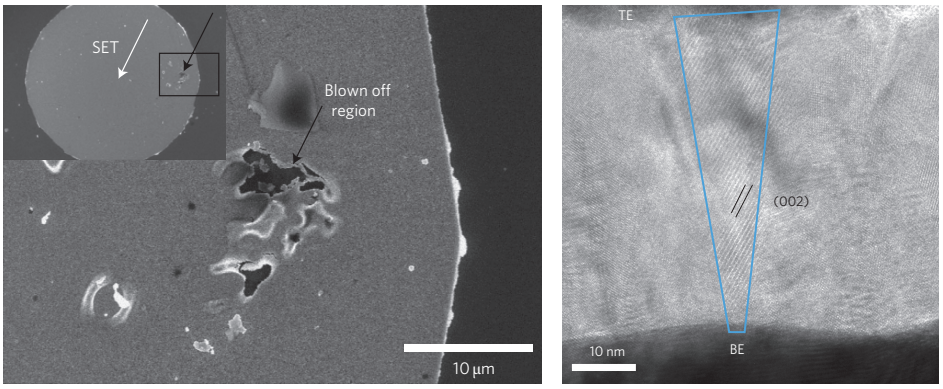

(a) (b)

Figure 2.2: Reported by Kwon *et al.* [70]; (a) SEM images of $Pt/TiO_2/Pt$ based circular shaped devices displaying localized morphological changes; (b) HRTEM cross section image shows cone shaped Ti_4O_7 filament (highlighted in blue).

it is clear that the deformed areas have significantly higher electrical conductivity compared to neighboring undamaged regions, providing further support to the conductive filament theory. In this case, although the affect area is found to be a small portion of the original 100 μm × 100 μm device, the extent of the conductivity change still encompasses a region that is several square microns in size. It is however not clear which portions of this altered region participate in repeatable resistance switching. As expected, once in the switching state, the resistance of this type of filamentary devices have very little correlation with the original size of the device [73, 74]. Together, these observations form the basis of filamentary switching theory of TiO_2 based devices. The switching behavior is dominated by the size and the nature of these filaments.

2.3 Proposed Mechanism

Most transition metal oxides are known to contain certain number of defects such as oxygen vacancies. Creation and transport of such oxygen vacancies have been studied for a long time [42, 75, 76, 77, 43, 44, 47, 48]. It is well known that such vacancies can move within the oxide as a result of concentration gradient, thermal gradient, electric field and other driving forces. Formation of oxygen vacancies is often represented in Kröger-Vink notation as shown in equation 2.1.

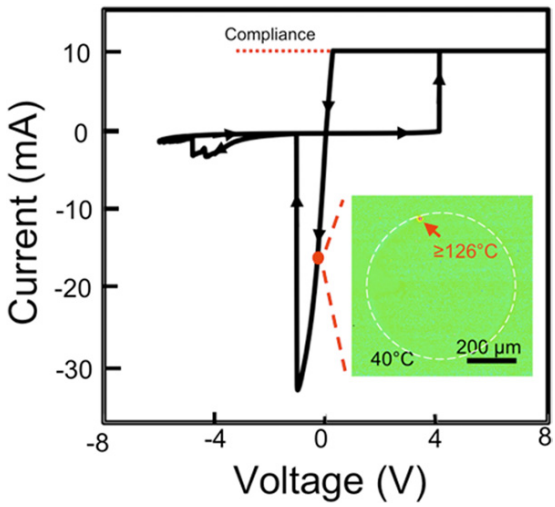

Figure 2.3: Thermal micrograph of a large circular shaped (500 µm diameter) $Pt/TiO_2/Pt$ device. The hot-spot reaches 126 °C during switching indicating presence of localized filaments [30].

Here O_O and $V_O^{''}$ represent oxygen atom at an oxygen lattice site and oxygen vacancy, respectively. Creation of each vacancy produces two free electrons which may change the valance state of the local Ti atoms according to equation 2.2.

$$O_O \rightleftharpoons V_O^{''} + 2e^- + \frac{1}{2}O_2 \tag{2.1}$$

$$Ti^{4+} + ne^- \rightleftharpoons Ti^{(4-n)+} \tag{2.2}$$

Motion of oxygen vacancies play a crucial role in most models attempting to described the mechanism of resistance switching. For devices containing electrode metals that form Schottky type contacts with TiO_2 (such as Pt), it was proposed that modulation of Schottky barrier depletion width, formed at the metal/oxide boundary, due to accumulation and depletion of oxygen vacancies give rise to resistance switching [63, 78]. This process is schematically explained in figure 2.5. Here, the contact between Pt and TiO_2 forms a Schottky barrier. If the concentration of positively charged oxygen vacancies are low at the interface, the depletion width of the barrier is large and therefore the contact displays rectifying current-voltage behavior. On the other hand if vacancies accumulate at

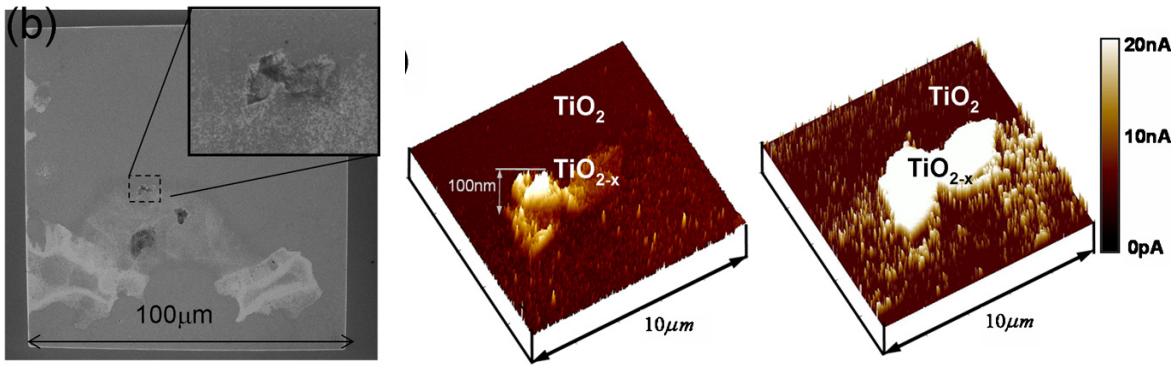

(a) (b) (c)

Figure 2.4: Reported by Huang *et al.* [72] (a) Localized morphological changes on a 100 × 100 μm^2 $Ti/TiO_2/Pt$ device; (b) Surface morphology of the TiO_2 film after removal of the top electrode (corresponding to the region shown in the inset of (a)); (c) C-AFM scan reveals increased conductivity near the regions where morphological changes are observed.

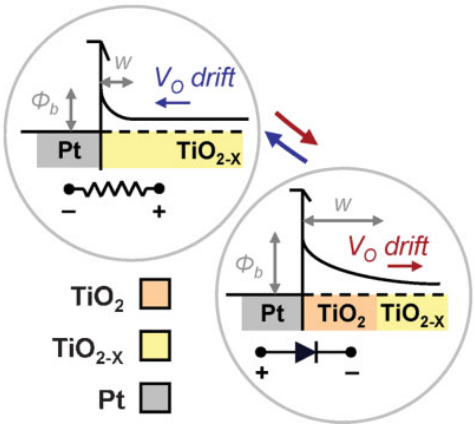

Figure 2.5: Schematic of Schottky barrier modification due to vacancy migration. Thin depletion region (upper inset) produces an ohmic interface and thick depletion width (lower inset) produces a rectifying interface [63].

the interface in response to an applied electric field, this barrier width is reduced significantly. This allows more tunneling current through the interface, and diminishes the rectifying behavior of the junction. Physically, this change in the barrier can occur uniformly over the entire electrode area or in localized regions. This model is consistent with the observation that the I-V characteristics of these devices is rectifying in the high resistance state and non-rectifying in the low resistance state [63].

The switching model based on electric field dependent oxygen vacancy migration raises many

questions regarding the details of this mechanism. For example, can vacancy motion be fast enough to explain resistive switching on the nanosecond time scale? Can this mechanism account for both fast switching and long retention? What happens during electroforming? What is the relationship between conductive filaments and motion of vacancies? What role does temperature play? How can this model explain unipolar switching where polarity of the electric field does not seem to matter?

The question of switching and retention times of these devices have required a closer look at the vacancy migration model. It has been argued that application of large electric fields can non-linearly increase the migration speed of oxygen vacancies by many orders of magnitude [51, 4, 52]. As a result, it may be possible to achieve many orders of magnitude time difference between switching time and retention period. However, the extent to which this justification is applicable at the device level is still open for debate [79]; a larger discussion about this topic is presented in chapter 4.

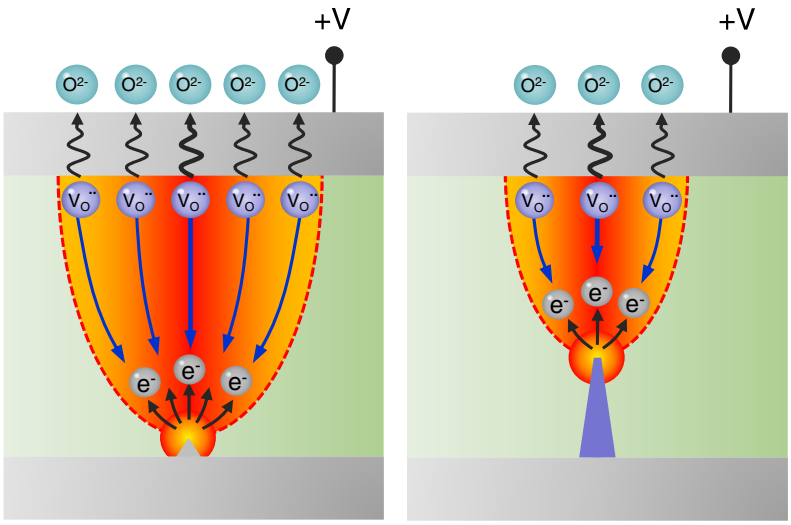

Figure 2.6: Schematic diagrams of electroforming reported by Kim *et al.* [53]; (a) Oxygen vacancies produced at the anode interface migrate towards the cathode due to electric field; (b) Locally high electric field accelerates the filament formation process.

In order to answer the remaining questions, more refinements need to be made to the vacancy migration based model. It is known that as the number of vacancies increase in TiO_2, the existence

of oxygen deficient (and more conductive) phases such as Ti_2O_3, Ti_4O_7, Ti_5O_9 etc. becomes more energetically favorable [53, 50, 80]. These are often referred to as Magnéli phases. Based on the observations of localized heating and growth of these secondary phases, the model for electroforming is schematically illustrated in figure 2.6 [53]. Application of positive voltage to one of the electrodes during electroforming induces vacancy motion towards the cathode. Accumulation of large number of vacancies at the cathode interface initiates nucleation of conductive filaments. The process potentially generates many such filaments over a large area. As these filaments grow, electric field between the tip of the filament and the anode begins to get stronger due to the pointed shape and the reduced gap over which the voltage drop occurs. Stronger electric field and localized Joule heating (due to higher local current density) near the filament area accelerates the movement of the oxygen vacancies. Once few of these filament connect the two electrodes, large power dissipation may occur leading to morphological change. It has been suggested that morphological changes can also occur as a result of oxygen gas evolution near the anode due to the redox reaction in equation 2.1 [71, 72, 81, 82, 54]. The initial nucleation of filaments raises additional questions about the nature of the vacancy migration. If the vacancies migrate in response to an applied electric field, then the accumulation of vacancies near the cathode should be more or less uniform. Under this circumstance, it is not clear how conductive filaments can form only in certain localized regions. Some researchers have suggested that migration of vacancies can be significantly faster along grain boundaries in TiO_2 leading to localized high concentration regions, which in turn results in nucleation of localized filaments [52, 56]. Others have postulated that interface roughness along the TiO_2-metal boundaries may give rise to inhomogeneity in the electric field in various regions of the device, and this can drive the filament formation process [53]. In this thesis, I will show that the initial localization is most likely related to charge trapping rather than migration of vacancies along grain boundaries or surface roughness.

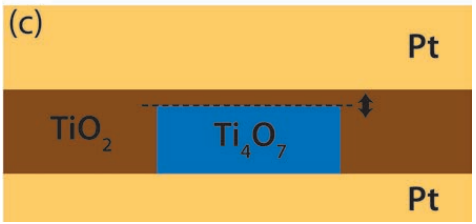

Figure 2.7: The thin barrier between Ti_4O_7 filament and the top electrode can be modified by application of electric field due to motion of oxygen vacancies [55].

Once the filaments are formed during the electroforming step, they can act as source or sink for vacancies during bipolar resistive switching depending on the polarity of the applied electric field. Therefore, repeatable switching only requires small modifications to the filaments generated during the electroforming process as shown in figure 2.7 [55]. Here the filament penetrates the majority of the oxide film except for a very small gap near the electrode. In the figure, the filament is presented as Ti_4O_7, while the gap is shown as TiO_2. However this gap may consist also of magnéli phases with slightly lower electrical conductivity, rather than being stoichiometric TiO_2 [50]. The expansion and contraction of the filament during switching can take place over a gap that is less than 1 nm in size. The exact location of the gap could be anywhere along the length of the filament depending on the growth process during electroforming [68]. While this type of polarity dependent modulation of filament size can explain bipolar resistive switching, a different process is thought to be at play for the unipolar switching. The rupture of a connected filament for unipolar case is assumed be to thermal in nature rather than electrical. Excessive Joule heating due to high power dissipation in the low resistance state partially dissolves the conductive filaments leading to the high resistance state. Since only portions of the filaments are disconnected, subsequent application of electric field can still give rise to localized high current density and Joule heating. Since oxygen ion are likely to migrate away from areas of high temperature, this thermo-chemical reaction can once again reconstitute the disconnected filament(s) in a manner similar to electroforming [53].

2.4 Conclusion

This chapter provides an overview of various observations related to resistance switching in TiO_2 based devices. Observation of morphological changes, appearance of localized temperature increase and existence of conductive filaments have lead to the development of a physical model that relies on motion of oxygen vacancies within the oxide layer. Formation of conductive filaments have been attributed to localized migration of oxygen vacancies due to electric field and Joule heating. Resistive switching, both unipolar and bipolar, has been explained in terms of contraction and expansion of these filaments. Development of these models have largely been driven by observations made after the electroforming and resistance switching events. Due to extreme experimental challenges, nobody yet has successfully observed the growth or modification of these filaments as they occur. Therefore parts of these proposed mechanisms, regarding the dynamics of filament growth and modification, are speculative in nature. Extensive research work over a last 5-8 years have contributed to the growth of a critical mass of information such that the filamentary resistance switching model is generally agreed upon by most researchers. The relative contribution of various driving forces and the nature in which they affect the switching process still remains very much an open area for debate and development.

Chapter 3

Device Fabrication, DC Electroforming, and Resistance Switching

From the literature review presented in the previous chapter, it is clear that TiO_2 based resistance switching devices have been heavily studied over the last few year and yet much remains unknown about the mechanism of operation. The majority of this thesis work is focused on exploring the electroforming process and the associated mechanism of these devices. In this chapter, the design, fabrication, and DC electrical characterization of these TiO_2 based devices will be discussed. The DC resistance switching and electroforming results presented here will provide a general overview of the device behavior. Since this type of experimental results are often reported in literature, they will establish a basis for comparison between these devices and literature reports. An important aspect related to DC electrical characterization is the role of compliance current, which is always employed during DC voltage sweeps in order to prevent current overshoot when the device resistance suddenly changes during electroforming or resistance switching. In most cases, this is accomplished by enforcing a current compliance on the voltage source equipment. A close look will be taken at the transients associated with this compliance process and how it affects the electroforming of TiO_2 based devices.

3.1 Design And Fabrication

Devices fabricated for this study had a metal/TiO_2/metal heterostructure with a crossbar type architecture. A schematic diagram is shown in figure 3.1. The size of the device is defined by the size of the top and bottom electrodes. Crossbars with sizes ranging from 200 nm × 200 nm to 100 µm × 100 µm were fabricated for this work.

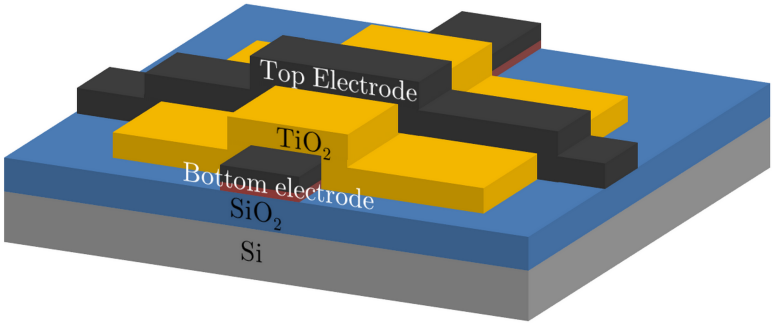

Figure 3.1: Schematic diagram of crossbar device

The process flow for the fabrication of micron sized devices is schematically shown in figure 3.2. All devices where fabricated on Si substrates pre-coated with 1 µm of thermal SiO_2. For the bottom electrode, two layers of metals were used. The first layer was 5 nm thick Ti (for adhesion to SiO_2) and the second was 15 nm thick Pt. Both of these metals were sputter deposited (consecutively, without breaking vacuum in between) at room temperature. These layers were patterned using photolithography and Ar ion beam etching.

After the completion of the bottom electrodes, a 15 nm thick TiO_2 film was deposited using either RF sputtering or atomic layer deposition (ALD) method. For all the sputtered films, a Rutile target was used, the substrate temperature was maintained at 250 °C, and the chamber pressure was kept at 5 mTorr. Some of the sputtered films were deposited under a pure Ar environment and these will be referred to as '0% O_2 film'; here '0%' means that no oxygen gas was used during the deposition. Some films, on the other hand, were deposited under a 80:20 ratio of Ar:O_2 gas mixture, and these will be referred to as '20% O_2 film'. After the completion of the deposition

process, the 20% O_2 films were anneal in vacuum for 3 hours at 250 °C (in the sputter chamber, prior to unloading). No such additional anneal was performed for the 0 % O_2 films. For the TiO_2 films deposited using the ALD process, $Ti(NMe_2)_4$ precursor was used with an O_2 plasma oxidation step. The substrate temperature was maintained at either 100 °C or 200 °C. No post-deposition anneal was performed like the sputtered 20% O_2 film, however the deposition time for the ALD process was significantly longer (3 hours) compared to the sputter process (25-30 minutes). After deposition, photolithography and ion beam etching was used to pattern this layer. Finally, a 20 nm thick Pt top electrode layer was deposited using DC sputtering at room temperature and patterned using photolithography and a lift-off process.

The smallest size crossbar fabricated using this photolithography based process had a size of 5 μm × 5 μm. For devices with smaller size than this, electron-beam lithography was used to pattern the top and bottom electrodes. The metal deposition was performed using electron-beam evaporation (rather than sputtering) and liftoff process was used for both the top and the bottom electrodes. No changes where made to the TiO_2 deposition or patterning steps.

Figure 3.3a shows an SEM image of a large array of these devices. Figure 3.3b shows the large metal pads that connect to the top (pad A) and bottom (pad B) electrodes of each device, which facilitate electrical testing. In addition to these two pads, there is an additional metal pad marked as C. This pad is not connected to either one of the electrodes and it is not used during DC tests. However, for electroforming studies with short voltage pulses, it serves as a return path for the signal as will be discussed in detail in the following chapters. Figure 3.3c shows a magnified view of the crossbar device.

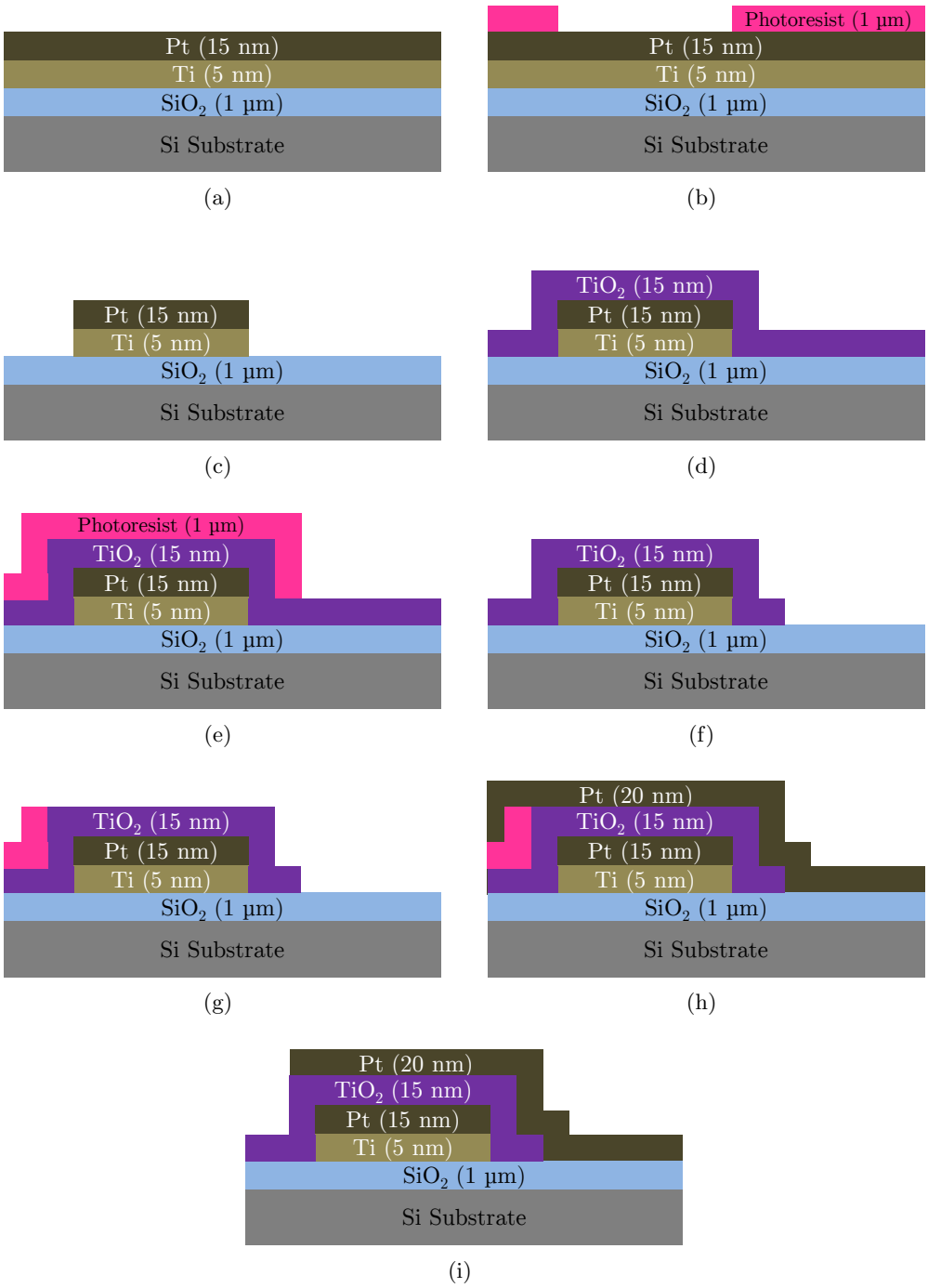

Figure 3.2: Process flow for photolithography based device fabrication. (a) Sputter deposition of Ti and Pt for bottom electrode; (b) Photolithography to pattern bottom electrode; (c) Ion beam etching; (d) TiO_2 deposition (Sputter or ALD); (e) Photolithography to pattern TiO_2 film; (f) Ion beam etching; (g) Photolithography prior to deposition of top electrode metal; (h) Sputter deposition of Pt for top electrode; (i) Lift-off.

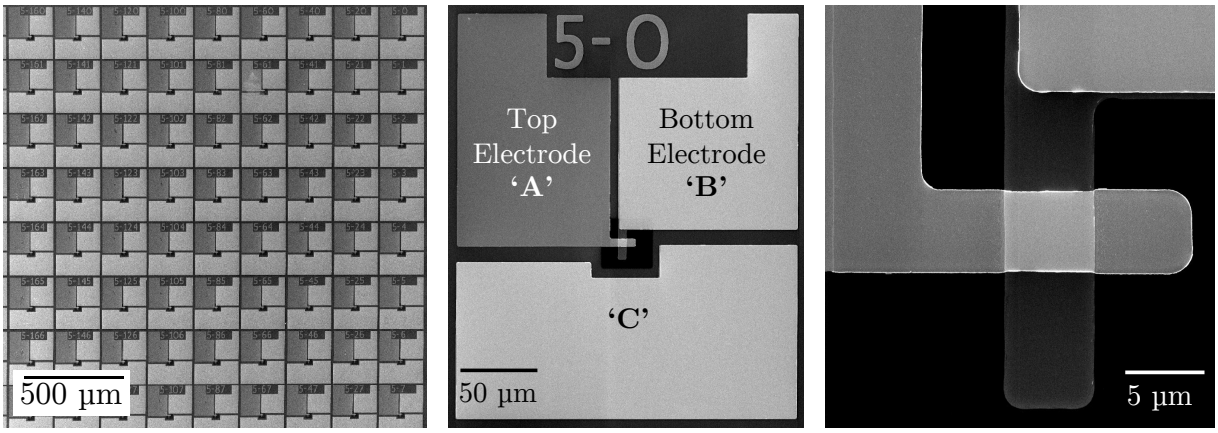

(a) (b) (c)

Figure 3.3: (a) SEM image of a large array of crossbar devices; (b) individual device with contact pads A, B and C; (c) higher magnification view of the 5 µm x 5 µm sized device defined by the intersection of the top (horizontal) and bottom (vertical) electrode traces.

3.2 Electroforming and Resistance Switching

Electroforming and resistance switching experiments were performed on the crossbar devices using DC voltage sweeps. Figure 3.4 compares the current-voltage (I-V) characteristics of pristine (prior to electroforming) 5 µm × 5 µm devices fabricated from the four different types of TiO_2 films discussed in the previous section. All DC sweep experiments were conducted with a Keithley 2400 source-meter. The voltage polarity for all the plots is always in reference to the top electrode (the bottom electrode was the ground terminal). As the I-V sweeps show, for the sputtered films the oxygen content during the deposition process had a large effect on the resistivity of the film. It is difficult to make direct comparison of film resistivity based on the I-V behavior since the current through the device non-linearly depends on the voltage. In general, devices fabricated with 20% O_2 film were found to be 5-6 orders of magnitude more resistive compared to the devices with 0% O_2 film. Generally, sputtered TiO_2 films with 80:20 ratio of Ar to O_2 during deposition produced very resistive films. The 20% O_2 film would have been several orders of magnitude more resistive if the 3 hour post-deposition anneal was not performed (result not shown in the plot). It has been reported

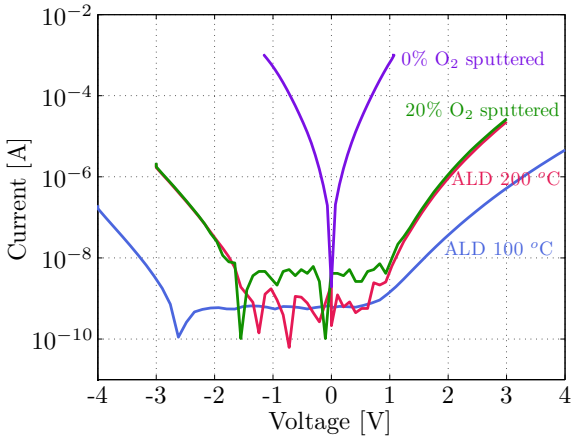

Figure 3.4: Pristine I-V characteristics of 5 μm × 5 μm devices fabricated using four types of TiO_2 films.

that such anneals can change the crystallinity of the film [83] and cause the adhesion layer Ti to diffuse through the Pt bottom electrode and reduce the TiO_2 film [84]. Both of these factors can contribute to reduction of electrical resistivity. Controlling the anneal time was found to be a good method of controlling the resistivity of the 20% O_2 films, although no extensive systematic study was performed to further investigate this matter. For the ALD films, temperature again seemed to play a large role in determining the film resistivity, as the device with TiO_2 film deposited at 200 °C had more than one order of magnitude lower resistivity compared to the device with film deposited at 100 °C.

Figure 3.5 shows the electroforming and resistance switching behavior of 5 μm × 5 μm sized devices for these four types of TiO_2 films under DC voltage sweep. A current compliance was enforced during both electroforming and resistance switching in order to prevent excessive power dissipation when the device suddenly transitioned to a low resistance state. 10-15 devices were tested for each type of film. Devices based on 200 °C ALD films and 20% O_2 sputtered film exhibited the most consistent switching behavior. These devices could be reliably electroformed and switched for many cycles. Although switching was also observed on the more resistive 100 °C ALD film, the switching characteristics were generally quite unreliable. Most devices either never

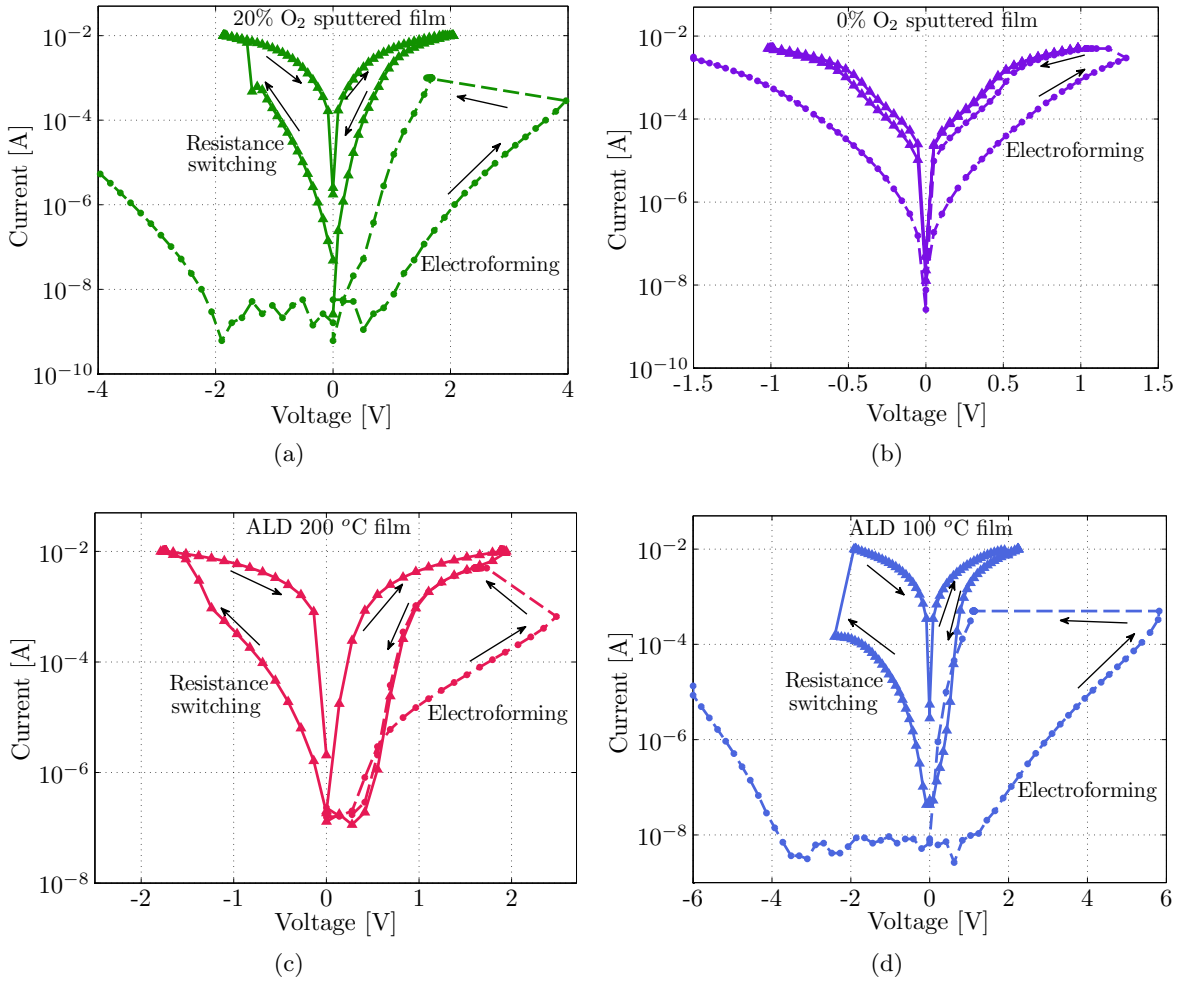

Figure 3.5: Electroforming and resistance switching using DC voltage sweeps. Device size is 5 μm × 5 μm for all cases. The devices were fabricated using four different types of TiO_2 films. (a) 20% O_2 sputtered film; (b) 0% O_2 sputtered film; (c) 200 °C ALD film; (d) 100 °C ALD film.

switched or only switched for 1-2 cycles. The devices based on 0% O_2 film were the only ones that did not exhibit any switching at all. After electroforming, they were found to be permanently stuck in a very low resistance state. However, this may be due to high current through these relatively large size devices. When smaller 200 nm × 200 nm devices were fabricated using this 0% O_2 sputtered film, stable resistance switching was obtained as shown in figure 3.6.

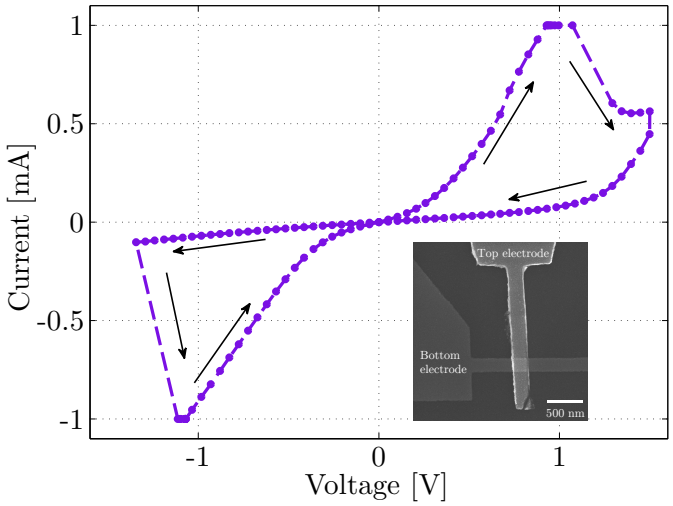

Figure 3.6: Resistance switching in a 200 nm × 200 nm crossbar device fabricated using 0% O_2 sputtered film. Inset shows the SEM image of the device

3.3 Transients Associated With Electroforming

The electroforming and resistance switching curves shown in figure 3.5 give the impression that the compliance current enforced by the source-meter prevents current overshoot from occurring when the device resistance suddenly decreases. In general, if the meter detects that the current through the circuit is higher than the set compliance value, it will lower the output voltage in order to ensure that the current stays at or below the maximum limit. However, capacitance associated with the device itself and the experimental setup (cables, probes, and such) will cause electrical discharge through the device as soon as there is a sudden decrease in resistance. Also, detection of the current overshoot condition and the subsequent reduction of the supply voltage cannot be performed infinitely fast. How fast these things take place depends to a large extent on the internal sensing mechanism of the source-meter.

In order to measure the transients associated with current compliance during electroforming, a resistance switching device was connected in series with a 330 Ω resistor and an oscilloscope was used to monitor the voltage across this resistor during the course of the electroforming voltage sweep.

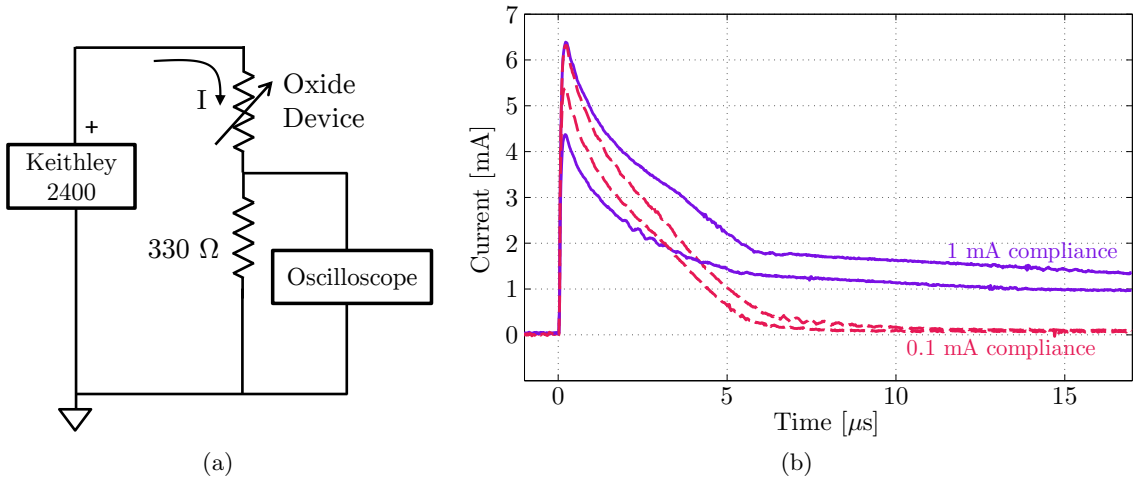

(a) (b)

Figure 3.7: (a) Circuit diagram for transient current measurement; (b) Current overshoot in devices immediately proceeding electroforming. All four devices used for this experiment was 5 μm × 5 μm in size. For two devices the compliance was set to 0.1 mA (red dotted curves), and for the other two the compliance was set to 1 mA (magenta solid curves).

The circuit for this setup is shown in figure 3.7a. The oscilloscope was setup such that acquisition was triggered as soon as there was a sudden change in voltage across the 330 Ω resistor, indicating a resistance decrease of the device. Since the voltage across a known resistor was capture, this allowed for calculation of the current through the series circuit. This experiment was repeated on multiple devices using two different compliance currents values (0.1 mA and 1 mA). The resulting current transients are shown in figure 3.7b for two devices for each compliance current value. Here time equal to 0 s corresponds to the moment when the device goes through a sudden change in resistance. In most cases the current is much higher than the compliance value for at least 5 μs. In some cases, the time it takes to reach the compliance value is longer than 15 μs. This time scale is heavily dependent on the compliance setting and the magnitude of the resistance change. The maximum overshoot current is only limited by the total series resistance. For this experiment, this resistance is the series combination of the device resistance and the 330 Ω resistor. When electroforming is performed without any series resistor, the current would be only limited by the device resistance and therefore the overshoot could be even larger than what is seen in these plots.

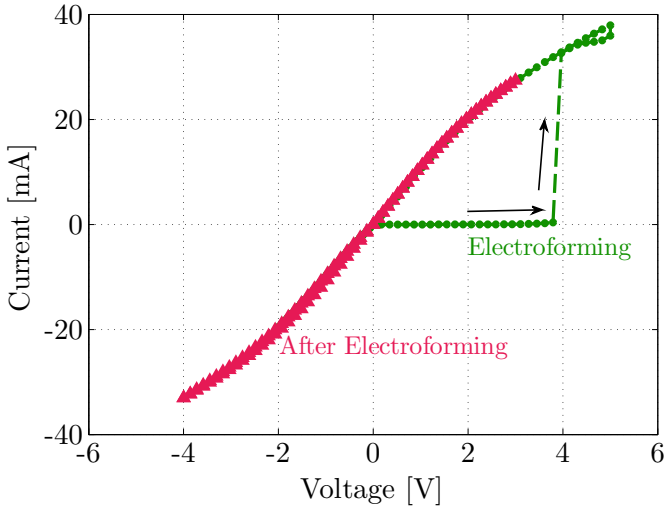

Figure 3.8: DC electroforming of a 5 µm × 5 µm sized device without current compliance. The current exceeds 30 mA during electroforming (green curve), and subsequent DC voltage sweep fails to show any signs of resistance switching (red curve).

Since figure 3.7 shows that current compliance is ineffective for the early portion of the electroforming process, a valid question to ask is whether such a compliance is at all necessary? The short answer to this question is: yes. Figure 3.8 shows an example of electroforming where current compliance was completely removed (by setting it to an extremely large value). Removal of compliance resulted in complete electrical breakdown of the device and no subsequent resistance switching was observed.

There is no doubt that current compliance plays an important role in DC electroforming and resistance switching. Obtaining stable resistance switching on a given TiO_2 film often requires first finding a suitable electroforming and switching 'recipe', where the proper compliance values need to be discovered. This often boils down to simple trial and error process during the course of which many devices are usually destroyed. Part of the problem arises from the fact that enforcement of a current compliance does not really control the actual current overshoot, rather it indirectly controls how fast that overshoot is brought under control. This transient depends on the device resistance, experimental setup, and the control circuits within the voltage source. As soon as one

of these variables changes, one needs to restart the whole process. This DC electroforming method is effective and can work reliably once a suitable recipe is found. However if the goal is to learn more about the processes that drive electroforming, then this method provides almost no useful information.

3.4 Conclusion

The DC resistance switching experiments performed on crossbar devices of various sizes show that the resistivity of the TiO_2 film plays a large role in determining the switching properties of the device. If the film is too conductive or too insulating, the ability to obtain reliable resistance switching diminishes greatly. Resistivity of sputtered films can be controlled by performing a post deposition anneal step, whereas the resistivity of the ALD films can be influence by controlling the deposition temperature. Transient study of the DC electroforming process show that enforcing a current compliance does not prevent current overshoot from occurring during electroforming. These transients current spikes can be tens of microseconds long depending on the experimental setup. Although the compliance setting does not affect the magnitude of the current overshoot, it reduces the time scale over which the devices experience this overshoot. It keeps the devices from being permanently damaged, however it is an imprecise method of controlling the electroforming process.

Chapter 4

Modeling The Dynamics Of Oxygen Vacancy Motion

The switching mechanism of resistance switching devices based on $SrTiO_3$, TiO_2, and other oxides discussed in Chapter 2 relies on motion of oxygen vacancies in order to achieve the modulation between several different resistance states [51, 27]. It is possible to achieve a large redistribution of vacancies within these oxides under an electric field [85]. Although, fast switching and long retention time have been experimentally demonstrated on some devices, the argument for vacancy motion as the mechanism behind it has been mostly qualitative in nature [8, 32]. The goal of the modeling work presented in this chapter is to determine whether a realistic operational window for data storage is attainable through this mechanism alone.

To be competitive with existing memory technologies, RRAM devices must switch in less than 100 ns and retain the programmed state for at least 10 years. Therefore, we must establish whether this 15 orders of magnitude time difference between programming speed and retention time is obtainable when vacancy motion alone is at play. Waser *et al.* [51] have argued that a simple isothermal field-driven redistribution of vacancies, assuming electric field-independent mobility, will not result in dramatic distinction between switching and retention times; this has been labeled as the "Voltage-Time dilemma". Though several arguments have been proposed to overcome this issue, including field-dependent mobility coupled with thermal events during switching [63, 51, 27],

the extent to which such effects can be applied to achieve the figures of merit of memory devices required is not immediately clear.

The physical model presented here will allow us to examine the dynamics of vacancy motion and to explore the interplay of various key governing parameters, such as temperature, applied and built-in electric fields, vacancy mobility, and its activation energy. The model presented here is applied to a 1-D system where no lateral inhomogeneity of vacancy concentration or migration is significant. This type of model is directly applicable to non-filamentary type devices where resistance switching is not laterally localized to any specific portion of the device area. However, the dynamics explored here is equally applicable to filamentary devices where vacancy motion is still considered to play a dominant role behind formation and dissolution of filaments. In the subsequent sections, details of the model and the method of applying it to simulate a 1-D device will be discussed. Simulation results will be presented that will show the effect of temperature, activation energy, and electric field. The role of secondary effects such as double ionization of vacancies, electromigration, local electric field, etc., that may affect the dynamics of device operation will also be discussed.

4.1 Vacancy Migration Model

The model presented here focuses on a Metal(M1)/Oxide/Metal(M2) type resistance switching device where the deep work function of M1 forms a Schottky interface with the oxide layer due to work function mismatch. This metal interface also blocks transport of ions such as oxygen vacancies, which are mobile and serve as electron donors in the oxide layer. Several recent reports indicate that the effective Schottky barrier height can be modified by an externally applied voltage that induces oxygen vacancy motion inside the oxide [63, 27, 49, 73, 86]. Since ionized vacancies are positively charged, their accumulation near the interface reduces the width of the Schottky barrier depletion region (Fig. 4.1b), whereas a depletion of vacancies has the opposite effect (Fig.

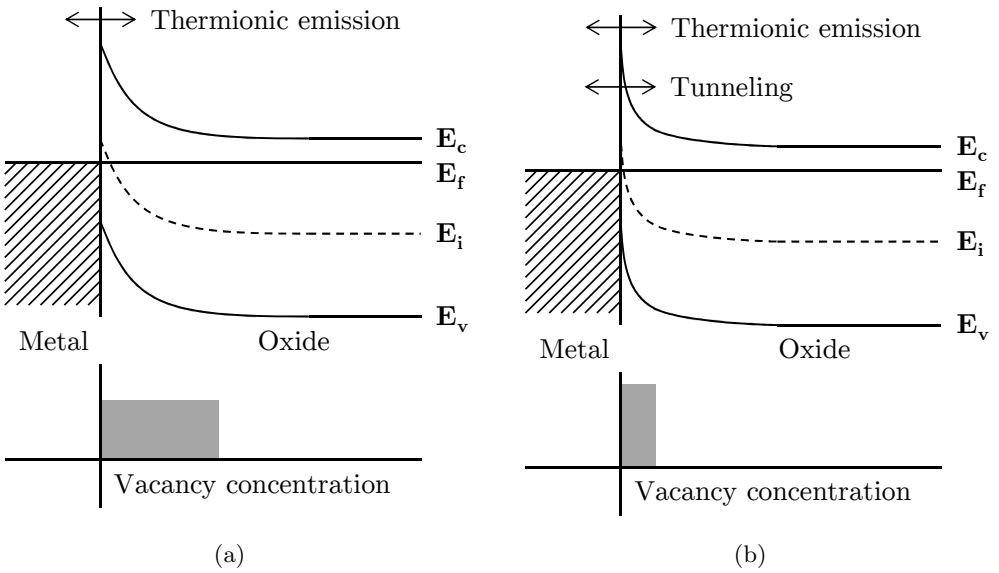

Figure 4.1: Modification of energy barrier at the Schottky interface as a result of accumulation or depletion of oxygen vacancies; (a) Low oxygen vacancy concentration near the metal oxide interface increases the Schottky barrier depletion width, resulting in negligible tunneling current, giving rise to the high resistance state; (b) Increase in vacancy concentration reduces the depletion area, allowing more tunneling current and leading to the low resistance state.

4.1a). This, in turn, modulates the tunneling current through the barrier, resulting in the observed resistance change effect.

The model consists of four main equations. The first three of the four equations are commonly used for semiconductor device modeling, which are the Poisson's equation (Eq. 4.1) and the continuity equations for electrons (Eq. 4.2) and holes (Eq. 4.3).

$$\nabla \cdot (\varepsilon_r \varepsilon_o \nabla \psi) = q\,(p - n + N_D) \tag{4.1}$$

$$\frac{\partial n}{\partial t} = \frac{1}{q}\nabla \cdot (q\mu_n n\xi + qD_n \nabla n) \tag{4.2}$$

$$\frac{\partial p}{\partial t} = -\frac{1}{q}\nabla \cdot (q\mu_p p\xi - qD_p \nabla p) \tag{4.3}$$

In the above equations, ψ is the voltage, ε_r is the relative permittivity of the oxide, ε_o is the free

space permittivity, q is the unit of electronic charge, n, p, and N_D are respectively the electron, hole, and ionized donor concentrations, ξ is the electric field, $\mu_n(\mu_p)$and $D_n(D_p)$ are the electron(hole) mobility and diffusion constants, respectively. For the electron (Eq. 4.2) and hole (Eq. 4.3) continuity equations, only the drift and diffusion currents are taken into account. Effects such as trap-assisted-tunneling or the thermal generation-recombination of carriers are ignored. The term "ionized donors", N_D, in equation 4.1 is used to refer to oxygen vacancies in the oxide layer; and all oxygen vacancies in this model are considered to be singly ionized and therefore carry a charge of +1 [87]. To account for the time dependence of the vacancy motion, equation 4.4 below is used.

$$\frac{\partial N_D}{\partial t} = -\frac{1}{q}\nabla \cdot J_{N_D} \tag{4.4}$$

Here, J_{N_D} is the vacancy flux, which was modeled by a standard lattice-site hopping model, shown schematically in figure 4.2a. The hopping probability of an oxygen vacancy from one lattice site to the adjacent available one, an α distance away, is exponentially dependent on the activation energy barrier, E_a, between the two sites. However, since the oxygen vacancy is positively charged, under an electric field, this energy barrier can be skewed in the direction of the electric field by $\xi q\alpha$ as shown schematically in figure 4.2b. In this expression q represents the charge of the oxygen vacancy which is singly ionized with +1 charge. considering the forward and backward hopping rates, using a Boltzmanns distribution, the expression for vacancy flux, J_{N_D}, can be expressed as shown in equation 4.5.

$$\begin{aligned} J_{N_D} = &\frac{1}{2}\alpha N_{D_L} f_o exp\left(-\frac{E_a}{k_B T} + \frac{\xi q\alpha}{2k_B T}\right)\left(1 - \frac{N_{D_R}}{N_{D_{max}}}\right) \\ &- \frac{1}{2}\alpha N_{D_R} f_o exp\left(-\frac{E_a}{k_B T} - \frac{\xi q\alpha}{2k_B T}\right)\left(1 - \frac{N_{D_L}}{N_{D_{max}}}\right) \end{aligned} \tag{4.5}$$

The first terms in equation 4.5, $\frac{1}{2}\alpha N_{D_L} f_o exp\left(-\frac{E_a}{k_B T} + \frac{\xi q\alpha}{2k_B T}\right)\left(1 - \frac{N_{D_R}}{N_{D_{max}}}\right)$, represents the va-

cancy flux from the left side of the energy barrier to the right, and the second term represents flux from the right side to the left. Starting with the expression for left to right $-\frac{E_a}{k_B T}$ Inside the exponential represent the effect of activation energy barrier where k_B is the Boltzmann's constant and T is the temperature. The second term inside the exponential, $\frac{\xi q \alpha}{2 k_B T}$ represents the change in energy barrier due to electric field, ξ. In this term, the 2 in the denominator appears because, as figure 4.2b shows, only half of the change in energy barrier due to electric field is applied to each side of the barrier. In the pre-factor in front of the exponential term, f_o is the average attempt frequency with which each vacancy tries to surmount the barrier, and N_{D_L} is the vacancy concentration on the left side of the barrier. Also, from any given location, each vacancy can either hop to the left or the right side of its current location. Since we are only concerned about keeping track of vacancies going from left to right, on average only about half of the jumps will go in that direction. Therefore, in the prefactor, $\frac{1}{2}$ is used to take this effect into account. Finally, the term $\left(1 - \frac{N_{D_R}}{N_{D_{max}}}\right)$ is used to impose a limit on vacancy migration when a maximum attainable vacancy concentration, $N_{D_{max}}$ has been reached in the direction of the vacancy hop. This maximum attainable vacancy concentration is related to the maximum oxygen site concentration in the crystal that can accommodate vacancies (thermodynamic factors are not included; which would explicitly describe the accommodation of defects as a function of the defect chemical potential within the crystal [88]). When the vacancy concentration on the right side of the barrier, N_{D_R}, starts to approach $N_{D_{max}}$, this term reduces the flux proportionally. The term in equation 4.5 that corresponds to vacancy flux from right to left can be similarly broken down into its individual components and the meaning of each part is analogous to the ones discussed above.

The terms N_{D_L} and N_{D_R} can be expressed in terms of N_D using equations 4.6 and 4.7 respectively. Also, the activation energy term containing E_a in equation 4.5 can be factored out and

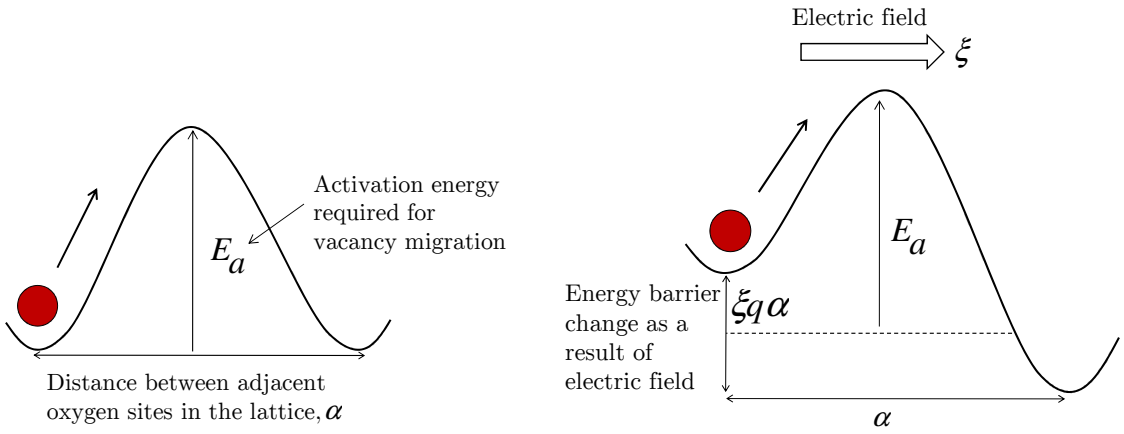

Figure 4.2: (a) In the absence of an electric field, oxygen vacancies encounter a symmetric energy barrier E_a hopping from one side to another. Under this condition, the flux in either direction is the same, leading to a net zero flux; (b) Presence of an electric field lowers the barrier on one side while increasing it on the other side, leading to a net flux in the direction of the electric field.

combined with the pre-factors to define the diffusion constant, D_o, as shown in equation 4.8.

$$N_{D_L} = N_D - \frac{\alpha}{2}\frac{dN_D}{dx} \tag{4.6}$$

$$N_{D_R} = N_D + \frac{\alpha}{2}\frac{dN_D}{dx} \tag{4.7}$$

$$D_o = \frac{1}{2}\alpha^2 f_o exp\left(-\frac{E_a}{k_B T}\right) \tag{4.8}$$

By substituting equation 4.6, 4.7 and 4.8 into equation 4.5 and removing second order terms, a simplified form can be obtained (Eq. 4.9).

$$\begin{aligned} J_{N_D} = &\frac{2}{\alpha} D_o N_D sinh\left(\frac{\xi q \alpha}{2k_B T}\right)\left(1 - \frac{N_D}{N_{D_{max}}}\right) \\ &- D_o \frac{dN_D}{dx} cosh\left(\frac{\xi q \alpha}{2k_B T}\right) \end{aligned} \tag{4.9}$$

When the electric field is small so that $\frac{\xi q \alpha}{2k_B T} \leq 0.1$ and $N_D \ll N_{D_{max}}$, equation 4.9 reduces to a simpler from where the first term represent the drift of vacancies due to electric field and second

term represents diffusion due to concentration gradient. The familiar Nernst-Einstein relationship where vacancy mobility $\mu = \frac{D_o q}{k_B T}$ also becomes evident in that case. However, for the more general case, The drift velocity of vacancies is defined from the first term of 4.9, and is given as:

$$v_{N_D} = \frac{2}{\alpha} D_o sinh\left(\frac{\xi q \alpha}{2 k_B T}\right)\left(1 - \frac{N_D}{N_{D_{max}}}\right) \tag{4.10}$$

Equations 4.1, 4.2, 4.3, and 4.4 (after substituting the expression for J_{N_D} from equation 4.9 into equation 4.4) fully describe the model that we used to explore the transient characteristics of the Schottky resistance switching device. The transient characteristic of vacancy transport, as represented by equations 4.4 and 4.9, is coupled to the Schottky interface through the N_D term in equation 4.1. Any change in vacancy concentration affects the potential profile ψ of the device, which in turn affects the device current-voltage characteristics. Current flow through the device consists of the drift and diffusion components in equation 4.2 and equation 4.3, which captures the thermionic emission of carriers over the Schottky barrier. Additionally, a parallel channel of tunneling current is calculated in the vicinity of the Schottky interface following the scheme outlined in [89]. The parameters of most interest for the study of dynamics of vacancy motion are ξ, T, and E_a, which control the timescale of switching and retention. Equation 4.10 is used to calculate the drift velocity of vacancies that corresponds to specific switching and retention conditions.

4.2 Model Implementation

Device Structure For Simulation

As mentioned earlier, the vacancy migration model discussed in the previous section was implemented on a 1-D Metal(M1)/Oxide/Metal(M2) structure, as shown in figure 4.3a. For the oxide layer, material parameters of $SrTiO_3$ were used. Motion of oxygen vacancies has been widely stud-

ied in $SrTiO_3$ and it is known to be able to accommodate large changes in vacancy concentration without going through any phase transformation. Since, with this model we are only looking at the dynamics of vacancy motion, ignoring secondary effects such as formation of secondary phases, the choice of oxide does not have a significant impact on the final result. Results obtained here can be easily generalize to other oxide based systems as long as the ionic motion blocking Schottky barrier condition holds true at the M1/Oxide interface. Consequently, M1 was modeled as a deep work function metal, such as Pt, that forms a Schottky contact with vacancy-doped $SrTiO_3$ due to the work function mismatch between the two layers; and it was treated as a blocking interface, such that donors/vacancies cannot cross the interface. M2 was modeled as a highly conductive oxide contact that forms an ohmic, non-oxygen-blocking contact with $SrTiO_3$ (such as conductive $SrTiO_3$ or $SrRuO_3$ [49]). Therefore, M2 acts as a source or a sink of oxygen vacancies to the $SrTiO_3$ layer, as necessary. The initial doping of the $SrTiO_3$ layer was assumed to be uniform with a concentration of 1×10^{18} cm^{-3}. Also, the vacancy concentration at the $SrTiO_3$/M2 interface was fixed at the value of 1×10^{18} cm^{-3} throughout the simulation. The temperature was maintained at 300 K for all simulations. The remaining material parameters and constants used in the simulation are listed in table 4.1. Using these parameters, the energy band structure prior to start of the simulation is shown in figure 4.3b.

One important parameter value that has not been discussed for is the activation energy, E_a for vacancy motion. Reported value of activation energy for vacancy motion in $SrTiO_3$ varies between 0.6-2.2 eV [42, 92]. Instead of selecting a single value of E_a, the simulation is performed with several different values of activation energies in order to fully explore its impact on switching dynamics.

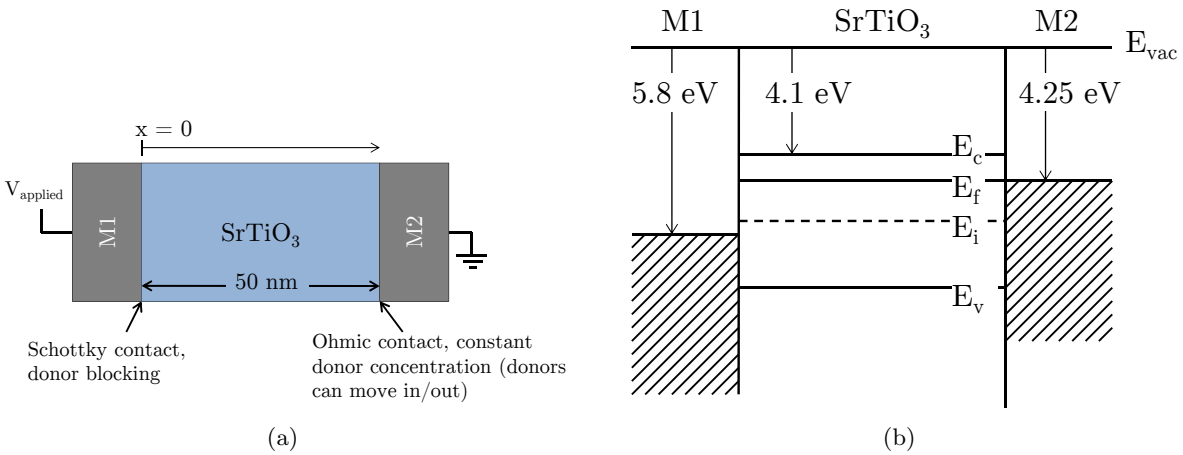

Figure 4.3: (a) Schematic of the M1/$SrTiO_3$/M2 structure used for simulation; (b) Energy band diagram showing position of the fermi levels in each layer prior to the start of the simulation. Due to the large work function difference between M1 and $SrTiO_3$, a Schottky barrier is formed at that interface. In order to create an ohmic contact, the fermi level of M2 was chosen such that it matches perfectly with the fermi level of the $SrTiO_3$ layer

Simulation Setup

The simulation solver loop is shown schematically in figure 4.4. The four coupled differential equations (Eq. 4.1-4.4) were solved iteratively. Since we are interested in the finding out the temporal evolution of the vacancy profile and its impact on device current-voltage characteristics, ideally all four equations should be solved using a time dependent solver. However, since the mobility of electrons and holes are many orders of magnitude faster than the mobility of oxygen vacancies, performing full transient simulation for all four equations is intractable. Time steps necessary to capture the transients of electron and hole motion need to be much smaller than the time steps needed for vacancy motion. In order to get around this problem, time stepping was carried out for equation 4.4, while the time dependent portions of equations 4.2 and 4.3 were set to zero. Adopting this method implies that the electrons and holes achieve steady state distributions instantaneously when compared to the time scale of vacancy motion. Again, this is a reasonable assumption given the mobility of vacancies vs. mobility of electrons and holes. As an example,

Table 4.1: Material parameters and constants for simulation

Parameter	Value
$SrTiO_3$ Thickness	50 nm
Bandgap, E_g	3.2 eV
Electron affinity, χ [90]	4.1 eV
Electron mobility, μ_n [91]	6 cm^2/V s
Hole mobility, μ_p [91]	5 cm^2/V s
Electron Effective mass, m_n	$5m_o$
Hole effective mass, m_p	$5m_o$
Gap between oxygen sites, α	2.76 Å
Max. allowed vacancy conc., $N_{d_{max}}$	2×10^{20} cm^{-3}
Attempt frequency, f_o	1×10^{13} s^{-1}
M1 work function, ϕ_{M1}	5.8 eV
M2 work function, ϕ_{M2}	4.25 eV
Relative permittivity, ε_r	300
Electron mass, m_o	9.11×10^{-31} kg
Boltzmann constant, k_B	1.38×10^{-23} J/K
Vacuum permittivity, ε_o	8.85×10^{-12} F/m
Electronic charge, q	1.6×10^{-19} C
Plank's constant, h	6.626×10^{-34} J s

if we assume E_a = 0.6 eV and T = 300 K, using equation 4.8, we get $D_o = 3.24\times10^{-13}$ cm^2/s. Using the Nernst-Einstein relations of $\mu = \frac{D_o q}{k_B T}$, where μ represents vacancy mobility, we get $\mu = 1.25\times10^{-11}$ cm^2/Vs. Comparing this value with the electron and hole mobility listed in table 4.1 clearly justifies the use of this 'quasi-transient' solver approach.

The three components that make up the total current through the device are the tunneling current, and the drift and diffusion currents of electrons (Eq. 4.2) and holes (Eq. 4.3). The potential profile obtained from the self-consistent solution to equation 4.1-4.4 are used to calculate the tunneling probability through the Schottky barrier and the total tunneling current following the scheme described by Sze [ref]. Then all three components of the current are summed together to get the total current at the given applied voltage. Throughout the simulation all voltage values are referenced with respect to the M1 contact, while the M2 contact is assumed to be grounded.

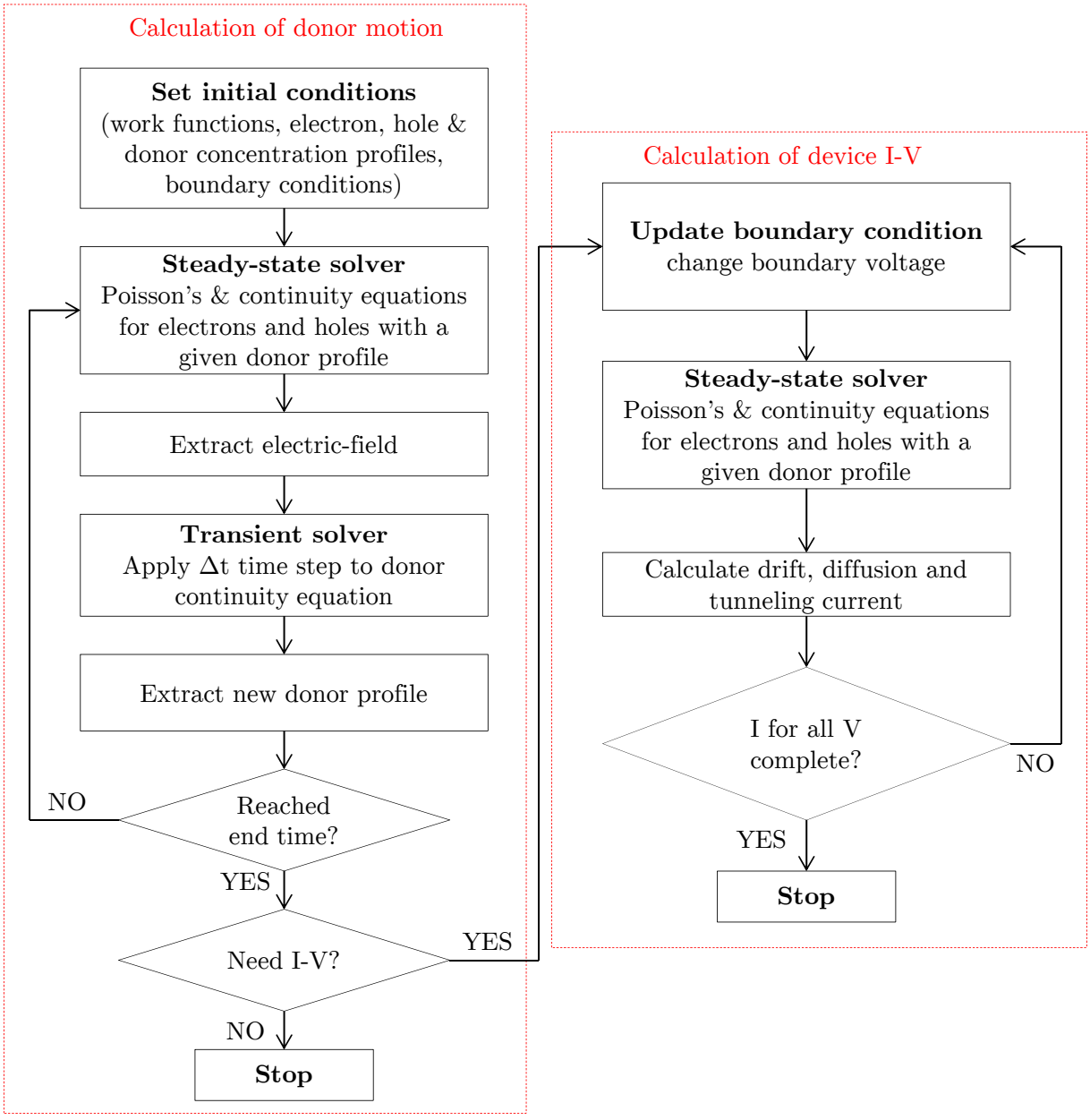

Figure 4.4: Schematic shows the solver loop used to couple steady-state solution of Poisson's equation (Eq. 4.1) and continuity equations for electrons (Eq. 4.2) and holes (Eq. 4.3) with the transient solution of donor continuity equation (Eq. 4.4). When the current voltage (I-V) characteristics of the device is desired for a given donor concentration profile, only the steady state portion of the solver is used while varying the boundary condition which reflects the externally applied bias.

4.3 Simulation Results

Programming

The presence of a large built-in electric field in the direction of the Schottky interface, owing to the small thickness of the $SrTiO_3$ layer and large work function difference between the two metal contacts, acts to modify the initial uniform vacancy concentration. In the simulation, the device was first equilibrated by determining the long-time solution to equations 4.1-4.4 with zero applied external bias. Figures 4.5a and 4.5b compares the initial vacancy and potential profiles with the corresponding equilibrium profiles. Due to the built-in electric field, vacancies accumulate next to the Schottky contact and get depleted from the $SrTiO_3$/M2 interface. However, since the $SrTiO_3$/M2 is treated as an open interface which can act as a source or sink, more vacancies get injected into the oxide layer as soon as the interface concentration begins to decreases. On the other hand, at the donor blocking Schottky interface, vacancies continue to accumulate until it reaches the maximum attainable concentration, $N_{D_{max}}$, which was set to 2×10^{20} cm^{-3}. As a result of the injected vacancies from the M2 contact, the equilibrium Schottky barrier depletion width is much thinner when compared to the barrier width of the initial uniform vacancy concentration profile.

In order to test the programmability of the device, once the equilibrium profile was achieved, a $\pm$ 5 V pulse was applied for 100 ns to program the device to either the ON or OFF state. For this simulation the activation energy, E_a, was chosen to be 0.175 eV and the temperature was 300 K. Application of a -5 V pulse causes the vacancy concentration at the Schottky interface to increase. As a result, the Schottky barrier depletion width decreases and thereby the tunneling current increases slightly. This is designated as the 'ON' state, since the device current in this state should be higher than the equilibrium state. However, since the vacancy concentration in the equilibrium state was already quite high at the M1/$SrTiO_3$ interface due to built-in electric field,

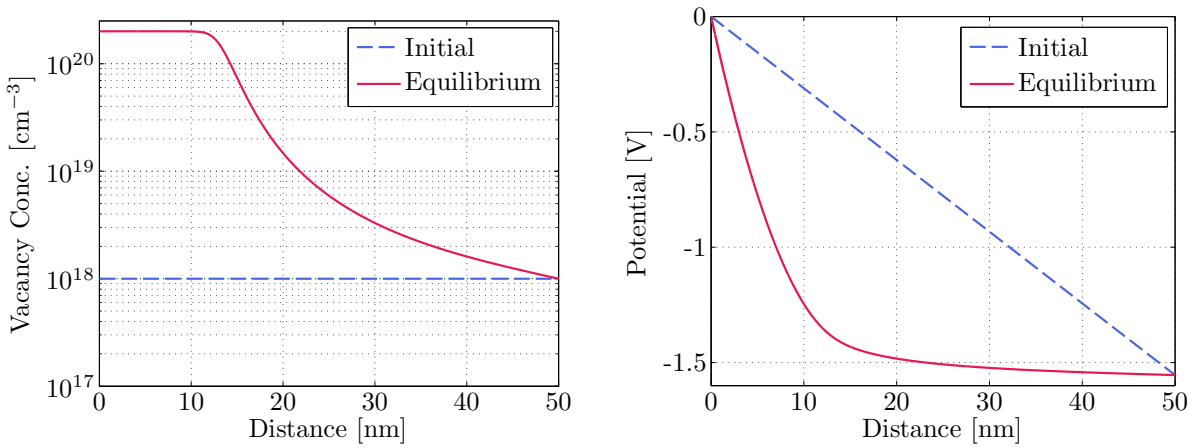

Figure 4.5: (a) Initial vacancy concentration prior to the start of the simulation is set to 1×10^{18} cm^{-3}. At equilibrium, there is significant accumulation of vacancies at the Schottky barrier due to built-in electric field. The maximum concentration at the interface is limited to 2×10^{20} cm^{-3}; (b) Corresponding potential profiles.

this -5 V programming pulse only very modestly increases the vacancy concentration. As a result, the potential profile is also only slightly affected by this redistribution. The application of +5 V, 100 ns pulse has the opposite effect on vacancy motion. Positive bias causes the vacancies near the M1/$SrTiO_3$ interface region to deplete from the equilibrium value and spread throughout the $SrTiO_3$ layer. This redistribution considerably affects the potential profile, which leads to a larger depletion region and consequently, smaller tunneling current. Figure 4.6 shows the 'ON' and 'OFF' state vacancy concentration and potential profiles immediately after the application of the 100ns programming pulses.

Retention

The vacancy profiles achieved immediately after the application of the programming pulses are not kinetically stable. Given enough time, drift due to built-in electric field and diffusion due to concentration gradients will cause the vacancy distributions to be restored to the equilibrium profile shown in figure 4.5a. This effect, in essence, defines the retention characteristics of the

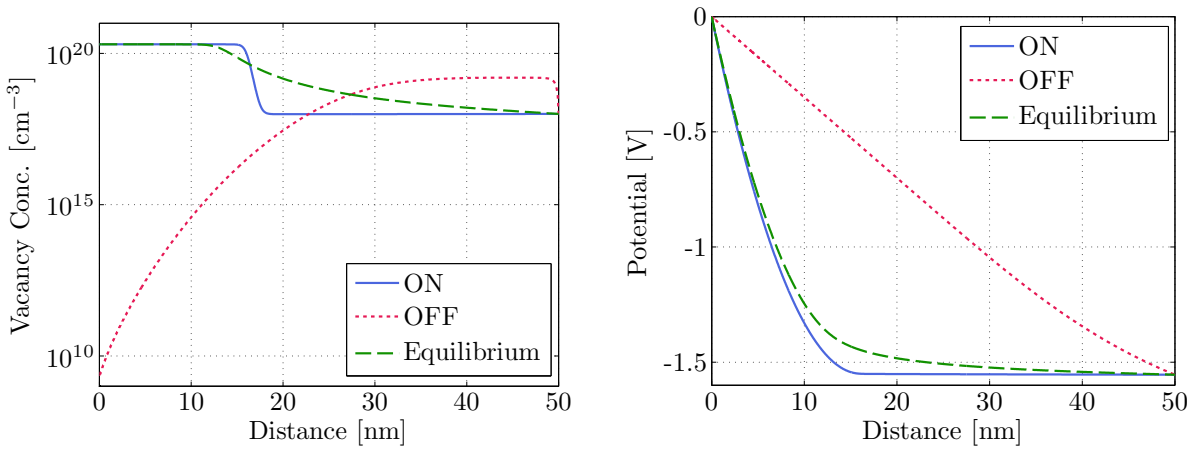

Figure 4.6: (a) Vacancy profile at equilibrium, and immediately after application of -5V (OFF state) and +5V (ON state). For all three cases $T = 300$ K and $E_a = 0.175$ eV; (b) Corresponding potential profiles. Thin depletion region in the ON state allows higher tunneling current compared to the thick depletion region in the OFF state.

device. Retention was investigated by simulating the vacancy profiles evolution as a function of time, in the absence of an applied voltage and using different values of the activation energy for vacancy migration. In each case, the ON and OFF state vacancy profiles (Fig. 4.6a) were used as the starting points.

Figure 4.7 shows the evolution of the vacancy profile from both the ON and OFF states, for an activation energy of 0.175 eV at $T = 300$ K after the programming pulse is removed. During this evolution, after each time step, the current through the device at -1 V is calculated for each new vacancy profile. This current for both the ON and OFF states as a function of time, for three different activation energies (0.175 eV, 0.6 eV and 1.02 eV), are shown in figure 4.8. As expected, as the vacancy profile evolves toward the equilibrium profile, the ON state current decreases and the OFF state current increases. Given long enough time, both states eventually merge to the same value of current, with higher activation energies taking longer. The initial changes in current with time are nearly linear on the log-log plot. However, the rate of change accelerates appreciably near the end (the OFF state has a complicated state of current owing to the profile evolution). Often

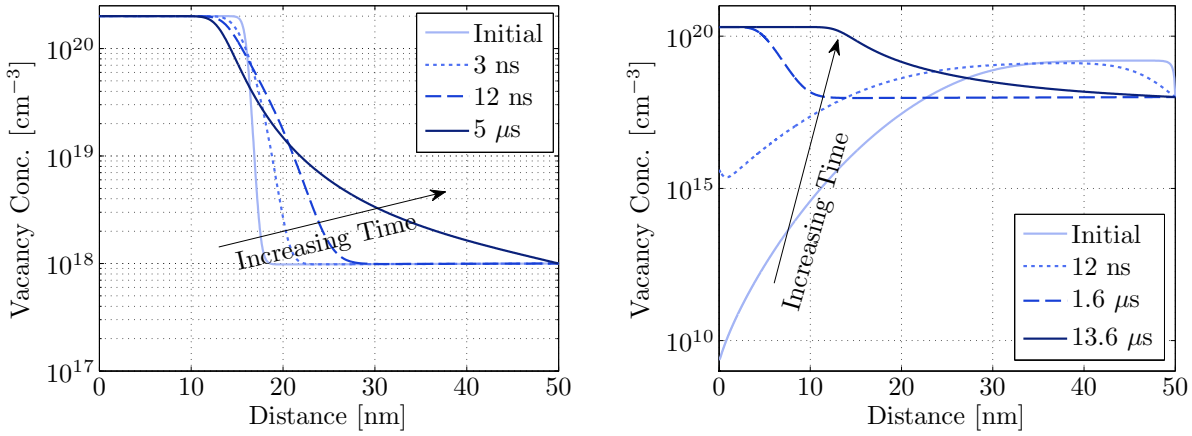

Figure 4.7: Evolution of ON (a) and OFF (b) state profiles towards equilibrium at $T = 300$ K with $E_a = 0.175$ eV. Once the programming pulse is removed, the internal electric field and concentration gradient slowly restores the originial equilibrium profile.

in literature, linear extrapolation of the early time data is used to estimate the retention time of devices. However, as figure 4.8 shows, this can greatly overestimate the retention time.

If we define the retention time of our device as the time at which point the difference in current between the OFF and ON state is lower than two orders of magnitude, then the upper dashed line (in Fig. 4.8 marked as 'ON Threshold') indicate the retention current for the ON state and the lower dashed line ('OFF Threshold') indicate the retention current for the OFF state. For an activation energy of 1.02 eV, this time is ≈10 years. For lower values of energies, the time is reduced drastically, ≈6.8 µs for 0.175 eV and ≈36 seconds for 0.6 eV. It is also interesting to look at the dynamic range in time between programming speed and retention time for a given set of E_a, T, and ξ. The programmed vacancy profiles which were used (shown in Fig. 4.6a) as the starting point for the retention simulations resulted from the application of a 100 ns long ±5 V pulse to a material with an activation energy of 0.175 eV; and for this case, the retention time was ≈ 6.8 µs. In other words, the retention time was only two orders of magnitude larger than the programming time. Similar results were observed for other activation energies as well, meaning

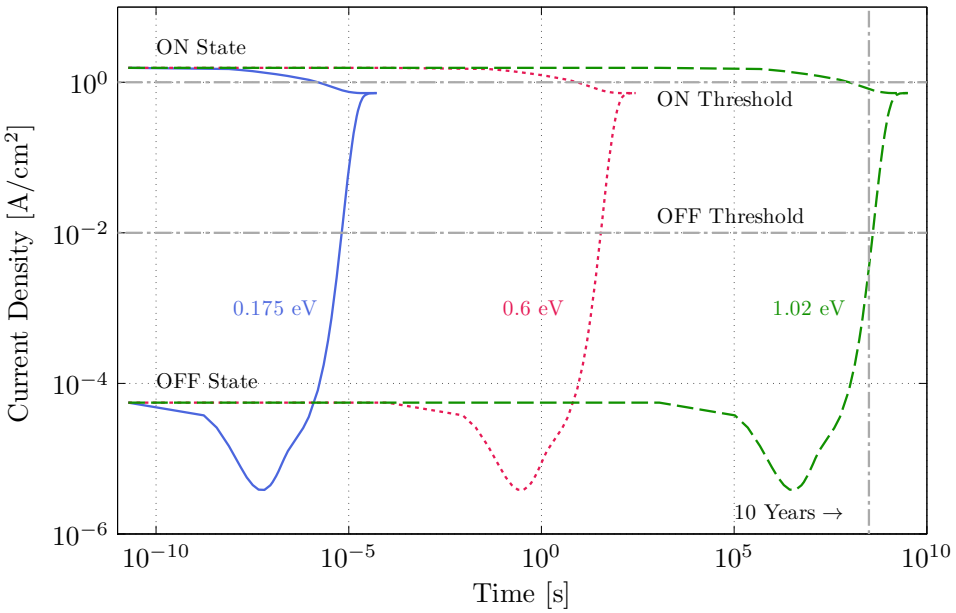

Figure 4.8: Current density measured at -1 V as a function of time for three different activation energies for vacancy migration. Current is measured periodically as the vacancy profile evolves from the programmed to equilibrium state (at T = 300 K). The two dotted lines marked as 'On Threshold' and 'OFF Threshold' indicate two orders of magnitude difference in current between the ON and OFF state. This is defied as retention. To achieve 10 years of retention, activation energy of 1.02 or larger is necessary.

the writing times needed to generate similar profiles to those shown in figure 4.6a are also only 1-2 orders of magnitude lower than the retention time, values unacceptable for data storage. Ideally, we would like to switch under the condition where the material behaved as if the activation energy for writing was $\approx$ 0.175 eV (T = 300 K) and for reading it was $\approx$ 1.02 eV. As mentioned earlier, three primary factors that control the timescale of programming are activation energy, temperature, and electric field. We would like to investigate if there exist any reasonable combination of these three parameters that will result in suitable switching and retention times.

4.4 Role Of Temperature, Activation Energy, And Electric Field

The effects of temperature, activation energy and electric field on device characteristics can be generalized from the simulation carried out for the 0.175 eV and 1.02 eV cases. Considering programming first, the ON and OFF state donor profiles shown in figure 4.6a were obtained under

the conditions of $E_a = 0.175$ eV, $V = \pm 5$ V, and $T = 300$ K. Under these conditions, programming the device from equilibrium state was possible in 100 ns. Using these parameters in equation 4.9, we can calculate a drift velocity of 0.67 nm/ns. For this calculation, the electric field, ξ, was assumed to be ± 5 V/50 nm, or 1 MV/cm. On the other hand, when we consider data retention, we see from figure 4.8 that in order to achieve 10 years of retention, we needed $E_a = 1.02$ eV at $T = 300$ K. The drift velocity for this case is calculated to be 3.3×10^{-15} nm/ns. For this calculation, the electric field is assumed to be 0.31 MV/cm. This is the built-in electric field that results from the 1.55 eV work function difference between the two electrodes, which works to restore the equilibrium vacancy profile starting from the OFF state. Here, we are considering the OFF to equilibrium transition because the change in vacancy profile and device current is more drastic for this transition than the ON to equilibrium transition. The electric field calculation was done by assuming that the potential drops linearly from one electrode to another (Fig. 4.6b). This assumption is valid during most the of the retention time period (until there is significant vacancy accumulation at the Schottky interface), and therefore for the purpose of estimating the timescale of vacancy motion, this can serve as a good approximate value.

Temperature

While all the simulations discussed so far was carried out at $T = 300$ K, retention characteristics under higher operating temperatures (e.g. 85 ^{o}C) are often desired. We can approximate the characteristics under higher temperatures from room temperature conditions. Under retention conditions, when the electric field is small (since there is no externally applied voltage), the electric-field dependence of vacancy mobility in equation 4.9 can be safely ignored. Consequently, the temperature dependence of vacancy flux mostly depend on E_a/k_BT term embedded in D_o in that equation. Therefore for a given set of E_a and T, as long as the ratio E_a/k_BT stays constant, the

retention characteristics would be similar. As an example, the retention characteristic with E_a = 1.02 eV and T = 300 K would be the same for E_a = 1.22 eV and T = 360 K (85 ^{o}C), since 1.02 eV/(k_B 300 K) = 1.22 eV/(k_B 360 K). Therefore, in order to have the same retentions properties at a higher operating temperature, a higher activation energy would be necessary.

Activation Energy

Figure 4.9 compares the drift velocity as a function for temperature for several different activation energies. For each activation energy, the drift velocity is plotted for two different electric fields; one corresponding to the programming field of 1 MV/cm and the second corresponding to the retention field of 0.31 MV/cm. The velocity corresponding to 100 ns write time (0.67 nm/ns) is marked as the Write-Line on the plot, and the velocity corresponding to 10 years of retention (3.3×10^{-15} nm/ns) is marked as the Read-Line. It is obvious that for none of these activation energies, velocities appropriate both for 10 years of retention and 100 ns writing time is achievable. For a 1.02 eV and 1.3 eV activation energies, 10 years of retention can be achieved, but vacancies cannot move fast enough to achieve a 100 ns programming time even with temperatures as high as 2100 K. For a 0.175 eV activation energy, vacancies can move fast enough at room temperature for 100 ns programming, but is always too high for 10 years of retention. In other words, there does not seem to be any reasonable combination of activation energy and temperature that control the timescale of device evolution, that lead to a reasonable operational window for Schottky type devices based on uniform ionic motion.

Electric Field

Electric field is the third major parameter which can have a large impact on device behavior. Figure 4.9 examines a wide range of temperatures and activation energies, but it only considers

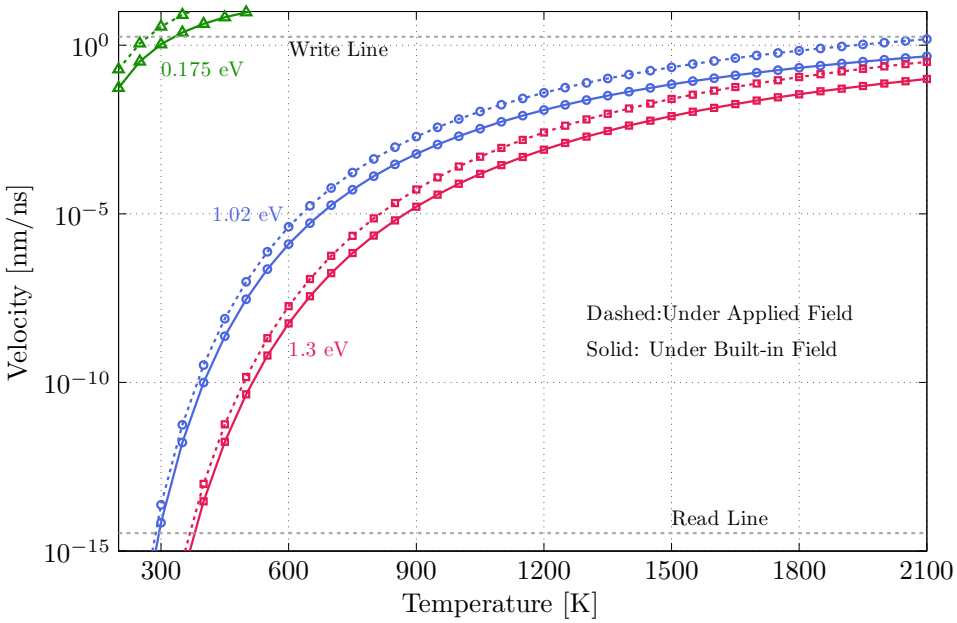

Figure 4.9: Vacancy velocity as a function of temperature for three different activation energies under built-in field (0.31 MV/cm) and under applied field (1 MV/cm). 'Read Line' indicates the maximum allowable velocity for 10 year retention and 'Write Line' indicates the minimum required velocity for 100 ns programming.

two electric fields (1 MV/cm and 0.31 MV/cm). While for the low activation energy case (0.175 eV), the vacancy velocity cannot be slowed down (thus, long retention is never possible), for the high activation energy case (1.02 eV) the velocity can be increased by increasing the applied electric field during programming. Therefore it is worthwhile to look at how much the electric field needs to be increased in order to achieve a reasonably fast programming time. According to equation 4.10, vacancy velocity is exponentially related to the electric field. Figure 4.10 shows several vacancy velocities for the 1.02 eV activation energy as a function of both electric field and temperature. The line corresponding to the velocity needed to achieve 100 ns programming time (0.67 nm/ns) is highlighted in red (dashed). From this line we see that, in order to achieve 100 ns programming with 1 MV/cm electric field, the temperature needs to be approximately 2400 K. On the other hand, to achieve the same programming time at a lower temperature, e.g. 1000 K, the field needs to be $\approx$ 30.5 MV/cm (that is 153 volts over the 50 nm oxide layer!). Considering the electrical

breakdown characteristics of oxides [93], applying a field much larger than 3-4 MV/cm does not seem reasonable. Therefore, like the activation energy and temperature, tuning the device behavior by increasing the electric field also does not seem to get us all the way to the desired operation limits. Regardless of whether the region of ionic motion is uniform throughout the device or confined to a small portion of the device, the same trade-offs among electric field, temperature and activation energy exist will exist.

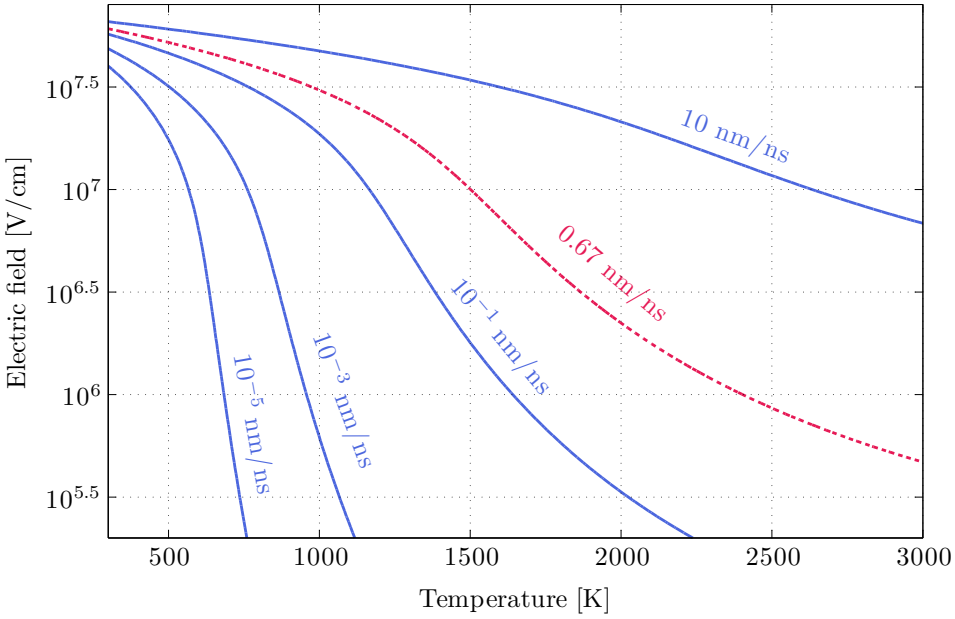

Figure 4.10: Vacancy velocity for $E_a = 1.02$ eV as a function of electric field and temperature. 0.67 nm/ns is needed to achieve 100 ns programming with $\pm$ 5 V pulse.

Few other factors, such as double ionization of vacancies, electromigration and local electric fields, that may also play some role in determining the device behavior is briefly discussed below.

4.5 Other Factors Affecting Vacancy Motion Dynamics

Vacancy Ionization Level

Throughout our discussion so far, we have operated under the assumption that oxygen vacancies are singly ionized. However, it has been suggested that vacancies in some cases may be doubly

ionized [94]. To evaluate the impact of double ionization, simulations were carried out with vacancy ionization level set to +2. In order to incorporate this into the model, equations 4.1 and 4.5 were modified as shown in equation 4.11 and 4.12 respectively.

$$\nabla \cdot (\varepsilon_r \varepsilon_o \nabla \psi) = q\,(p - n + 2N_D) \tag{4.11}$$

$$\begin{aligned} J_{N_D} = &\frac{1}{2}\alpha N_{D_L} f_o exp\left(-\frac{E_a}{k_B T} + \frac{\xi q \alpha}{k_B T}\right)\left(1 - \frac{N_{D_R}}{N_{D_{max}}}\right) \\ &- \frac{1}{2}\alpha N_{D_R} f_o exp\left(-\frac{E_a}{k_B T} - \frac{\xi q \alpha}{k_B T}\right)\left(1 - \frac{N_{D_L}}{N_{D_{max}}}\right) \end{aligned} \tag{4.12}$$

Simulation results indicate that when the same switching pulse (100 ns and ±5 V) is applied, the retention time for doubly ionized case is 6.35 μs compared to 1.58 μs for the singly ionized vacancies with $E_a = 0.175$ eV (shown in figure 4.11). Similar differences in retention time is observed for other values of activation energies as well. This difference is due to higher ON state and lower OFF state initial currents that results from higher vacancy migration (thus, a stronger 'write' operation) due to stronger influence of electric field on doubly ionized vacancies. As figure 4.12 shows, there is a shift in both the vacancy and potential profiles between the singly and doubly ionized cases in equilibrium, ON and OFF states. Since double ionization lead to higher charge density, the depletion width is shorter in the equilibrium and ON states compared to the singly ionized case. However, in the OFF state, more vacancies migrate away from the interface in the doubly ionized case because the force on each ion is greater from the applied electric field due to the higher charged state. These effects combine to give a lower OFF current and higher ON current when compared to the singly ionized case. Although the ON and OFF current levels are different, the retention time does not change by orders of magnitude. This is because the effect of electric field on vacancy drift during retention period is also twice as high when the vacancies are charged +2 instead of +1. Therefore, the fundamental dilemma remains the same regardless of the vacancy ionization level.

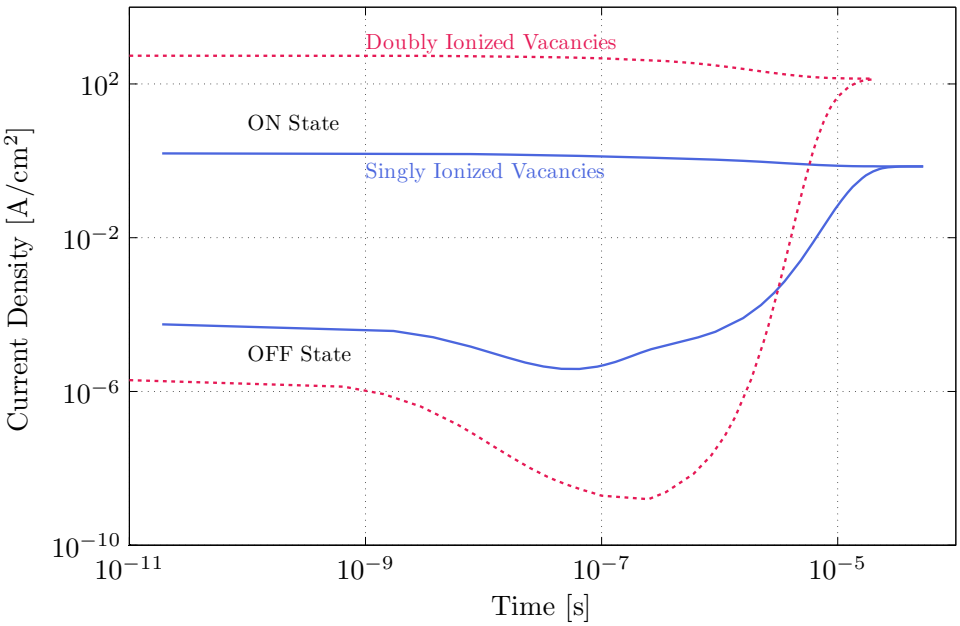

Figure 4.11: Comparison of retention characteristic of the device with singly and doubly ionized vacancies. Activation energy and temperature for both cases is 0.175 eV and 300 K respectively.

Electromigration

Electromigration is another mechanism which has been linked to a possible way of obtaining a wider operational window for these devices. Physically this mechanism is explained as increased ion motion owing to a high number of electron impacts with the ions due to high device current [95]. This can be equated to an effective reduction in the activation energy. Typical reductions in activation energies have been reported to be ≈20% [96]. As an example, if E_a = 1.02 eV, under high electric field when there is high current (e.g. under programming conditions), incorporation of the electromigration effect would make the device behave as if it had an activation energy of .816 eV. Yet again, like the doubly ionized vacancies case, the change in activation energy is in a favorable direction; however, the effect is not large enough to alter the programming or retention behavior in any significant way.

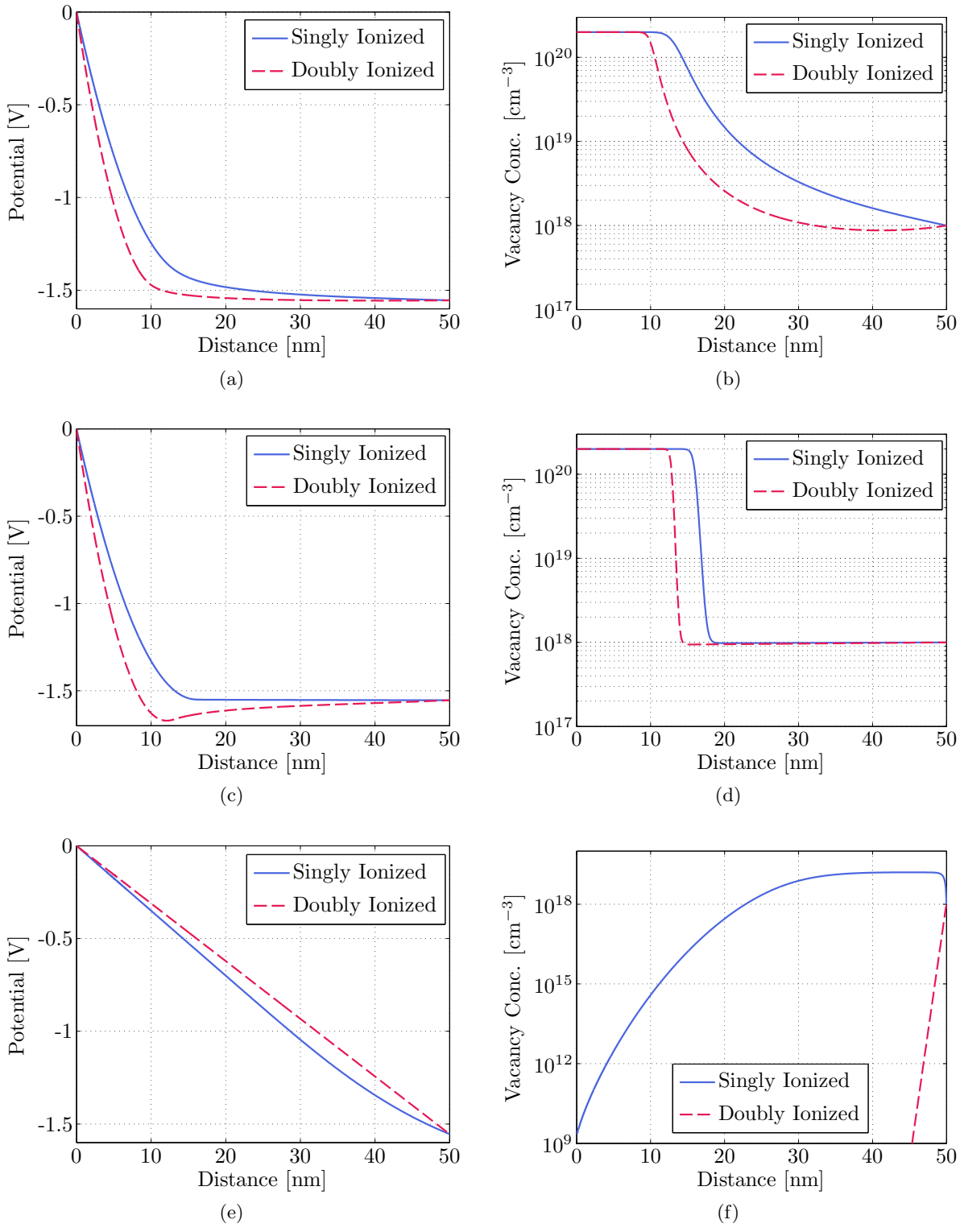

Figure 4.12: Equilibrium potential (a) and vacancy (b) profiles; ON state potential (c) and vacancy (d) profiles; OFF state potential (e) and vacancy (f) profiles for singly and doubly ionized vacancies.

Local Electric Field

Another mechanism that has been proposed is that the local electric field (acting on an atomic site) inside the dielectric is much greater than the macroscopically observed (applied) field [52]. According to the Lorentz relationship, the local field, ξ_{local}, at an atom in a dielectric is given by equation 4.13.

$$\xi_{local} = \xi\left(1 + F\varepsilon_r\right) \tag{4.13}$$

where, ε_r is the dielectric susceptibility, and F is the Lorentz factor. Therefore, in materials with high dielectric susceptibilities exposed to large electric fields, such as $SrTiO_3$ with $\varepsilon_r = 300$, it is possible to achieve local fields that are significantly (orders of magnitude) higher than the external field, depending on the Lorentz factor. When the local field is large enough, the velocity of vacancies is substantially increased since they are exponentially related. As a result, the difference in vacancy velocity under the built-in field and applied field significantly increases, as shown in figure 4.13 using $F = 0.2$ for activation energy of 1.3 eV (though field dependent dielectric constant [93] was not included in this calculation, which would complicate the picture somewhat). It is apparent that the separation between the solid (low field) and dashed (high field) lines is much larger and the velocity is higher than that determined in figure 4.9. The low field and low temperature retention time is greater than the value needed or 10 years (point 'b' in figure 4.13), while the local field increase combined with a reasonable temperature rise (700K) leads to a 100 ns programming time (point 'a'). **However, this whole argument in favor of local field is presented as purely a mathematical exercise.** the appropriateness of inclusion of local field with regard to calculation of vacancy mobility remains to be verified. Several reports have described the effects of the local field (or field gradient) on ion displacements [97, 98] in dielectrics. It has also been argued that when ion hopping takes place between crystallographically similar sites, the local field plays no role

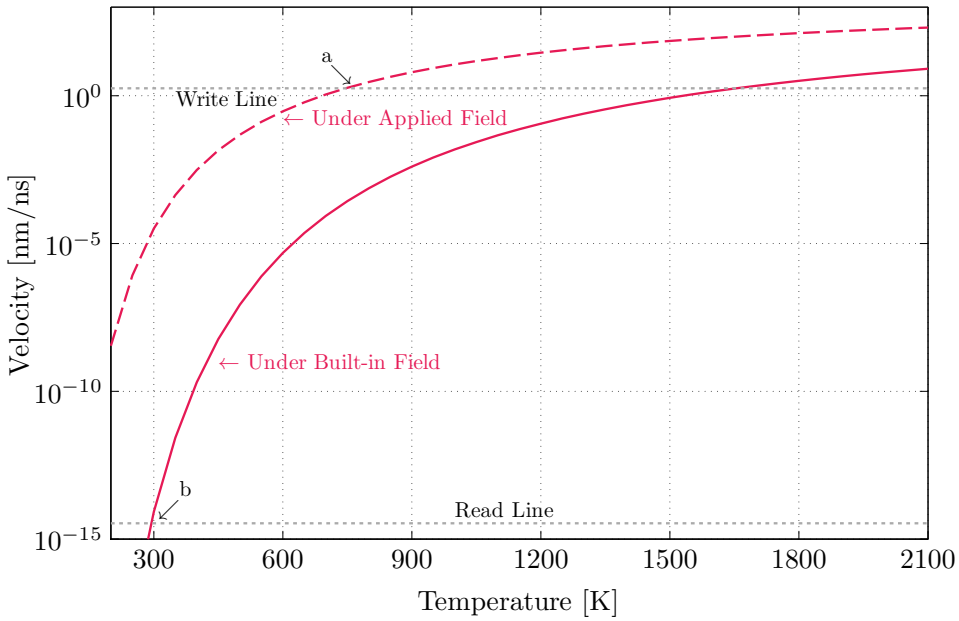

Figure 4.13: Vacancy velocity as a function of temperature under built-in and applied electric field taking into account the Lorentz factor with T = 300 K, E_a = 1.3 eV and F = 0.2. 'Read Line' indicates the maximum allowable velocity for 10 year retention and 'Write Line' indicates the minimum required velocity for 100 ns.

in determining the hopping rate [99, 100]. From an energy conservation perspective, this argument certainly has merit. On average, the only electric field experienced by a migrating ion is the macroscopic field. Any local enhancement of that field in one part of the crystal must be balanced by reduction in other parts. While a physical parameter capable of causing static ion displacements was deemed worthy of consideration in the model, it is clear that experimental verification of such an effect is needed before it is given any serious consideration.

4.6 Conclusion

The model and simulation results presented here, incorporating only standard physical parameters, demonstrate quantitatively the fundamental conflict between retention and programming dynamics that is present in any resistance switching device based on homogeneous ion motion. Although the results presented here were specific to a $SrTiO_3$ based Schottky type device, the model is general and can be applied to other device geometries and material systems. It is clear that

no reasonable combination of electric field, temperature, and activation energy can lead to an appropriate operating window for these devices. Secondary effects, such as electromigration, are not expected to significantly improve this condition either. The exponential dependence of vacancy velocity on electric fields, which is often invoked in literature to explain resistive switching, does not seem to provide the necessary dynamic range. Based the on the mechanisms described here, one can come up with contrived situations and device geometries [101] which may seem promising, however, the general case of a simple metal/oxide/metal type system cannot be explained fully. Other mechanism, those not included in this model, such as formation of secondary phases of oxides due to oxygen ion migration must be examined carefully in order to fully understand how this fundamental conflict can be resolved. In systems dominated by filamentary conduction, these other mechanisms will have a large role in determining the dynamics. How the electric field and temperature affects the device behavior in those systems may also be different than the assumptions used in this model.

Chapter 5

Time-Dependent Electroforming Study

In chapter 3, some of the factors related to device design and test protocols that can impact the electroforming and the switching characteristics of TiO_2 based devices were discussed. It was observed that the control of compliance current during electroforming with DC voltage sweeps is a critical factor for obtaining stable resistive switching. Although, it is clear that events that take place during electroforming are intimately connected to the subsequent resistive switching phenomenon, there is a surprising lack of any extensive study on electroforming. This is partially due to the fact that electroforming is an one-time non-reversible event, which makes it particularly difficult to study. It is generally believed that the conductive filaments that are responsible for resistive switching are formed during the electroforming step. However, exactly what conditions trigger the formation of these filaments and how such events can be controlled remains largely unknown.

Figure 5.1 shows an example of resistance switching and electroforming with DC voltage sweep similar to many cases discussed in chapter 3. In that chapter, the transient current overshoot associated with enforcing a compliance current during DC electroforming was discussed in detail. However that experiment only showed the time dependent behavior of the compliance process where the transients were dictated by the current control mechanism of the voltage source. It did not show

the actual change of resistance as a function of time of the device itself. The voltage and current transients that take place during this transition period (between P1 and P2) was not captured and therefore no information was gained about the events that took place during this time.

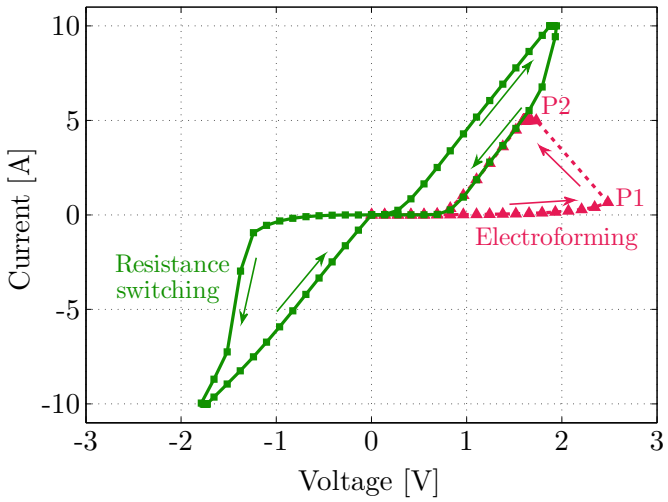

Figure 5.1: Electroforming and resistance switching of a 5 µm × 5 µm device with DC voltage sweep. Point P1 and P2 marks the voltage and current just prior to and immediately after electroforming, respectively. The transient change in voltage and current from P1 to P2 cannot be measured using this DC method.

In order to overcome the limitations posed by the DC electroforming method, in this chapter a method will be discussed where electroforming is induced using voltage pulses of controlled amplitude and time span. This allows for examination of the transient voltage, current, and power dissipation of the device during the electroforming process. This chapter is organized into three sections. In the first section, the experimental setup necessary for the pulsed electroforming study is described. The second section is focused on the dynamics of the electroforming process. Here the correlation among the electroforming voltage, time, and the ambient temperature from various types of pulsing experiments will be discussed along with how these electroforming conditions affect the subsequent resistance switching properties of the device. In the third section a thermal model of the device will be presented and some of the experimental observations will be correlated with predications from this model.

5.1 Experimental Setup

All the pulsed experiments described in this and the next two chapters were carried out using 5 μm × 5 μm sized devices. These devices were fabricated using TiO_2 films deposited using ALD method at 200 °C. The device geometry (shown in chapter 3, figure 3.3b) was designed such that both DC and high speed pulsing experiments could be performed on the same structure. For simple DC experiments (performed using Keithley 2400 source-meter), pads A and B were used to access the top and bottom electrodes of the device, respectively. For high speed pulsing experiments all three pads (A, B, and C) were utilized. The experimented setup is shown in figure 5.2a. Two GS-type microwave probes are used for this setup. One probe connects a voltage pulse source (Agilent 81110A) between pad pair A-C and the second probe connects an oscilloscope (Agilent DSO6104A) between pad pair A-B. The resulting circuit is shown in figure 5.2b. This connection method essentially creates a series circuit containing the input impedance of the pulse source (z_o = 50 Ω), the oxide device, and the termination resistance of the oscilloscope (set to z_o to match the characteristics impedance of cables and the microwave probes).

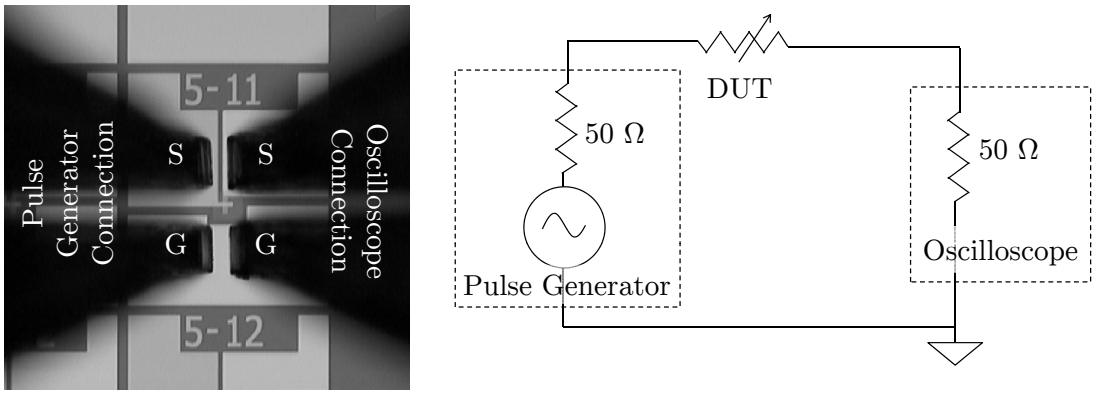

(a) (b)

Figure 5.2: (a) Two GS-type microwave probes are used to connect the pulse generator and the oscilloscope to the device; (b) Circuit corresponding to the connection.

Because of the series configuration of the circuit in figure 5.2b, the oxide device and the 50 Ω

resistance of the oscilloscope forms a voltage divider network. If the voltage generated by the pulse source (V_p) is known, then by measuring the voltage drop over the oscilloscope (V_s) the voltage (V_d), current (I_d) and resistance (R_d) of the oxide device can be calculated. Equations 5.1 and 5.2 show the expressions for V_d and V_s, respectively.

$$V_d = V_p \left(1 + \frac{(R_d + z_o) - z_o}{(R_d + z_o) + z_o}\right) \left(\frac{R_d}{R_d + z_o}\right) \tag{5.1}$$

$$V_s = V_p \left(1 + \frac{(R_d + z_o) - z_o}{(R_d + z_o) + z_o}\right) \left(\frac{z_o}{R_d + z_o}\right) \tag{5.2}$$

In equation 5.1, the term $\left(1 + \frac{(R_d+z_o)-z_o}{(R_d+z_o)+z_o}\right)$ is the voltage across the series combination of the oxide device and the oscilloscope termination resistance, taking into account the incident pulse and the reflected pulse due to impedance mismatch. The term $\left(\frac{R_d}{R_d+z_o}\right)$ represents the portion of the voltage that is dropped across the oxide device. Equation 5.2 is identical to 5.1, except that it calculates the voltage drop across the oscilloscope. The two terms, R_d and V_d are the only unknown quantities in these equations. The values for the other three variables in these equations, namely V_p, V_s, and z_o, are all known. V_p is controlled through the pulse source, V_s is capture by the oscilloscope and $z_o = 50\ \Omega$. The solutions for R_d and V_d in terms of V_p, V_s, and z_o are given in equations 5.3 and 5.4, respectively. I_d, calculated based on V_d and R_d using Ohm's law, is given in equation 5.5.

$$R_d = \frac{2z_o\,(V_p - V_s)}{V_s} \tag{5.3}$$

$$V_d = 2\,(V_p - V_s) \tag{5.4}$$

$$I_d = \frac{V_d}{R_d} = \frac{V_s}{z_o} \tag{5.5}$$

For all the pulsed electroforming experiments, voltage pulses generated by the pulse source

had a rise and fall time of $\approx$ 2.5 ns. The experimental setup described above does not allow for independent measurement of this pulse; only the voltage drop over the oscilloscope is measured. As a result, the value V_p in equations 5.3 and 5.4 is only known when the pulse amplitude from the pulse source reaches its specified value. therefore, R_d and V_d can only be calculated when V_p value is steady and not during the rise and fall time of the pulse.

5.2 Pulse Induced Electroforming

In order to learn about various aspects of electroforming, using the setup described in the previous section, three types of pulsed electroforming experiments were performed. For clarity of explanation, they will be referred to as 'fixed pulse width', 'fixed pulse amplitude', and 'pulse-train' experiments.

Experiment 1: 'Fixed Pulse Width'

For this experiment, the oxide devices were subjected to consecutive pulses with fixed width but increasing amplitude until electroforming was observed. The pulse amplitude was increased from 0 volts in increments of 0.1 volts. The time gap between consecutive pulses was $\approx$ 1 s. An example case for this experiment is shown in figure 5.3. Figure 5.3a shows the voltage across a device as a function of time for a set of five 250 ns long pulses leading up to the electroforming event (labeled P1 through P5). The corresponding device current, resistance, and power dissipation as a function of time are shown in figures 5.3b, 5.3c, and 5.3d, respectively. For clarity, not all the pulses starting from 0 V are shown. Only P3-P5 are consecutive pulses, and some of the intermediate pulses before and after P1 and P2 are omitted. $t = 0$ corresponds to the time when the pulse reaches its full amplitude after the initial rise time of 2.5 ns. The voltage amplitude set-points, V_p, on the pulse source were 1.5 V, 2.1 V, 2.6 V, 2.7 V, and 2.8 V for pulses P1 through P5, respectively. Once a pulse with sufficient amplitude was applied, the device resistance suddenly changed to a

low value (pulse marked as P5). This pulse is labeled as the 'Electroforming pulse'. Since the device was in series with two 50 Ω resistors (the input impedance of the pulse generator and the termination impedance of the oscilloscope), as the resistance of the device decreased with time, the voltage across the device also showed a corresponding decrease. The time corresponding to the inflection point of the electroforming voltage curve is denoted as $t_{forming}$, which marks the time it takes to initiate permanent lowering of the device resistance. The voltage at $t_{forming}$ is denoted as $V_{forming}$. The small glitches observed in all the plots at t ≈ 22 ns, 44 ns, 66 ns, and so on, prior to electroforming, were due to impedance mismatch and resulting reflection of the high frequency components associated with the rising edge of the pulses. This was a result of the device geometry and the experimental setup and was present for all pulses. The amplitude of these glitches decreased gradually for each successive reflection and eventually became negligible.

As figure 5.3c shows, the decrease in resistance was not limited to the electroforming pulse only. Similar resistance decrease is apparent for pulses that immediately preceded the electroforming pulse (P3 and P4). However, unlike the electroforming case, this decrease in resistance were verified to be non-permanent in nature. Figure 5.4 shows a case where a similar experiment to the one described for figure 5.3 was carried out. However, instead of single pulses, two pulses at each voltage amplitude was generated. Like before, only five different voltage amplitudes are shown in the plot. For each amplitude, the first pulse is marked as Pxa and the second as Pxb. The amplitude set-points on the pulse-source were 1.05 V, 1.8 V, 2.05 V, 2.1 V, and 2.15 V for pulses P1x through P5x, respectively. Each pulse has a width of 1 μs and the time gap between every pulse was maintained at ≈ 1 s. Figure 5.4 shows that the voltage across the device overlapped exactly for each given amplitude until electroforming. For the electroforming case, even though the amplitude set-point for both P5a and P5b were the same, due to the permanent lowering of resistance during P5a, the voltage profile P5b differs significantly from the prior pulse. For all other

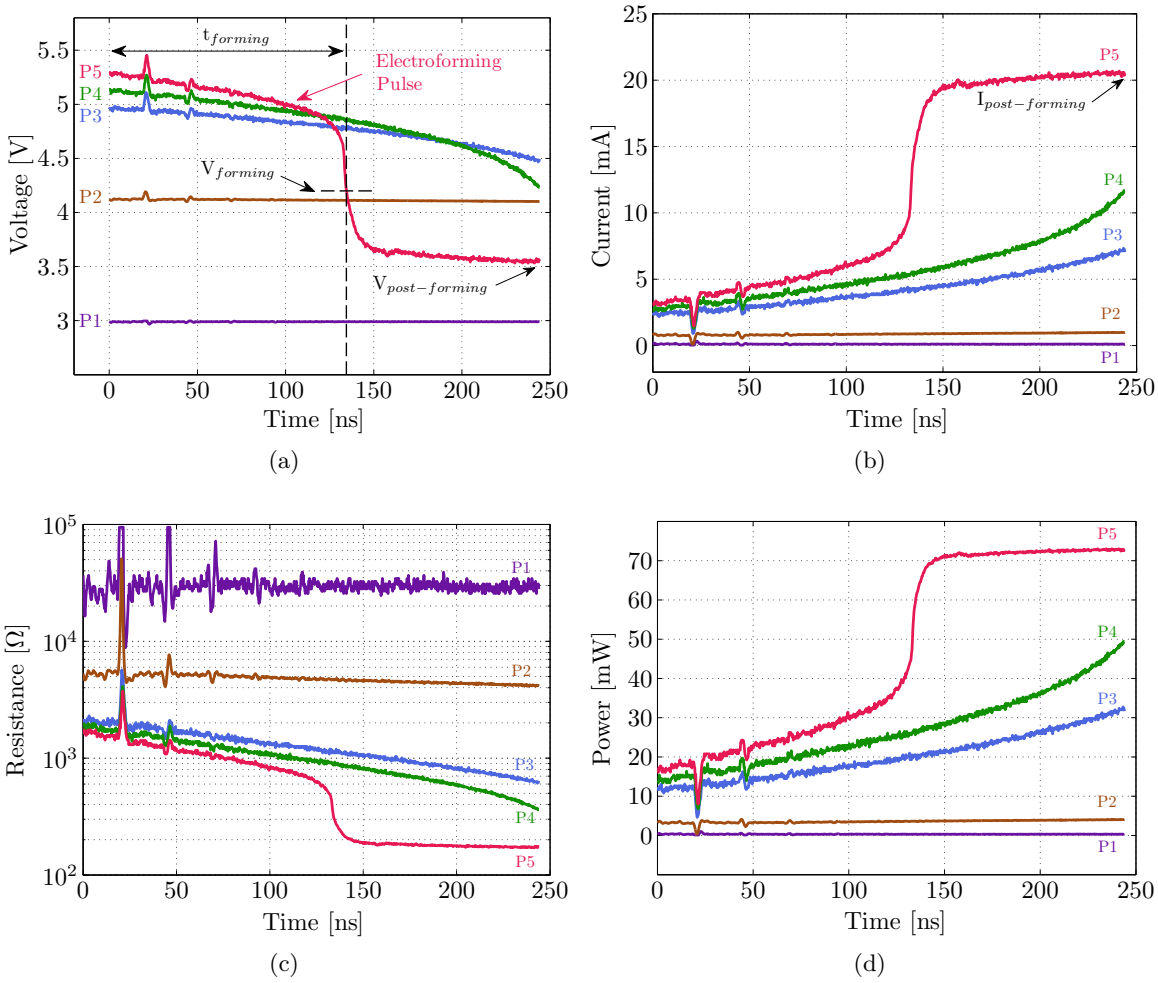

Figure 5.3: Transient voltage (a), current (b), resistance (c) and power (d) profiles for five 250 ns pulses. Pulse marked P5 corresponds to the electroforming pulse in all four plots. V_p was 1.5 V, 2.1 V, 2.6 V, 2.7 V, and 2.8 V for pulses P1-P5, respectively.

cases, transient changes in resistance observed prior to electroforming did not permanently alter the device behavior.

In figure 5.3a, both $t_{forming}$ and $V_{forming}$were defined based on the inflection point of the electroforming pulse. It is however not clear that such an inflection point would not exist in pulses prior to electroforming. One can imagine pulse P4 in figure 5.3a having an inflection point if it was slightly longer in time. Whether or not that would have triggered a permanent change in device resistance is not known. But since the inflection point was always a common feature in

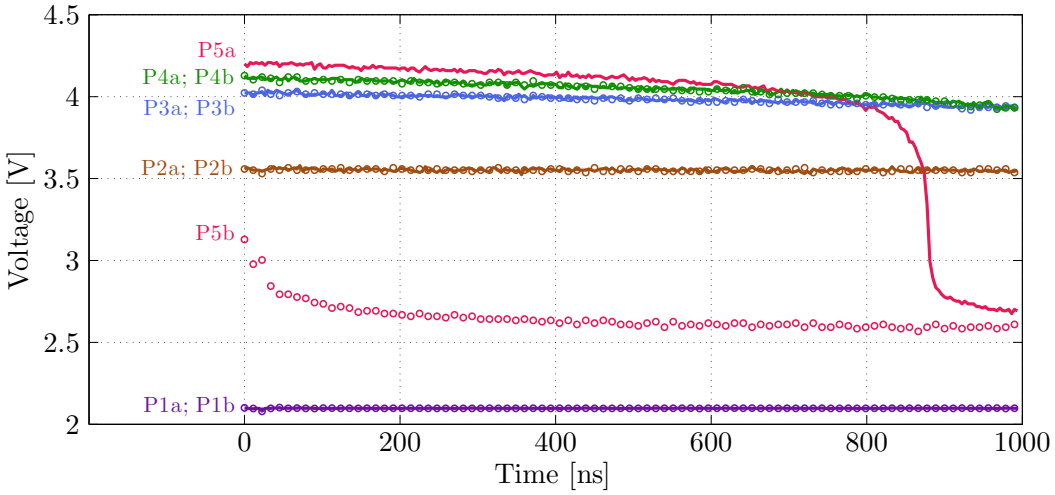

Figure 5.4: Electroforming with double pulses. At each voltage amplitude, two voltage pulses were generated. The first pulse is marked as Pxa (solid line) and second is marked as Pxb (open circles). For P1x through P4x, both pulses exactly overlap each other. This is in contrast to the case for P5a and P5b. Due to electroforming during P5a, it differs significantly from P5b.

the electroforming pulse across all devices, it was the most consistent way of defining $t_{forming}$ and $V_{forming}$.

Similar results to the ones presented in figure 5.3 were observed for all other pulse widths on other devices. The device behavior under pulses prior to the electroforming pulse was always repeatable, but once the electroforming pulse was encountered, the resistance level changed permanently. As the resistance level stabilized after electroforming, the power dissipation level also reached a stable value, as can be seen in the 150-250 ns time range in figure 5.3d for the electroforming pulse. A more detailed discussion about this post-electroformed power dissipation level and its impact on resistive switching will be discussed in the next sub-section

Experiment 2: 'Fixed Pulse Amplitude'

The procedure of the 'fixed pulse width' experiment described in the previous section was such that each device experienced multiple pulses prior to encountering the electroforming pulse. Therefore, it is possible that $t_{forming}$ and $V_{forming}$ may have been influenced as a result of subjecting the device

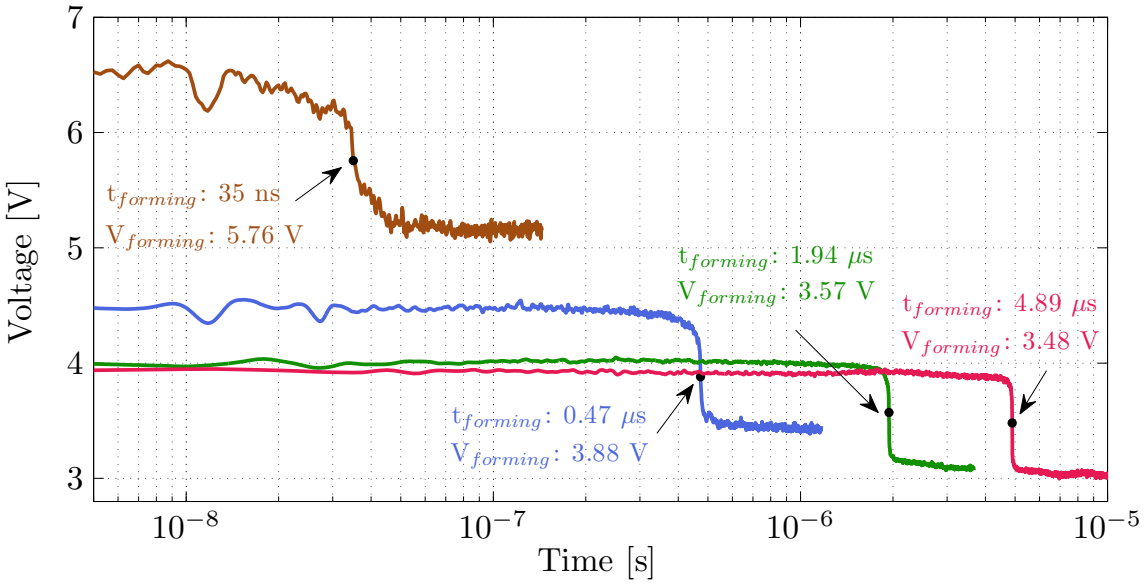

Figure 5.5: Electroforming voltage profiles with varying pulse amplitudes. The ambient temperature was 25 °C for all cases shown here.

to a series of pulses. In order to remove this ambiguity, a new experimental procedure, referred to as 'fixed pulse amplitude', was developed. Here, each pristine untested device was subjected to a single voltage pulse of fixed amplitude with a width that would, based on the prior results, lead to electroforming. This test protocol ensured that the device behavior could not have been affected by anything other than the electroforming pulse. This experiment was repeated for several different voltage amplitudes at three different ambient temperatures (25 °C, 62.5 °C, and 100 °C). The ambient temperature was set by controlling the stage temperature of the probe station used for the pulsed measurements. The goal of this experiment was to check the influence of temperature on the electroforming characteristics. For each voltage amplitude and ambient temperature combination, $t_{forming}$ and $V_{forming}$ were measured for three separate devices to check the uniformity across different devices.

Figure 5.5 shows four examples of electroforming under different pulse amplitudes at 25 °C ambient temperature. While qualitatively the electroforming characteristics look about the same, the change in $t_{forming}$ is many orders of magnitude higher compared to the corresponding change in

$V_{forming}$. A change of less than a factor of 2 in $V_{forming}$, from 3.48 V to 5.76 V, decreased $t_{forming}$ by more than two orders of magnitude. The relationship between $t_{forming}$ and $V_{forming}$ under all three ambient temperature conditions across all measured devices is shown in figure 5.6a. Each marker on this plot represents an individual device. In total, $\approx$ 140 devices were electroformed under various voltage and temperature combinations. The dotted lines are added to the figure as a guide to the eye.

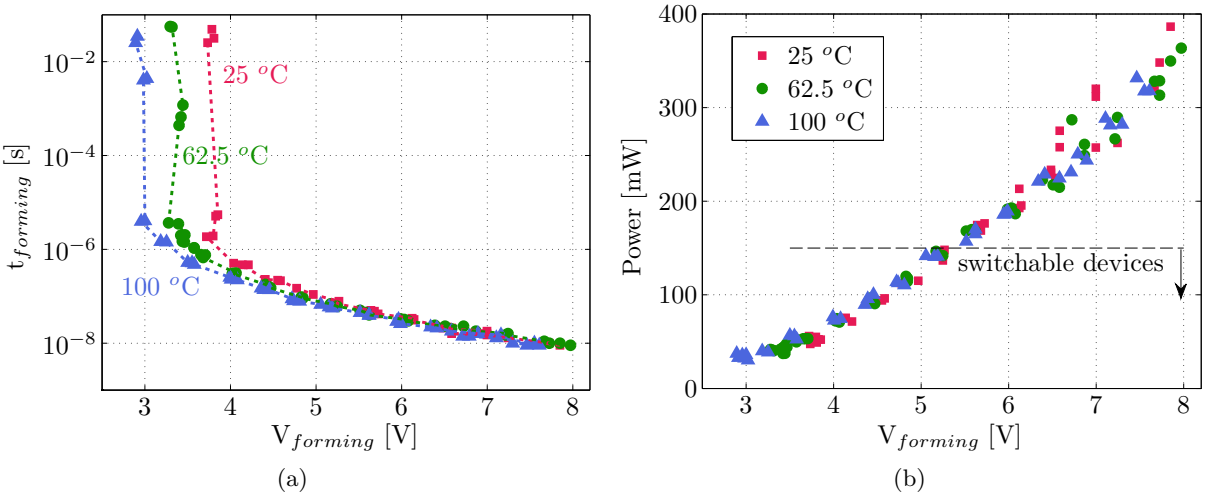

Figure 5.6: (a) Electroforming time as a function of voltage at three ambient temperature conditions; (b) Corresponding post-electroformed power level. When this power level was below 150 mW (indicated by dotted horizontal line), devices where found to be switchable.

In figure 5.6a, considering the 25 °C ambient temperature case first, it is clear that as long as $V_{forming}$ is greater than $\approx$ 4.5 volts, $t_{forming}$ increases roughly exponentially as $V_{forming}$ decreases. However, a much more drastic increase in $t_{forming}$ is observed for $V_{forming} < 4.5$ V. It is remarkable that $t_{forming}$ increases by almost five orders of magnitude when $V_{forming}$ decreases from 4 V to 3.8 V. The same type of behavior is observed for 62.5 °C and 100 °C ambient temperatures cases as well. However, as the ambient temperature increases, the voltage at which the drastic $t_{forming}$ increase is observed shifts toward lower $V_{forming}$.

Figure 5.7a shows the current and voltage levels at the end of the electroforming pulse (denoted

$I_{post-forming}$ and $V_{post-forming}$ in figure 5.3) for all the devices. The post-electroformed resistance ($R_{post-forming} = V_{post-forming}/I_{post-forming}$) of the devices are generally in the range of 120 Ω - 220 Ω as shown in figure 5.7b. Each resistance value in this figure is from a separate device, and calculated based on a single voltage and current value. As a result, for a given device it is not clear if the resistance is truly voltage dependent or if it is constant. The latter case would imply that higher electroforming bias gives rise to post-electroformed states that is slightly lower in resistance compared to lower electroforming bias. Regardless of which case is true, the resistance of the devices after electroforming is significantly lower the than resistance level in pristine state.

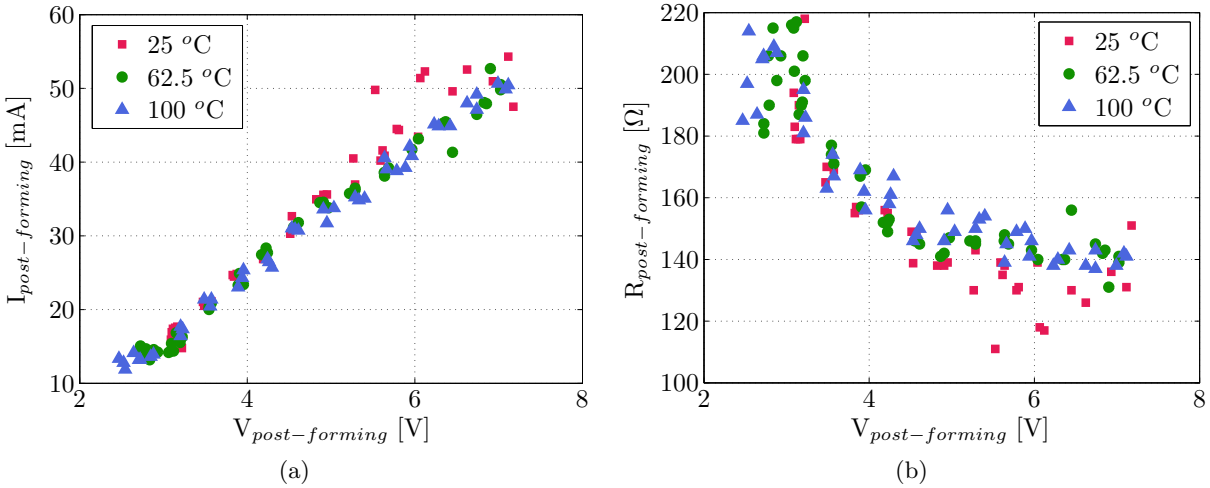

Figure 5.7: (a) Current vs. voltage at the end of the electroforming pulse for each device in figure 5.6; (b) Resistance at the end of the electroforming pulse ($V_{post-forming}/I_{post-forming}$)

After electroforming the devices with these single voltage pulses, DC voltage sweeps were conducted to examine their switching behavior. Devices with $V_{forming} < 5.5$ volts were found to be switchable, while those above this threshold were permanently stuck in a low resistance state. As discussed earlier, once the electroforming event is complete, the power dissipation as a function of time reaches a steady value. Figure 5.6b shows the post-electroformed power level as a function of $V_{forming}$ for all the devices in figure 5.6a. As $V_{forming}$ increases, the power dissipation level also increases. Depending on the electroforming condition, this power ranges between 25 mW to 400

mW. It is conceivable that when this post-electroformed power dissipation level is high, it causes significant damage to the filaments responsible for resistive switching. In figure 5.6b, $V_{forming}$ = 5.5 V corresponds to $\approx$ 150 mW power. Any device that experienced a power level higher than this after electroforming were not switchable (indicated by the dotted horizontal line).

Experiment 3: 'Pulse-Train'

Before describing the details of the 'pulse-train' experiment, some discussion is necessary in regards to the motivation for this study. A close examination of the various electroforming voltage profiles in figures 5.3a, 5.4, and 5.5 show that in addition to the large and drastic change in voltage during the electroforming event, there is also a gradual decrease in voltage across the device as soon as a pulse is applied (beginning from t = 0 s). This effect is not limited to the electroforming pulse only, it is observed in pulses that precede the electroforming pulse. Also, for the cases where $t_{forming}$ is longer than several microseconds, this gradual change in voltage stops after $\approx$ 2.5 μs. One example of this is shown in figure 5.8 below. This plot shows voltage profile of an un-electroformed device subjected to a 10 μs long voltage pulse with an amplitude less than what would be necessary to trigger electroforming. As soon as the pulse is applied, the voltage starts to decrease and it stabilizes after 2.5 µs.

One hypothesis is that these voltage decreases are caused by temperature increase of the device as a result of power dissipation or 'Joule heating'. Since TiO_2 is semiconducting, the conductivity of the device should increase as the temperature rises. An increased conductivity, or decreased device resistance, should lower the voltage over the device as observed in these plots. If the time scale of the applied voltage pulse is longer than the thermal time constant of the system, then the Joule heating related voltage decrease should only be observed until the device reaches thermal steady state. Assuming the voltage decrease shown in figure 5.8 is a result of Joule heating, then

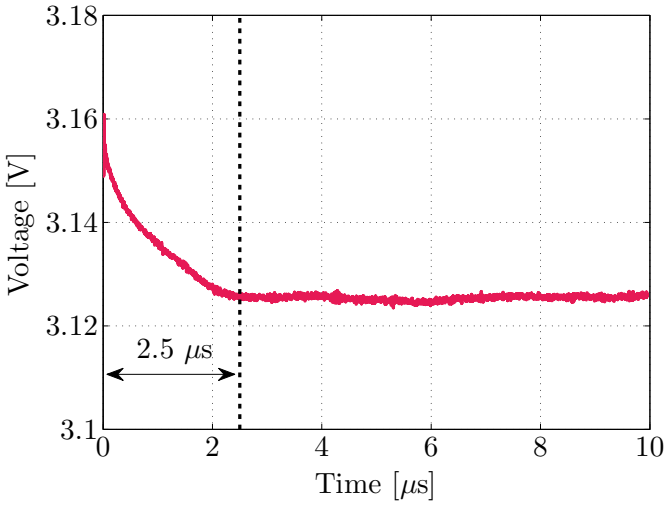

Figure 5.8: Voltage across a device prior to electroforming subjected to a 10 µs long pulse with V_p = 1.6 V. The voltage shows a clear decrease for the first 2.5 µs, and then stabilizes. The experiment was conducted at 100 °C ambient temperature.

this suggests a thermal time constant of the system of ≈ 2.5 µs, at which point the temperature reaches a steady value. The 'pulse-train' experiment was designed to explore the role of this time constant on the electroforming characteristics. A comparison between this experimentally observed ≈ 2.5 µs time constant and the actual thermal time constant predicted by thermal simulations will be presented in the Thermal Modeling section.

For the 'pulse-train' experiment, the devices were subjected to pulse-trains containing a fixed number of pulses with a fixed pulse width, amplitude, and time gap, t_{gap}, between adjacent pulses. While keeping all other parameters constant, the voltage amplitude was gradually increased in steps of 0.1 V from one pulse-train to the next until electroforming was observed. The time gap between consecutive pulse-trains was ≈ 1 second. A schematic of a pulse-train is shown in figure 5.9. This electroforming procedure was carried out over many devices with varying values of t_{gap}, ranging from 3 ns to 3 µs. The lower limit of t_{gap} (3 ns) was set by the shortest time gap allowed by the Agilent pulse source. The upper limit of 3 µs was chosen so that it was higher than the experimentally observed time constant of 2.5 µs.

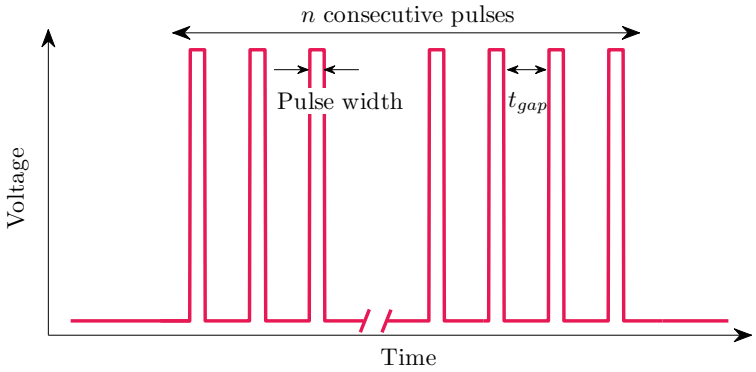

Figure 5.9: Schematic of pulse-train

Figure 5.10a shows $V_{forming}$ corresponding to different values of t_{gap} where trains of 100 pulses with 100 ns width were applied to trigger electroforming. For $t_{gap} \gtrsim 2$ µs, $V_{forming}$ approached the same value as a single 100 ns pulse (as obtained from 'fixed pulse width' experiment, indicated by the upper dotted line). However, as t_{gap} is reduced below 2 µs, $V_{forming}$ started to decrease rapidly. For the minimum possible t_{gap} of 3 ns, $V_{forming}$ was very close to the value for a single 10 µs long pulse (obtained again from 'fixed pulse width' experiment, indicated by lower dotted line). This 10 µs value is not a coincidence since 100 x 100 ns = 10 µs. Similar experiment with pulse trains containing 20 pulses with 50 ns width also revealed similar result as shown in figure 5.10b. With $t_{gap} = 3$ ns, the electroforming voltage was close to that of a single 50 ns pulse, and with $t_{gap} = 3$ µs it was close to that of a single 1 µs long pulse (20 x 50 ns = 1 µs). In general, $V_{forming}$ decreased with $t_{gap} \lesssim 2$ µs and approached a value corresponding to $V_{forming}$ of a single long pulse with total duration of all the individual pulses. This pulse-train experiment gives yet another indication of importance of this 2-3 µs time constant. If this is indeed the thermal time constant of the system, then for cases where t_{gap} is less than this value the device does not have enough time to cool down from the prior pulse. The effects of consecutive pulses begin to accumulate under this condition. This effect is more clearly seen by looking at the individual pulses within each pulse train. Figure 5.11 shows pulse train containing one hundred 100 ns wide pulses with t_{gap} of 3 ns, 250 ns, and 3

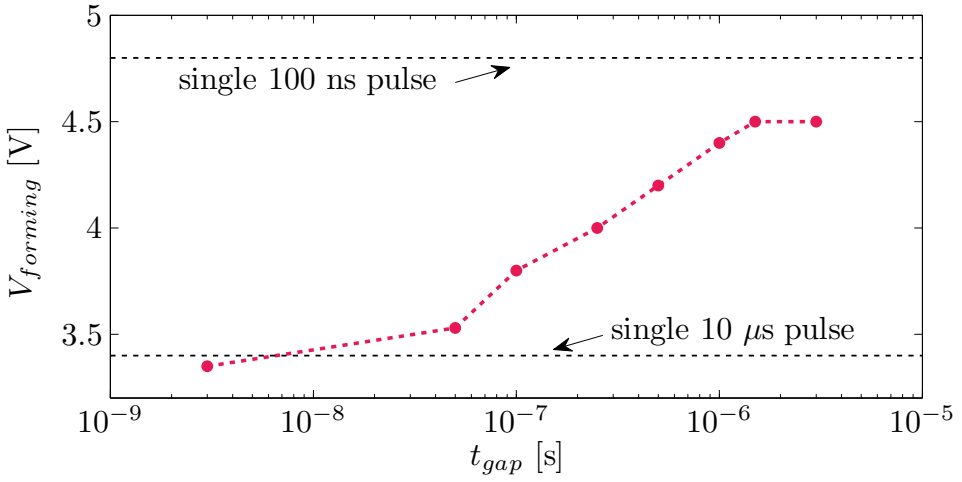

(a)

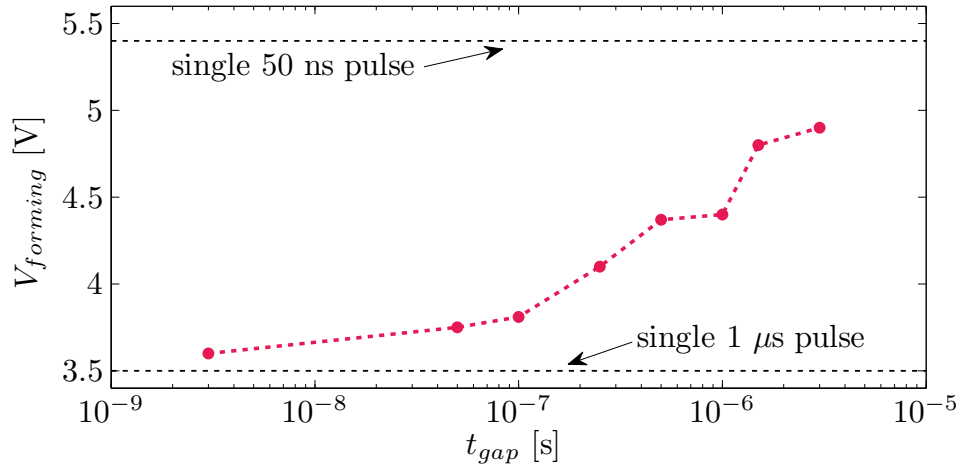

(b)

Figure 5.10: (a) $V_{forming}$ as a function of t_{gap} for pulse-trains containing 100 pulses with 100 ns pulse width each; (b) $V_{forming}$ as a function of t_{gap} for pulse-trains containing 20 pulses with 50 ns pulse width each. In both plots, upper horizontal dotted line indicate $V_{forming}$ (as obtained from 'fixed pulse width' experiment) for a pulse width that is equal to the width of a single pulse in the pulse-train. The lower horizontal dotted line indicated $V_{forming}$ for a pulse width that is equal to the aggregate width for all the pulses in the pulse-train.

μs. For clarity, alternating red and blue colors have been used to delineate adjacent pulses. Also, the time period corresponding to t_{gap} have been removed from the plot in order to get a better view of the pulses. For the t_{gap}= 3 μs case (figure 5.11a), the voltage across the device for each pulse looks identical to the preceding pulse until one of the pulses suddenly triggers electroforming. However, with t_{gap}= 3 ns (figure 5.11c), this is clearly not the case. The voltage decrease induced by each pulse carries over to the next pulse seamlessly and the electroforming event is spread out over multiple pulses. When t_{gap} is in-between these two extreme cases (figure 5.11b), only a portion of the effect from each pulse is carried over to the next pulse in the train.

Discussion

The pulsed experiments described in the last three sections provide significant insight into the electroforming event of TiO_2 based resistive switching devices. Although individually each experiment highlights certain aspect of electroforming, some subtle factors, which may not be immediately obvious, can only be understood when all the findings are considered together. Electroforming studies similar to the ones described in the 'fixed pulse amplitude' section have recently been reported by Lee *et al.* [102, 103] on $SrTiO_x$, TiO_y, and ZiO_z based devices. Their work qualitatively yielded similar results in terms of the $t_{forming}$ dependence on pulse amplitude as shown in figure 5.12. In an attempt to explain the observed behaviors, the authors have claimed that two different physical mechanisms are at play depending on the voltage amplitude used to trigger electroforming. For high biases, it is considered to be a purely electrically driven dielectric breakdown, whereas for low biases the breakdown is claimed to be thermally assisted.

The $t_{forming}$ and $V_{forming}$ relationship obtained from our experiments in figure 5.6a show a very strong dependence on ambient temperature when $V_{forming}$ is low. Based on this, it is logical to conclude that the breakdown process under low biases is thermally assisted. For higher biases,

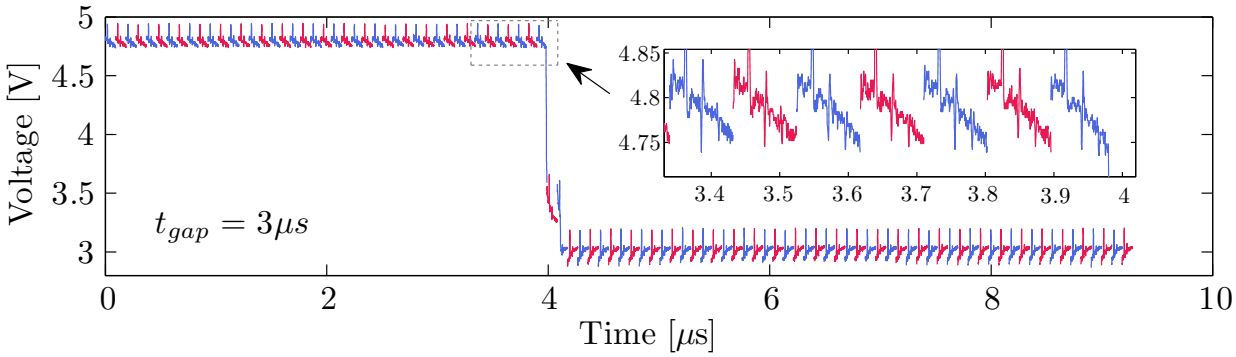

(a)

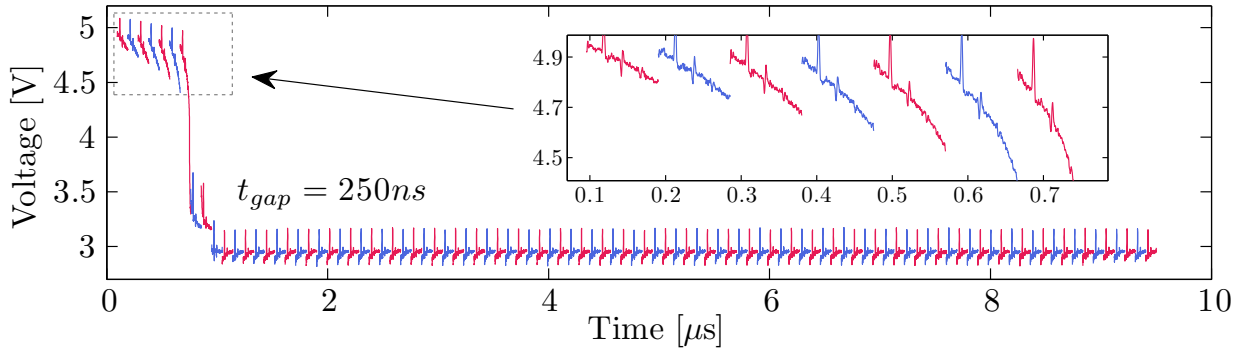

(b)

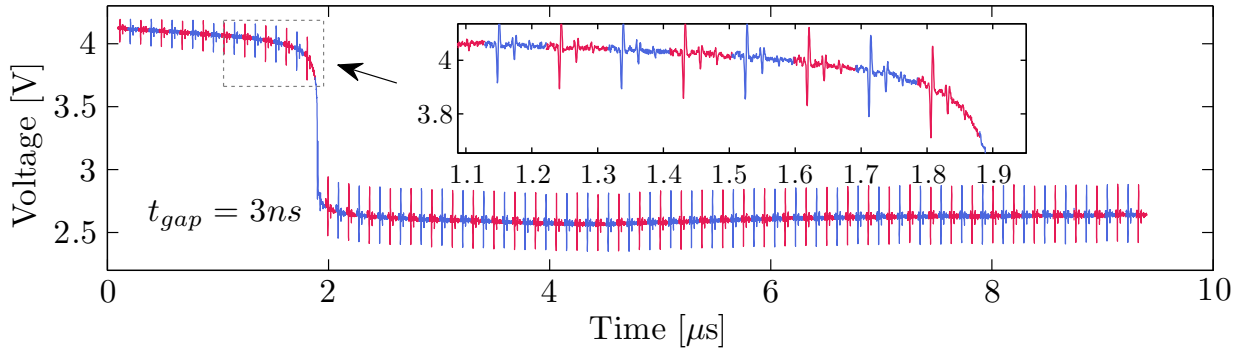

(c)

Figure 5.11: All pulse-trains contain 100, 100 ns wide pulses. For clarity, t_{gap} time period have been removed from each pulse train so that adjacent pulses can be compared easily. Adjacent pulses have been alternately colors in order to separate one pulse from another. (a) Pulse-train with $t_{gap} = 3$ µs; (b) pulse-train with 250 ns gap; (c) pulse-train with 3 ns gap. Inset in each case shows a closer view of the individual pulses. In (a), where $t_{gap} = 3$ µs, adjacent pulses show little interaction; in (c), where $t_{gap} = 3$ ns, effects of each pulse is carried over to next one to such an extent that it is difficult to distinguish one pulse from another.

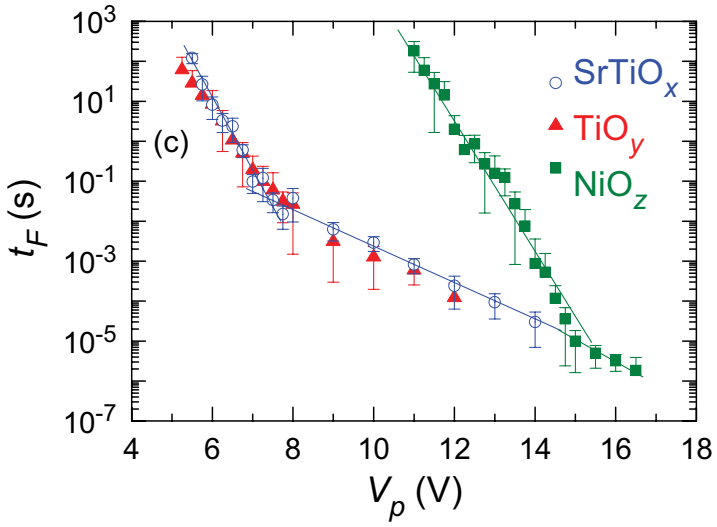

Figure 5.12: Electroforming time vs. voltage for three different oxides as measured by Lee *et al.* [102].

there are no pronounced differences between the three ambient temperature cases. However, this is not sufficient information to assert that this process is purely electrically driven. As discussed in the previous section, both the gradual decrease in voltage across the device prior to electroforming and the 2.5 µs long time constant observed for long pulses and in the pulse train experiments indicate that thermal events, resulting from Joule heating, may play a major role in electroforming under all biasing conditions. Joule heating related effects should be more pronounced at higher voltages due to higher power dissipation levels. This could, in fact, make the ambient temperature dependence appear less significant if the temperature increase due to Joule heating is higher than the range over which ambient temperature is varied. The correlation between these observations and Joule heating will become clearer as the thermal modeling results are discussed in the next section and the next chapter.

The experimental results discussed in the pulse-train section showed that as the time gap between consecutive pulses were made larger, $V_{forming}$ approached a value as if the device was electroformed with a single pulse. However, for both 50 ns and 100 ns pulse-train cases, $V_{forming}$

was found to be slightly below the value observed for true single pulse as indicated by the upper dotted lines in both plots. For both 50 ns and 100 ns pulse width cases, multiple device were tested with $t_{gap} = 3$ µs, and all of them failed to produce $V_{forming}$ that was exactly equal to the value indicated by the dotted lines. This slightly lower $V_{forming}$ value may be an indication that the breakdown mechanism is probabilistic in nature. Since in this pulse-train experiment the devices experience many pulses at any given voltage amplitude, there is a higher chance of electroforming occurring at a lower voltage compared to the single pulse experiments. A related effect can be observed in the electroforming behavior shown in figure 5.11a. Here, electroforming is not trigged by the very first pulse in the pulse-train as would be expected if it was only dependent on the pulse amplitude alone. Rather, although the effect of successive pulses seem independent of each other, after experiencing a few pulses the device suddenly electroforms. This again indicates that at any given voltage amplitude and pulse width, there is a finite probability of electroforming the device. Even though there is no observable influence of one pulse on another, electroforming can occur during any one of the pulses within the pulse-train. No cumulative changes need to occur within the device from one pulse to the next for this to be the case.

Increase in current through an oxide film as a result of electrical stress has been studied extensively in the context of gate oxide reliability in MOSFET structures. It is generally accepted that prolonged electrical stress causes defects to accumulate in the oxide which initially gives rise to increased leakage current and then eventually leads to permanent breakdown [104, 105, 106, 107]. Figure 5.6a shows that electroforming time increases drastically as the voltage is reduced below 4 volts. As a result, investigating the transient current-voltage characteristics of the device at low voltages using the pulsed experimental setup becomes intractable. Additionally, in the low voltage regime where the pristine resistance of the device is very high (> 10 kΩ), the pulsed experimental setup is unable to detect small changes in the device resistance. In order to see how such low volt-

age electrical stress affect the devices, a prolonged DC voltage stress experiment was conducted. For this, four different devices were stressed at +1 V for 1 minute. During this stress period, the current through the devices was recorded every second. This stress was followed by a wait period, t_{wait}, with zero bias applied to the device. After the wait period, the + 1 V stress and current measurement was resumed again. Each device had a specific t_{wait} value, which ranged from 5 s to 5000 s. This voltage stress and wait sequence was repeated 7 consecutive times. Figure 5.13 shows the current level as a function of stress time for all four cases. Here, adjacent stress periods are alternately colored. During each stress period, the current increased with time and during each t_{wait} period the current decreased. Longer t_{wait} periods generally lead to a larger decrease in current. But, even for the longest case, $t_{wait} = 5000s$, the current did not decease as much as it increased during the previous 1 minute stress period. As a result, for all four devices, the net current at the end of the seven stress cycles was higher than what was observed initially, prior to any stress. This is a clear indication that continual electrical stress causes changes to the oxide layer. Effects of this change diminishes very slowly over time. This finding is in contrast to the results obtained from the pulse-train experiments where t_{gap} was long (greater than the thermal time constant). There, consecutive pulses did not exhibit any sustained change in the device current-voltage characteristics prior to electroforming. The major difference between these DC experiments and the pulse-train experiments is the temperature of the devices. Due to the lower bias amplitude used during these DC experiments, the amount of Joule heating was negligible. As a result, the temperature of these devices never increased. However, for the pulse-train cases, the temperature increased during each voltage pulse, and the devices cooled slowly over time from an elevated temperature during the t_{gap} period. If the recovery of the any changes induced by the electric field is assisted by elevated temperature, then cumulative changes to the TiO_2 layer would be more visible for the DC cases compared to the high amplitude pulse-train cases, consistent with the results obtained here.

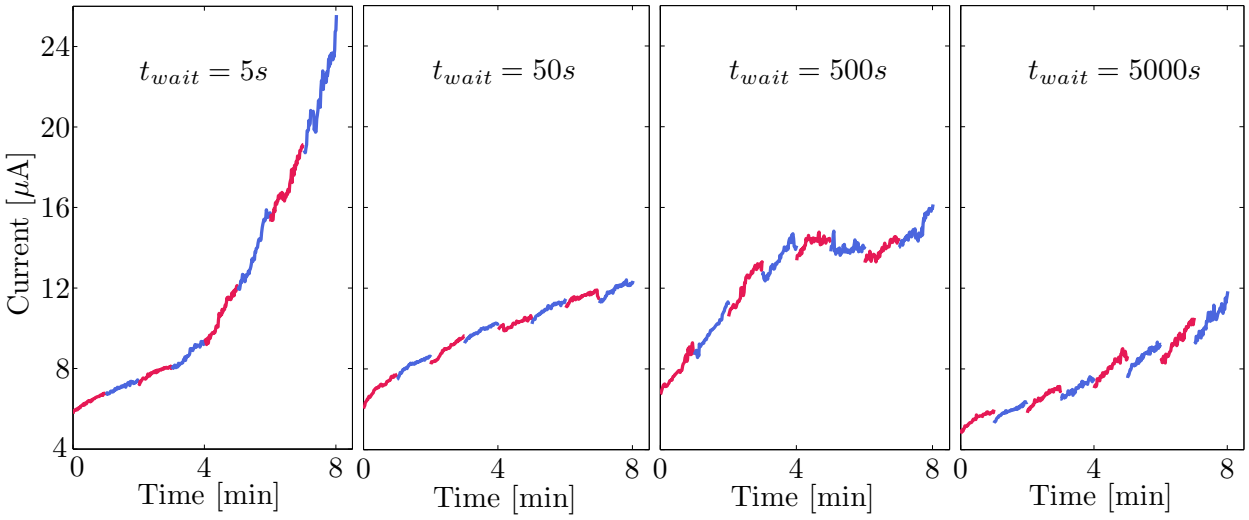

Figure 5.13: Increase in current as a result of subjecting four different (pristine, un-electroformed) devices to repeated +1 V DC stress for 60 s with t_{wait} time gap between adjacent stress periods. During the stress periods, current measurements were made with 1 second interval. Adjacent stress periods are alternately colored.

5.3 Thermal Modeling

The purpose of the thermal model presented in this section is to correlate some of the transient observations from the pulsed electroforming experiments to the thermal events that is believed to be the root cause. Using this model, quantitative comparison can be made regarding the thermal time constant of the device and the observed time constant from electroforming measurements (which, until now, have been attributed to thermal effects without any concrete support). It can also be used to estimate the temperature excursion leading up to the electroforming event under various biasing condition. In this section, the model will be described in detail and the thermal time constant will be extracted. Estimation of temperature excursion will be explored in the next chapter.

Equation 5.6 below was used to solve for the transient thermal profile of the device.

$$Q = \rho C_p \partial T/\partial t + \nabla \cdot (-k_{th} \nabla T) \tag{5.6}$$

Here, Q is heat source, ρ is density, C_p is heat capacity, k_{th} is thermal conductivity and T and t are temperature and time, respectively. This equation was implemented on a 2-D geometry with axial symmetry that had the same material layers as the crossbar device. The geometry is shown in figure 5.14. The radius of the top electrode was chosen so that the area of the device implemented in this model matched the area of the 5 µm x 5 µm device. The 2-D axial geometry was preferred rather than a full 3-D model due to computational simplicity. The model was solved using Comsol Multiphysics finite element solver. Prior to solving the model, all the exterior boundaries (highlighted in red), except for the bottom boundary, were set to thermal insulation condition. The temperature of the bottom boundary was fixed at the ambient temperature throughout the simulation. This is because during the electroforming measurements this surface is in contact with the probe station chuck where the ambient temperature is controlled. Also, no thermal interface resistances were taken into account between any of the adjacent layers. The initial temperature of each layer was set to the ambient temperature. The material parameters used for each of the layers are given in table 5.1.

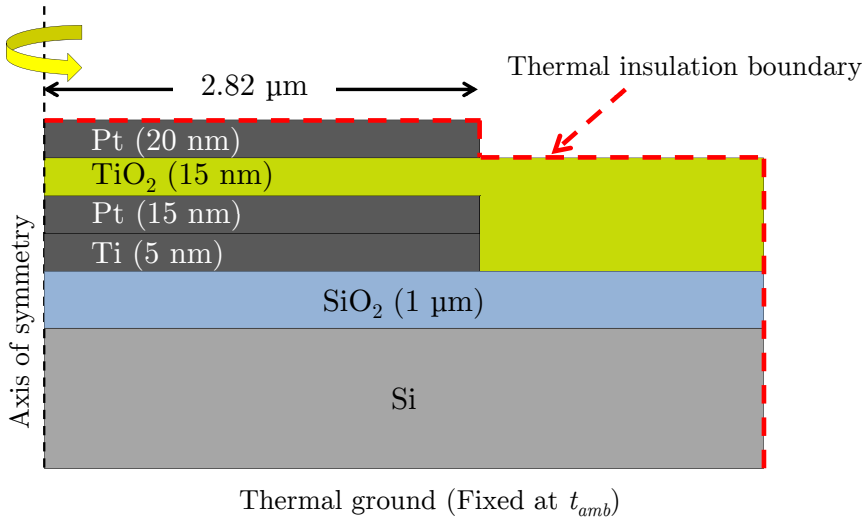

Figure 5.14: Device geometry for thermal simulation

In order to estimate the thermal time constant, $\tau_{thermal}$, of this system, a constant power

Table 5.1: Material parameters for thermal simulation

Material	k_{th} (bulk) [W/(m K)]	k_{th} (film) [W/(m K)]	ρ [kg/m^3]	C_p [J/(kg K)]
Si	148	148	2320	705
SiO_2	1.3	1.3	2648	733
Pt	71.6	7.16	21450	130
Ti	22	2.2	4500	520
TiO_2	11.7	1.17	4230	693

dissipation level was set for the TiO_2 layer (constrained only to the area directly below the top electrode) and the simulation was run for 10 µs. Figure 5.15 shows the resulting normalized average temperature increase as a function of time. For this simulation, the actual power dissipation level or the final temperature is not important since none of these factors would impact $\tau_{thermal}$. The simulations were carried out for two cases. For the first case, the thermal conductivity of all layers were assumed to be the same as bulk value for each material. However, thin films generally have lower thermal conductivity. To estimate the effect of this, the conductivity of the Pt, Ti, and TiO_2 layers were decreased by an order of magnitude (k_{th} (film) in Table 5.1). As the results in figure 5.15 show, the difference in thermal time constant between the two cases is negligible. This is because the thermal time constant of this system is dominated by the thermal conductivity and the heat capacity of the SiO_2 layer. As the temperature profiles indicate, when the power dissipation is constant, the device reaches thermal steady state in $\approx$ 3 µs. This results is very close to the 2.5 µs time constant observed during the pulsed electroforming experiment in figure 5.8. This is a strong indication that Joule heating and associated thermal steady state is responsible for some of the voltage transients observed prior to electroforming. The thermal effects also account for the interactions observed between adjacent pulses in the pulse-train experiments when $t_{gap} < \tau_{thermal}$ condition was true.

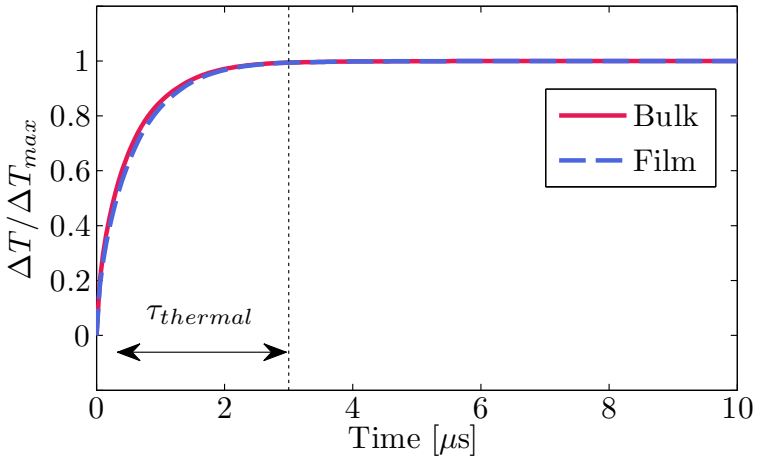

Figure 5.15: Normalized temperature rise as function of time. The curves labeled 'Bulk' and 'Film' are obtained using k_{th} (bulk) and k_{th} (film) values listed in Table 5.1, respectively. All other parameters are identical for the two cases. The thermal time constant, $\tau_{thermal}$, is ≈ 3 µs for both cases.

5.4 Conclusion

The pulse induced electroforming method discussed in this chapter provides a level of control and insight into the electroforming process of TiO_2 based resistive switching devices that cannot be achieved using a DC electroforming procedure. These studies reveal that temperature plays a very large role in determining the relationship between electroforming time and voltage. For low electroforming voltages (< 4 V), the role of ambient temperature is readily apparent. For these cases, small changes (30-40 °C) in ambient temperature can change the electroforming time by 4-5 orders of magnitude. For high electroforming voltages (> 4 V), although the ambient temperature does not seem to play a role, temperature effects nevertheless cannot be ignored. For these cases, due to higher level of power dissipation, Joule heating induced temperature increase affect the electroforming characteristics. Evidence of Joule heating is apparent in the transient voltage, current, and resistance profiles of the devices prior to electroforming. The time constant observed during the pulsed experiments has been verified to be related to thermal time constant of the device with the aid of thermal modeling and simulation. Therefore, for these cases, much of the effect of

ambient temperature change may be obscured by the significantly higher temperature change due to Joule heating. Overall, the pulse-induced transient studies discussed in this chapter highlight the importance of a closer examination of the thermal events associated with electroforming.

Chapter 6

Temperature Excursion During Electroforming

Time dependent electroforming studies discussed in chapter 5 highlighted the role of thermal events during the electroforming process. The relationship between electroforming time ($t_{forming}$) and voltage ($V_{forming}$) was observed to be highly affected by the ambient temperature for cases where $V_{forming}$ was small. For higher values of $V_{forming}$, it was argued that temperature rise due to Joule heating obscured the ambient temperature dependence. The pulse-induced electroforming experiments allowed for measurement of transient voltage and current profiles for the entire electroforming process. In this chapter, a method will be presented that uses those transient measurements to estimate the temperature change of the device prior to electroforming. The temperature values obtained using this method will be compared with predictions from thermal simulations (using the model presented in the last chapter). The combinations of results of these two methods will provide more insight into the role of thermal events that trigger electroforming.

Figure 6.1 shows the transient voltage profile of a device subjected to 250 ns pulses that eventually lead to electroforming. This plot was shown and discussed in detail in the previous chapter (5.3) and is repeated here for convenience. As discussed before, the voltage drop observed in this plot is a result of decrease in resistance of the device. The resistance decrease observed during the pre-electroforming pulse (one immediately preceding the electroforming pulse) was found to be

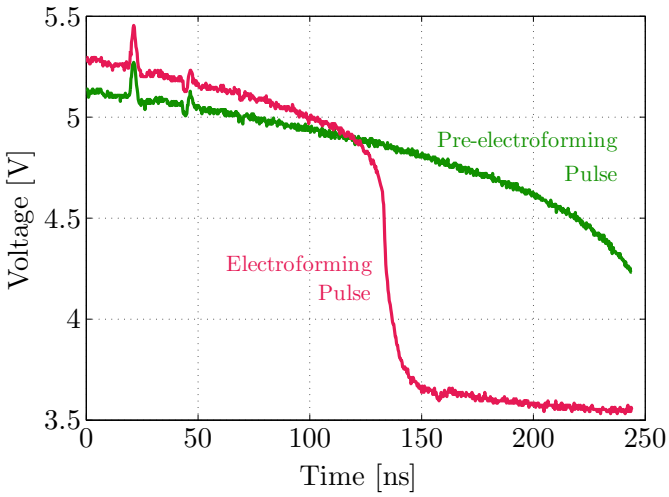

Figure 6.1: Transient voltage profiles of electroforming and pre-electroforming using 250 ns pulses

non-permanent in nature and repeatable. It was conjectured that some of this observed voltage change was a result of Joule heating due to power dissipation. If the temperature dependent resistance characteristics of the device (prior to electroforming) was known, then the transient current and voltage profiles could be correlated to the device temperature. The next section describes a method for obtaining the temperature dependent I-V characteristics, which is the first step toward estimating this temperature excursion.

6.1 Temperature Dependent Pulsed I-V

At first glance, determining the temperature dependent I-V characteristics seems rather straight forward. One can simply perform a DC voltage sweep and measure the current under various ambient temperature conditions. However, I-V relationships obtained using this method do not, in fact, reveal the true dependence on ambient temperature. If the application of voltage to the device causes significant power dissipation, it will alter the temperature due to Joule heating. As a result, the measured current would not correspond to the ambient temperature condition. In order to overcome this challenge, a pulsed I-V measurement method was implemented.

For the pulsed I-V measurement, the device was subjected to voltage pulses with a pulse width

of 15 ns and rise/fall time of 2.5 ns. The amplitude of the voltage pulse was increased for successive pulses and the voltage and the current measurements were made during the first 1 ns of the pulse (after the rise time, once the pulse reached full amplitude). Some select voltage pulses and the corresponding current profiles from this measurement are shown in figures 6.2a and 6.2b, respectively. The sampling period is highlighted on the figure. The effect of Joule heating is seen in this plot for cases were the voltage amplitude is high. Towards the end of these pulses, the voltage across the device started to decrease as the resistance decreased from the increased temperature. By sampling the voltage and current towards the beginning of the pulse, these effects were safely avoided. As a result, the I-V relationship captured using this method can be correlated to the known ambient temperature. This pulsed I-V method was carried out at 25 °C, 100 °C, 150 °C, and 200 °C. The resulting temperature dependent I-V characteristics are shown in figure 6.3a (solid lines).

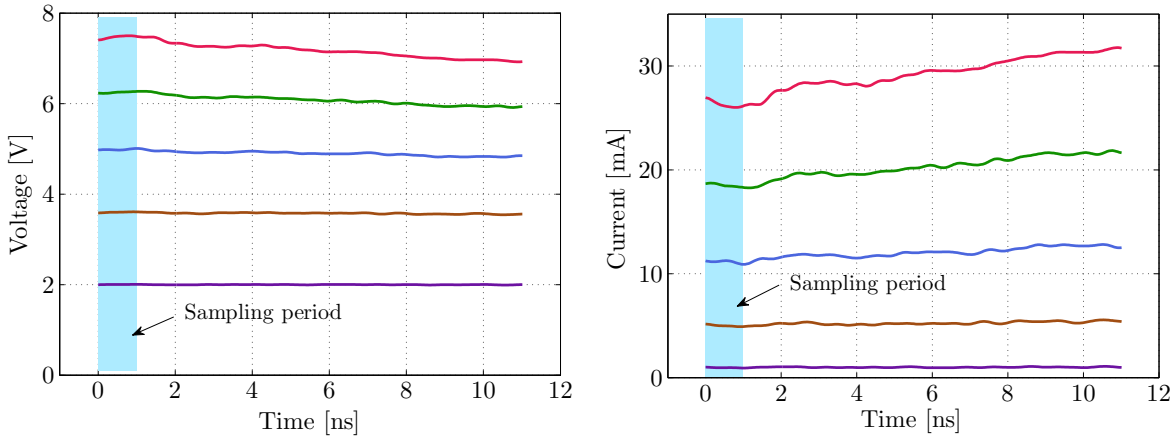

Figure 6.2: (a) Voltage and (b) profiles corresponding to several 15 ns pulses used for pulsed I-V measurements. The value of voltage and current are sampled during the first nanosecond of the pulse period (highlighted in blue) after the pulse rise-time.

The temperature dependent I-V data in figure 6.3a were collected under conditions such that the pulses used for the measurement would not induce electroforming. This meant limiting both the pulse amplitude and the width. As a result, the voltage range (the x-axis in figure 6.3a) in

some cases does not extend as far as would be desirable. To extend the I-V data over a larger range of voltage, curve fitting was performed (fitted curves shown using dotted lines). The equations corresponding to each fit is given below. Given the shape of the I-V profiles, it was difficult to fit each curve with a single functional form. As a result, a piecewise fit was performed as indicated in equations 6.1-6.4.

$$25\ ^\circ\text{C} : I = \begin{cases} 7.09\times10^{-5}V^3 - 3.19\times10^{-4}V^2 + 4.06\times10^{-4}V - 1.07\times10^{-4} & \text{if } V \leq 5.6 \\ 3.80\times10^{-4}V^2 - 7.3\times10^{-3} & \text{if } V > 5.6 \end{cases} \tag{6.1}$$

$$100\ ^\circ\text{C} : I = \begin{cases} 7.69\times10^{-4}V^2 - 3.78\times10^{-3}V + 4.91\times10^{-3} & \text{if } V \leq 5 \\ 4.23\times10^{-4}V^2 - 5.34\times10^{-3} & \text{if } V > 5 \end{cases} \tag{6.2}$$

$$150\ ^\circ\text{C} : I = \begin{cases} 8.50\times10^{-4}V^2 - 3.47\times10^{-3}V + 3.91\times10^{-3} & \text{if } V \leq 4.45 \\ 3.78\times10^{-4}V^2 + 9.93\times10^{-4}V - 6.59\times10^{-3} & \text{if } V > 4.45 \end{cases} \tag{6.3}$$

$$200\ ^\circ\text{C} : I = \begin{cases} 3.61\times10^{-4}V^2 + 1.46\times10^{-3}V - 6.43\times10^{-3} & \text{if } V > 4.2 \end{cases} \tag{6.4}$$

Analysis of the data in figure 6.3a revealed that there is no simple method of predicting the I-V characteristics for a given temperature based on the known I-V relationships for some other temperatures. Temperature coefficient of resistance (TCR), which describes how resistance of a material changes with temperature, can often be used to relate the temperature dependent I-V characteristics of a device between different temperatures. However, no single TCR value can consistently describe the data in figure 6.3a. As a result, within the range of 25-200 °C the best method of predicting the I-V relationship is to use interpolation. For temperature higher than 200 °C, extrapolation is used. For this, a 2-D fitting was performed using all four I-V curves as shown in figure 6.3b. Equation 6.5 represents this surface.

$$I = 2.78\times10^{-3} - 2.83\times10^{-3}V - 1.95\times10^{-5}T + 5.44\times10^{-4}V^2 + 1.12\times10^{-5}VT \tag{6.5}$$

Here, I, V, and T represent the current, voltage and temperature, respectively. Some representative I-V characteristics (e.g. at 300 °C and 400 °C), predicted based on this surface, are shown

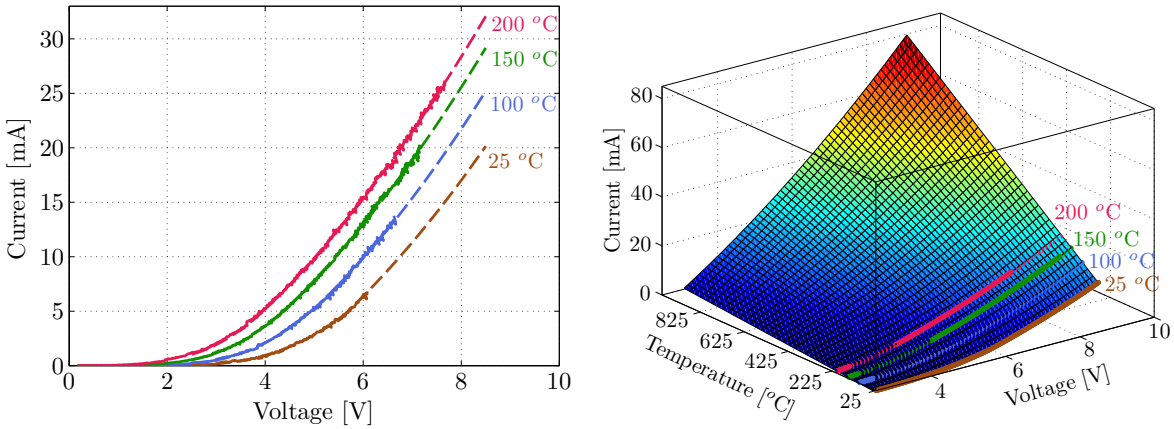

Figure 6.3: (a) Solid lines show pulsed I-V behavior for four different ambient temperatures, dotted lines show extrapolated I-V corresponding to equations 6.1-6.4; (b) 2-D surface fit of current as a function of voltage and temperature.

in figure 6.4. The data in this figure will sever as the basis for estimating the Joule heating related temperature rise, as will be described in the next section. For this fitting, voltages lower than 2.5 V were not considered, since for all electroforming experiments, the voltage pulse amplitude were above this limit. Therefore, temperature dependent I-V relationship in the range of 0-2.5 V is not needed.

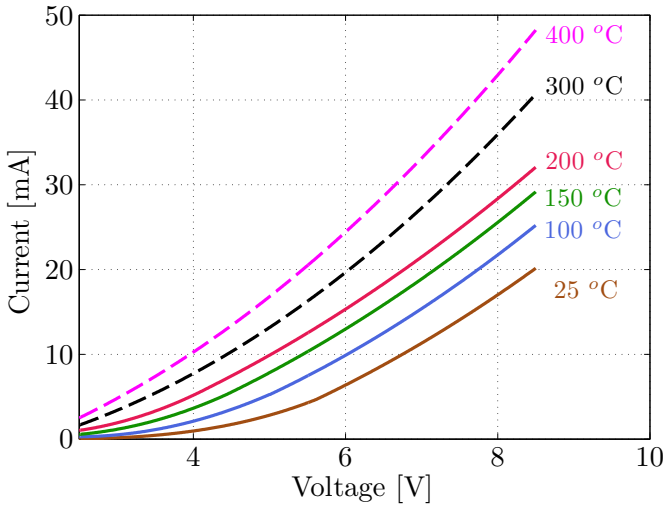

Figure 6.4: I-V curves corresponding to 25-200 °C are the same as the ones shown in figure 6.3a. 300 °C and 400 °C (dashed) are obtained from the 2-D surface fit based on figure 6.3b

6.2 Transient Temperature Extraction

In this section, the temperature dependent I-V data and the transient current and voltage profiles from electroforming experiments will be combined to extract the transient temperature profile during electroforming. The method is graphically illustrated in figure 6.5. Figure 6.5a and 6.5b shows the transient current and voltage profiles corresponding to 250 ns electroforming pulse. For any given time (indicated by the dotted line), there exists a specific current and voltage value. These values can be mapped onto the temperature dependent I-V data (figure 6.5c), and a temperature can be estimated by using interpolation. By repeating this process for the entire time range beginning from t = 0 s, a full temperature profile as a function of time can be generated as shown in figure 6.6.

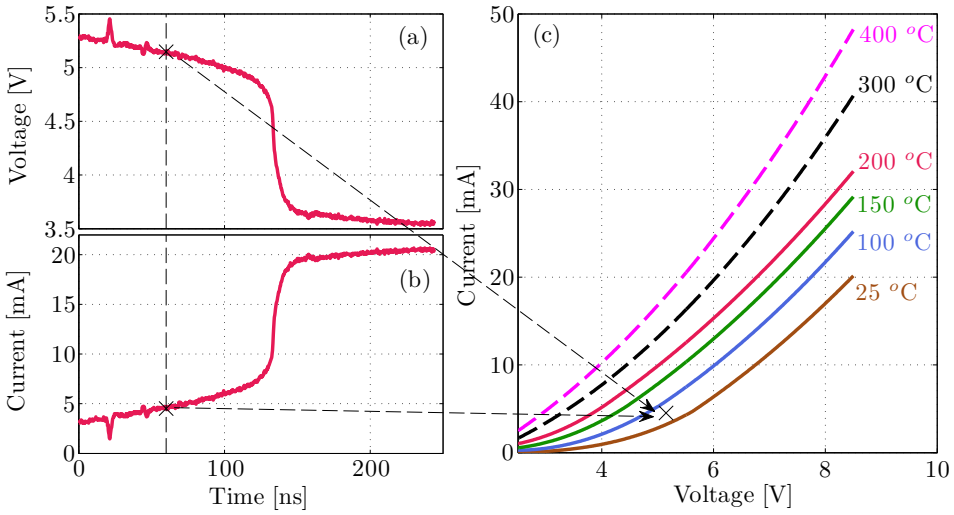

Figure 6.5: Transient voltage (a) and current (b) corresponding to a 250 ns long electroforming pulse; (c) voltage and current corresponding to the time indicated by dotted line is mapped onto the pulsed I-V data.

The method used to generate the temperature profile in figure 6.6 is based on two important underlying assumptions. The first assumption is that the current conduction behavior of the device is uniform. In other words, there is no localized area within the device where the electrical conductivity is higher than the rest. The second assumption is that the increase in current is due to an

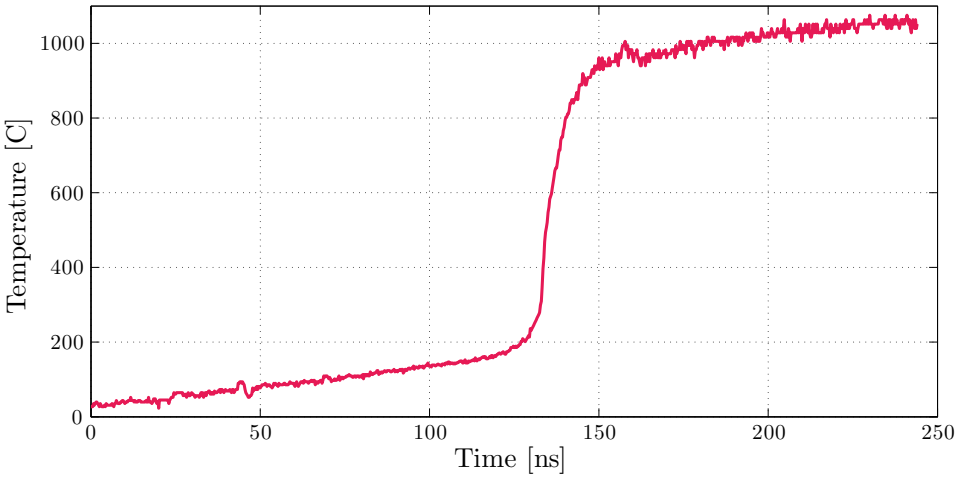

Figure 6.6: Extracted transient device temperature during electroforming

increase in device temperature (caused either by Joule heating or elevated ambient temperature) and not because of any other electronic effects. The extracted temperature profile is only valid as long as both of these assumptions are true. Therefore, when the device gradually transitions from uniform to filamentary electrical conduction mode, the extracted temperature values do not correspond to the actual device temperature. Examination of the transient voltage and current profiles do not reveal the time when this transition begins. Therefore the time range of validity for the extracted temperature profile cannot be directly identified. Beginning at t = 0, the device temperature will uniformly increase until the electrical conductivity begins to localize, causing the region of elevated temperature to also localize. A better understanding of the time range of validity of this method can be gained by correlating the measured power dissipation with thermal simulations, as will be discussed in the next section.

6.3 Comparison With Transient Thermal Simulation

The thermal model presented in the previous chapter was used to estimate the thermal time constant of the device and it was compared to the time constant observed during the pulsed-electroforming measurements. This model can also be used to estimate the transient temperature rise of the device.

Since the transient power dissipation is known for the entire duration of the electroforming pulse, this can be used as an input to the thermal model to simulate the temperature rise due to Joule heating. This process is schematically described in figure 6.7. The measured power is entered into the model as uniform power dissipated within the TiO_2 layer underneath the top electrode. The transient simulation then calculates the temperature profile based on this power dissipation level.

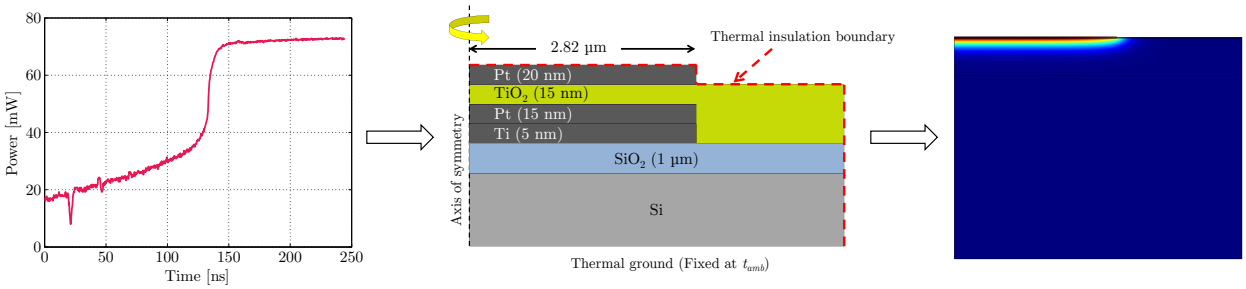

Figure 6.7: Procedure for thermal simulation. Measured power during electroforming is used as an input to the thermal model. The simulation calculates device temperature based on the transient power profile.

Figure 6.8 shows the simulated average temperature of the TiO_2 layer underneath the top electrode for the electroforming and the pre-electroforming pulses. These simulation results are compared with the extracted temperatures obtained using the method described in the previous section. Between the pre-electroforming and electroforming pulses, no simulation parameters were altered except the transient power profiles that corresponded to each of these pulses. The close match between the simulated and the extracted temperatures during the early portion of each pulse verify that this temperature rise is indeed due to uniform Joule heating. For the electroforming pulse, the uniform Joule heating assumption begins to break down around t = 120 ns. In other words, the increase in current observed after this time does not fit the model of temperature dependent resistance change. The current level suggests a much higher temperature rise than predicted by simulation based on the measured power dissipation.

It is known that after electroforming the current conduction localizes to a region that is a small

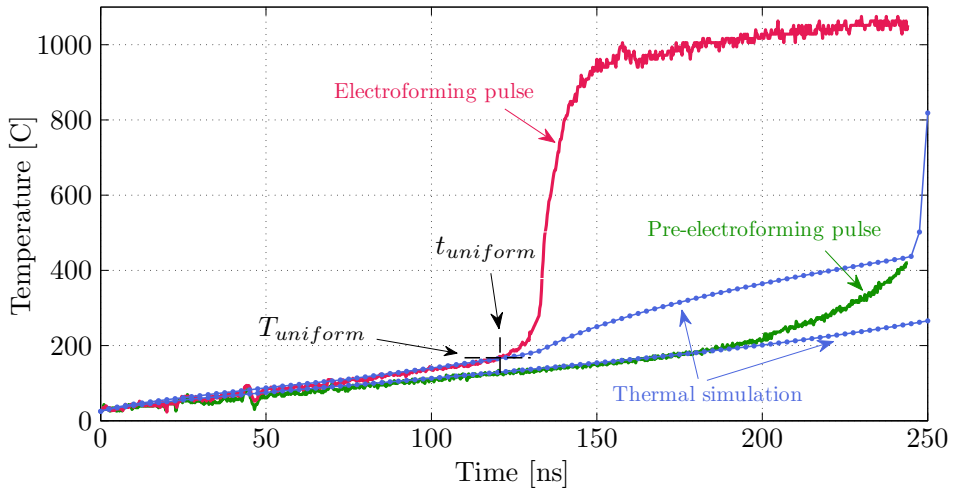

Figure 6.8: Comparison of extracted vs. simulated device temperature. The point where simulation prediction deviates from extracted temperature is marked as $t_{uniform}$.

fraction of the total device area. This region also has much higher electrical conductivity compared to the rest of the device. Therefore, the model of uniform Joule heating begins to breakdown as the device begins to transition from uniform to filamentary conduction mode. The measured current begins to be dominated by conduction through these regions of lower resistance. As a result, the device temperature can no longer be estimated using either the extraction method of the previous section or the thermal simulations discussed here. It is interesting that the uniform heating model also does not hold for the entirety of the pre-electroforming pulse. As discussed in the previous chapter, the pre-electroforming pulse did not produce any permanent changes to the resistance level of the device. This would suggest that no filament or localized regions of increased conductance was formed during this pulse. However, uniform Joule heating model clearly cannot be used to explain this increased current level. This means either a uniform resistance decrease took place which was not triggered thermally, or localized regions of increased conductance appeared which were not permanent in nature. Which one of these two mechanisms actually took place will be the central topic of discussion in the next chapter. However, it is clear that at a certain temperature, the device behavior starts to deviate from the uniform heating model. This temperature is marked

as $T_{uniform}$ and the time is marked as $t_{uniform}$ on figure 6.8 for the electroforming pulse. The voltage that corresponding to this time and temperature is called $V_{uniform}$. Figure 6.9 shows the relationship between these three quantities.

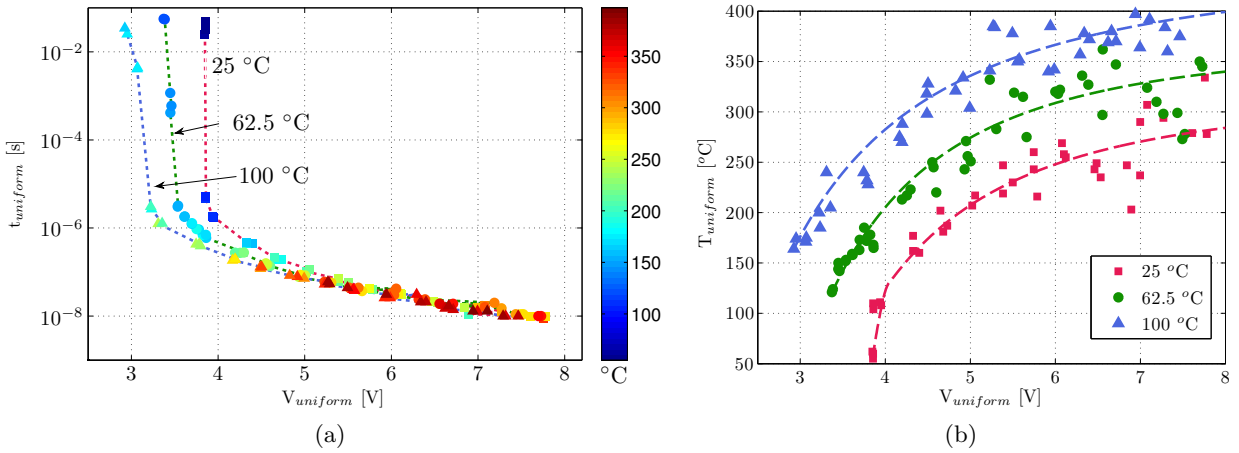

Figure 6.9: (a) $t_{uniform}$ vs. $V_{uniform}$. The color of each dot represents the temperature of the device at $t_{uniform}$; (b) The temperature values are shown explicitly as a function of $V_{uniform}$.

Figure 6.9a looks very similar to the electroforming time vs. voltage plot in figure 5.6a. The main difference between these two plots are the definition of the time and voltage. Instead of arbitrarily defining these parameters based on the inflection point of the electroforming voltage curve (as was done for figure 5.6a), the time, voltage, and temperatures here are more precisely defined based on physical events related to Joule heating. Each marker in figure 6.9a is colored according to $T_{uniform}$. This plot shows that the relationship between time and voltage cannot simply be evaluated based on the known ambient temperatures. For all three of the curves, the device temperature gradually increases with increasing voltage amplitude due to higher Joule heating. Considering the 25 °C curve, even for the lowest voltage (3.8 V), the device temperature is at least 25 °C higher than the ambient. This difference becomes greater than 250 °C as the voltage amplitude increase to 7.5-8 V. Comparison of the three curves reveal that for any given $t_{uniform}$, the difference in $T_{uniform}$ is roughly the same as the difference in ambient temperature. This is most apparent in the low

voltage (3-4.5 V) regime. In this region, every 37.5 °C increase in temperature reduces $V_{uniform}$ by $\approx$ 0.48 V. The $T_{uniform}$ as a function of $V_{uniform}$ is shown more explicitly in figure 6.9b for all three ambient temperature conditions.

6.4 Summary Of Observations

Before attempting to fit the data in figure 6.9a to any model, it is important to summarize some of the key findings from the various pulsed experiments. These are listed below.

1. The effect of multiple consecutive pulses prior to electroforming is not cumulative as long as the time gap between adjacent pulses is longer than the thermal time constant of the device. This was observed during the 'fixed pulse width' and the 'pulse-train' experiments described in the previous chapter. An exception to this scenario was observed during the DC stress experiments. In those cases, the increase in electrical conductivity of the devices as a result of electrical stress decreased very slowly once the stress was removed, and even with very long periods (5000 seconds) of no electrical stress, the conductivity did not return to the original levels of a pristine device. This may be related to the temperature of the device during the period after the electrical stress is removed. Because of the low voltage amplitudes (1 V) used during the DC cases, the temperature increase was negligible. However for the pulsed voltage experiments, the voltage amplitudes were much higher ($>$ 3 V) and this led to significant temperature rise.

2. Increasing the ambient temperature always lowers $V_{uniform}$ for any given breakdown $t_{uniform}$

3. Temperature increase due to Joule heating has the same effect on $V_{uniform}$ as temperature increase due to ambient heating. This fact was explicitly demonstrated in figure 5.10 using the 'pulse-train' experiments. In those experiments, the ambient temperature was held constant. However, Joule heating from consecutive pulses were found to lower the electro-

forming voltage. At first glance, this statement may seem to contradict the data in figure 6.9a where higher $V_{uniform}$ always corresponds to higher $T_{uniform}$. However, it must be kept in mind that $T_{uniform}$ is not independent of $V_{uniform}$, since it is caused by Joule heating. Also a high $V_{uniform}$-$T_{uniform}$ combination always produces shorter $t_{uniform}$ compared to a low $V_{uniform}$-$T_{uniform}$ combination.

4. The time denoted, $t_{uniform}$, does not necessarily represent the point of irreversible resistance change of the device. It simply represents the time where the resistivity change of the device can no longer be explained by uniform Joule heating. The change in resistivity accelerates beyond this point and eventually results in localized conduction. Therefore, this time is treated as the onset of localization.

6.5 Mechanism

The electroforming process as seen in figure 6.8 can be separated into three distinct regions. The first regions is from t=0 to t=$t_{uniform}$, where the decrease of the resistance has been determined to be due to Joule heating. This period is followed by the second region where rapid decrease of resistance occurs over localized areas of the device. Although this localization has not been directly demonstrated yet (other than the fact that uniform Joule heating model cannot explain this rapid decrease), gradual appearance of localized morphological changes during this time period, to be discussed in the next chapter, will confirm this statement. The third and final region is where the rapid resistance decrease comes to an end and the device assumes a permanent low resistance. As discussed in chapter 2, after this period many conductive filaments of reduced phases of TiO_2 are generally found within the device.

The data in figure 6.9 represents the conditions at the onset of localization of current conduction. The objective here is to come up with an explanation of this current localization that is consistent

with the key observations listed in the previous section. The literature review in chapter 2 revealed that the mechanism of electroforming in TiO_2 based devices is believed to be caused by migration of oxygen vacancies in response to the applied electric field. However, why such migration would lead to non-uniform electrical conduction remains unknown. One proposal, in attempting to explain this, is the fast migration of oxygen vacancies along grain boundaries [56, 51]. According to this, conductive filaments can begin to form due to these localized fast vacancy migration paths. How the kinetics of such migration fit with the measured data will be examined shortly.

Besides this vacancy migration model, which is popular in the resistance switching community, several other models of oxide breakdown exist. Most of these models were developed in relation to studies in gate oxide reliability in MOSFET devices. These are often referred to as time dependent dielectric breakdown (TDDB) studies. The experimental procedures are generally identical to the ones presented here for the TiO_2 based devices. For TDDB studies, oxide based capacitor type devices are stress with constant electric field until a sudden increase in current is observed indicating dielectric breakdown [108, 109, 110, 104, 111]. Two models that are often invoked to explain the TDDB data are the 'E' model and the '1/E' model [112, 113, 114, 115]. The 'E' model is based on thermodynamic free energy considerations and is also referred to as the 'Thermo-chemical Model'. The '1/E' model on the other hand is based on the assumption of hole injection assisted breakdown, and often referred to as the 'Hole Injection Model'.

For convenience of discussion and in order to stay consistent with other literature reports, from now on $t_{uniform}$ will be referred to as t_{bd}, the breakdown time; $V_{uniform}$ will be referred to as V_{bd}, the breakdown voltage; and $T_{uniform}$ will be referred to as T_{bd}, the breakdown temperature.

The general form of functional dependence between t_{bd}, T_{bd}, and the effective activation energy, E_{eff}, predicted by all three of these models is shown in equation 6.6.

$$t_{bd} \propto exp\left(\frac{E_{eff}\left(\xi_{ox}\right)}{k_B T}\right) \tag{6.6}$$

In this general from, E_{eff} is a function of the applied electric field, ξ_{ox}, which is calculated by dividing V_{bd} by the thickness of the oxide layer, which is 15 nm for all the measured devices (under the assumption that the voltage drops linearly over the oxide layer). The empirical relationship between E_{eff} and ξ_{ox} can be obtained from the data in figure 6.9a. Based on this empirical relationship, the validity of each of the models can be judged. From figure 6.9a, E_{eff} associated with the breakdown process can be obtained from the slope of $\ln(t_{bd})$ vs. $1/T_{bd}$ for any given ξ_{ox} value. Arrhenius plot for some select values of electric field, ξ_{ox}, is shown in figure 6.10a, and the extracted E_{eff} as a function of ξ_{ox} is shown in figure 6.10b. E_{eff} displays a strong dependence on the electric field. The value of E_{eff} is $\approx$ 0.7 eV at $\xi_{ox} \approx$ 2.3 MV/cm and it decreases to almost zero by the time the electric field reaches a value of 3.8 MV/cm.

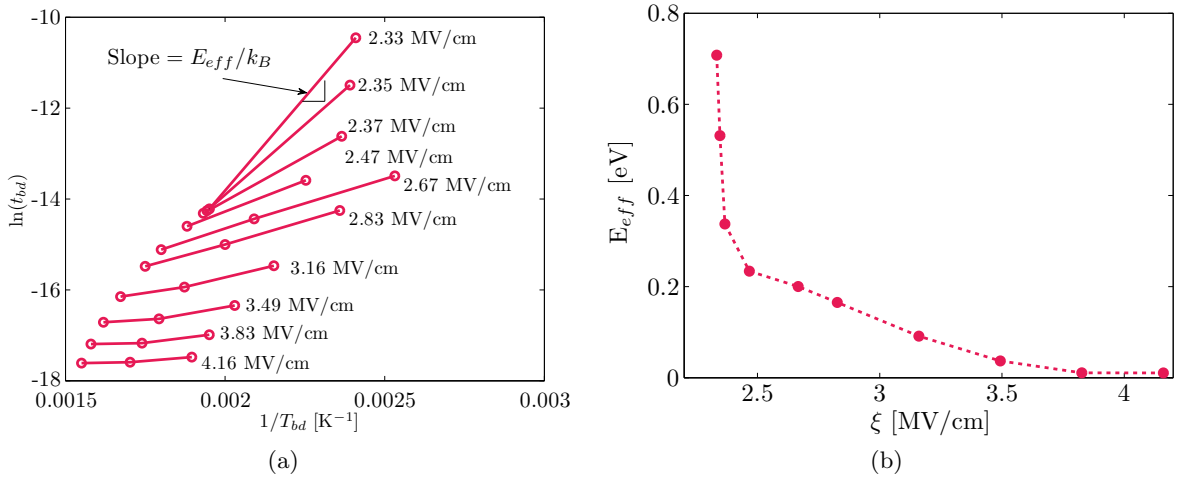

Figure 6.10: (a) Arrhenius plot for some select values of electric fields; (b) Activation energy (calculated from the slope of Arrhenius plot) as function of electric field.

Vacancy Migration Model

The vacancy migration model was discussed in detail in chapter 4. The model showed that the vacancy velocity is proportional to the applied electric field according to the following relationship.

$$\text{Velocity } \propto exp\left(-\frac{E_a}{k_B T_{bd}}\right) sinh\left(\frac{\xi_{ox} q\alpha}{2k_B T_{bd}}\right) \tag{6.7}$$

In equation 6.7, all the variables retain their original definition as presented in chapter 4. When $(\xi q\alpha)/(2k_B T) \gtrapprox 1$, as is the case for all of the data in figure 6.9b, the *sinh* term in equation 6.7 can be replaced with an exponential term as shown in equation 6.8 below.

$$\text{Velocity } \propto exp\left(-\frac{E_a}{k_B T_{bd}}\right) exp\left(\frac{\xi_{ox} q\alpha}{2k_B T_{bd}}\right) \tag{6.8}$$

If the onset of localization event during electroforming is a result of accumulation of vacancies that generates a small portion of the conductive filament, then it is reasonable to assume that for all the pulsed electroforming cases, approximately equal number of vacancies need to migrate over the t_{bd} period of time. Under this assumption, the product of t_{bd} and vacancy velocity should be a constant (equation 6.9). As a result, t_{bd} should be exponentially proportional to the activation energy and the applied electric field as shown in equations 6.10 and 6.11. Comparing equations 6.11 and 6.6 revels that E_{eff} should decrease linearly with ξ_{ox} as shown in equation 6.12.

$$\text{Velocity} \cdot t_{bd} = \text{Constant} \tag{6.9}$$

$$t_{bd} \propto exp\left(\frac{E_a}{k_B T_{bd}}\right) exp\left(-\frac{\xi_{ox} q\alpha}{2k_B T_{bd}}\right) \tag{6.10}$$

$$t_{bd} \propto exp\left(\frac{2E_a - \xi_{ox} q\alpha}{2k_B T_{bd}}\right) \tag{6.11}$$

$$E_{eff} = E_a - \frac{1}{2}\xi_{ox} q\alpha \tag{6.12}$$

This functional from of E_{eff} dependence on ξ_{ox} is not in agreement with the experimental data shown in figure 6.10b. Therefore, vacancy migration model does not seem to be a good explanation

for the initiation of the breakdown event.

Besides the poor fit, the vacancy migration model has additional difficulty in explaining why the transient I-V characteristics of the devices deviate from the Joule heating model for pulses preceding the electroforming pulse. If the deviation is the sign of formation of small portion of a conductive filament, then this deviation should be present from the very beginning of all subsequent pulses as well. However, that was demonstrated not to be the case. It is as if whichever portion of the filament formed during this early localization period completely disappeared when the pulse was removed and no traces of it was left during the subsequent pulses. This should not happen if accumulation of vacancies give rise to growth of filaments which are stable kinetically. This is a phenomenon that cannot be properly explained using the vacancy migration model.

Thermo-chemical Model

The thermo-chemical model, proposed by McPherson and Baglee [116] is based on free energy consideration associated with the oxide breakdown process. This model has been successfully used to explain TDDB data for many different oxide breakdown experiments [114, 113]. According to this model, the oxide breakdown time can be expressed as shown in equation 6.13 below.

$$t_{bd} \propto exp\left(\frac{E_a}{k_B T_{bd}}\right) exp\left(-\gamma(T)\xi_{ox}\right) \tag{6.13}$$

Where,

$$\gamma(T) = B + \frac{C}{T_{bd}} \tag{6.14}$$

In equation 6.13, E_a is the activation energy, and $\gamma(T)$ is known as the temperature dependent field acceleration parameter. Due to linear dependence of $\ln(t_{bd})$ vs. ξ_{ox}, this model is often called the 'E' model. The general form of $\gamma(T)$ is shown in equation 6.14 where both B and C are constants. Equation 6.15 obtained by substituting equation 6.14 into 6.13 shows that E_{eff} has linear dependence on ξ_{ox}(equation 6.16).

$$t_{bd} \propto exp\left(\frac{E_a}{k_B T_{bd}} - \frac{C\xi_{ox}}{T_{bd}}\right) exp\left(-B\xi_{ox}\right) \tag{6.15}$$

$$E_{eff} = E_a - Ck_B\xi_{ox} \tag{6.16}$$

The functional form of t_{bd} in thermo-chemical model is very similar to the vacancy migration model, and as a result the predicted dependence of E_{eff} on ξ_{ox} is also very similar. The linear dependence predicted by both of these models fail to properly explain the experimental observations.

Like the vacancy migration model, this model also has the same problem in explaining the repeatability of pre-electroforming pulses without any observed cumulative effect. If the deviation from the Joule heating model is a sign of breaking bonds in the oxide layer (which allows the oxide to be at a lower energy state in the presence of an applied electric field), then it is not clear how such permanent damage to the oxide lattice can have no observable carry-over effect on the I-V characteristics from pulse to pulse during repeated pulsing experiments.

Hole Injection Model

The hole injection model [117, 118, 119] asserts that positive charge buildup due to hole trapping leads to localized electric field enhancement that results in oxide breakdown. The process is schematically shown for the Pt/TiO_2/Pt device in figure 6.11. Electrons injected from the cathode (bottom electrode, electrically grounded), through Fowler-Nordheim tunneling or other methods, reach the anode due to gradient in potential profile. The mismatch at the anode (top electrode, positivity biased) between the energy level of the TiO_2 conduction band and Pt fermi level means that these electrons must thermalize, that is, lose the excess energy. One such method of losing this excess energy is through impact ionization which may generate hot-holes, shown schematically in figure 6.11a. Most of these holes drift to the cathode, however a small fraction of them may get trapped in the bandgap near the cathode. Generation of these trapped holes is proportional to

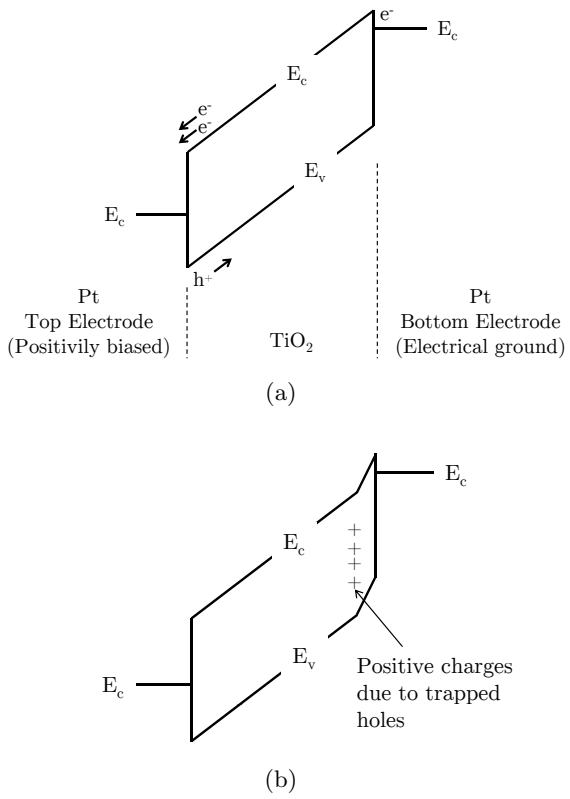

Figure 6.11: (a) Thermalization of hot-electrons and generation of hot-holes; (b) Trapped holes near the cathode.

the hot-hole generation rate, which is proportional to the electron current flow. The trapped holes create localized high electric field (figure 6.11b), which in turn locally enhances the current flow, creating a positive feedback. If this process is allow to continue, it can lead to bond breakage due to high electric field and/or the associated high temperature due to localized Joule heating, thus creating permanent damage to the oxide. However, if this process is stopped abruptly before it goes into runaway, the trapped holes may be removed through recombination [117], and no permanent damage to the oxide may occur.

The function form of t_{bd} according to this model [112] is given equation 6.17. Because $\ln(t_{bd})$ depends on $1/\xi_{ox}$, this model is often called the '1/E' model. Here, $G(T_{bd})$ is the temperature dependent field acceleration parameters and E_b is the activation energy associated with hole injection and trapping. The function form of temperature dependence of $G(T_{bd})$ is shown in equation 6.18,

where both C and E_a are constants [120].

$$t_{bd} \propto exp\left(\frac{G(T_{bd})}{\xi_{ox}}\right) exp\left(\frac{E_b}{k_B}\left(\frac{1}{300K} - \frac{1}{T_{bd}}\right)\right) \tag{6.17}$$

$$G(T_{bd}) = C + \frac{E_a}{k_B T_{bd}} \tag{6.18}$$

Substituting equation 6.18 into equation 6.17, and discarding any constant terms produces equation 6.19. The effective activation energy according to this model is inversely proportional to the electric field as shown in equation 6.20

$$t_{bd} \propto exp\left(\frac{C}{\xi_{ox}}\right) exp\left(\frac{E_a/\xi_{ox} - E_b}{k_B T_{bd}}\right) \tag{6.19}$$

$$E_{eff} = \frac{E_a}{\xi_{ox}} - E_b \tag{6.20}$$

The inverse dependence of E_{eff} on ξ_{ox} is close to the relationship observed in figure 6.10b. Although, this is not an exact match, functionally it is closer than the predictions of the other two breakdown models. The experimentally observed activation energy decreases more severely with increasing electric field compared to the predictions of this model.

The hole-injection model can also provide a qualitative explanation of the observation that pulses preceding the electroforming pulse do not show any cumulative effect. As trapped holes accumulate near the cathode in localized areas, the current through the device increases beyond what is predicted by the Joule heating model. This current is due to localized enhancement of the electric field. As large current starts to flow through a region, localized Joule heating may further reduce the TiO_2 resistivity leading to even higher current. Once the applied bias is removed, this process stops and the trapped holes may get annihilated through recombination. If all trapped positive charges are removed prior to the subsequent voltage pulse, the device would not display any cumulative effect. The only exception to the situation would be if the time gap between subsequent pulses was smaller than the thermal time constant of the device. Under this circumstance, the

device would exhibit cumulative behavior simply because it would still remain hot from the prior pulse. Since conductivity of the device is dependent on the temperature and the hole trapping rate is proportional to the total current flow, this would lead to onset of localization faster (as was observed in the pulse-train experiments).

This hole trapping based explanation does not necessarily rule out motion of oxygen vacancies. It is possible that when electric field is sufficiently enhanced in a localized region and the temperature in that region is high enough, vacancy motion participates in the breakdown process. Vacancies in that situation can either move in response to the electric field in the direction of the field or move in a lateral direction due to lateral temperature gradient [121]. The very fast decrease of activation energy as a function of electric field may result from such combined effects.

6.6 Conclusion

In this chapter, a method for extracting temperature rise at the onset of electroforming has been presented. The temperature, time, and electric field have been used to evaluate several models of oxide breakdown. Both the oxygen vacancy migration based model and the thermo-chemical model predict a linear relationship between activation energy associated with breakdown and electric field. However, the experimental observations show a strong non-linear dependence. The hole-injection model predicts an inversely proportional relationship which is close to the experimental observations. The hole-injection model is also able to explain the non cumulative effect observed when a pristine device is subjected to multiple pulses prior to electroforming. Based on these observations, it is concluded that the onset of electroforming is not triggered by ion migration, rather it is an electronic process. However, it is possible that vacancy migration still participates in the electroforming process once the local electric field and temperature increases significantly.

Chapter 7

Morphological Changes And Estimation Of Filament Size

Morphological changes are often associated with electroforming and resistive switching operations in RRAM devices. These observations have been linked to localized dissipation of high power resulting from filamentary electrical conduction mechanisms. The pulsed induced electroforming experiments discussed in chapter 5 also exhibited similar types of morphological changes after the completion of the electroforming event. In discussing the electrical and thermal transients during electroforming, the focus of the previous chapter was on uniform Joule heating during the early portion of the electroforming pulse. It was observed that a uniform Joule heating model could no longer explain the current and voltage transients of the device after a certain period of time, denoted as $t_{uniform}$. The argument was made that after this time, the current conduction starts to localize and eventually leads to formation of filaments. In this chapter, the link between this localized electrical conduction and associated localized morphological changes will be examined. The first section will focus on the relationship between electroforming conditions (voltage, power, time, etc.) and the physical extent of the morphological changes observed after the completion of electroforming. In the second section, an estimate of the filament size will be obtained using experiments designed to isolate the conductive portion of the device. The discussion in the third section will be about how these morphological changes evolve during various phases of the electroforming process. Finally in the

fourth section, electro-thermal simulations will be used to correlate the observed morphological changes with various filament geometries.

7.1 Effect Of Electroforming Conditions On Morphological Changes

The relationship between electroforming time and voltage was explored in chapter 5. It was observed that as the voltage was reduced, the electroforming time increased significantly. As a consequence of this voltage-time relationship, devices with short electroforming pulses experienced higher power dissipation level compared to the ones with long pulses. Figure 7.1 shows SEM images of several devices electroformed with voltage pulses with widths ranging from 20 ns to 10 μs.

It is clear that the extent and the nature of the morphological changes observed after electroforming is heavily dependent on the amplitude and the width of the electroforming pulses. The extent of the affected area generally gets bigger with increasing pulse width. For the short pulses (e.g. 20 ns, 50 ns, 100 ns), there is always an area where the Pt top electrode seem to have been melted and completely removed. For convenience of discussion, this type of features will be referred to as the 'blown-off region'. For longer pulses, the extent of this blown-off region begins to get smaller and it starts to get surrounded by a region that has brighter contrast in SEM image compared to the remainder of the device. Close examination reveal that this area consist of large Pt grains, which may have formed as a result of elevated temperature due to large power dissipation after electroforming. Once again, for convenience of discussion, this type of area will be referred to as the 'halo'. The images show that as the electroforming voltage decreases (and the pulse width increases), the morphological changes smoothly transition from exhibiting large blown-off region with no halo to almost non-existent blown-off region with halo that encompasses a very large portion of the device area. Larger version of each image in figure 7.1 can be found in Appendix B.

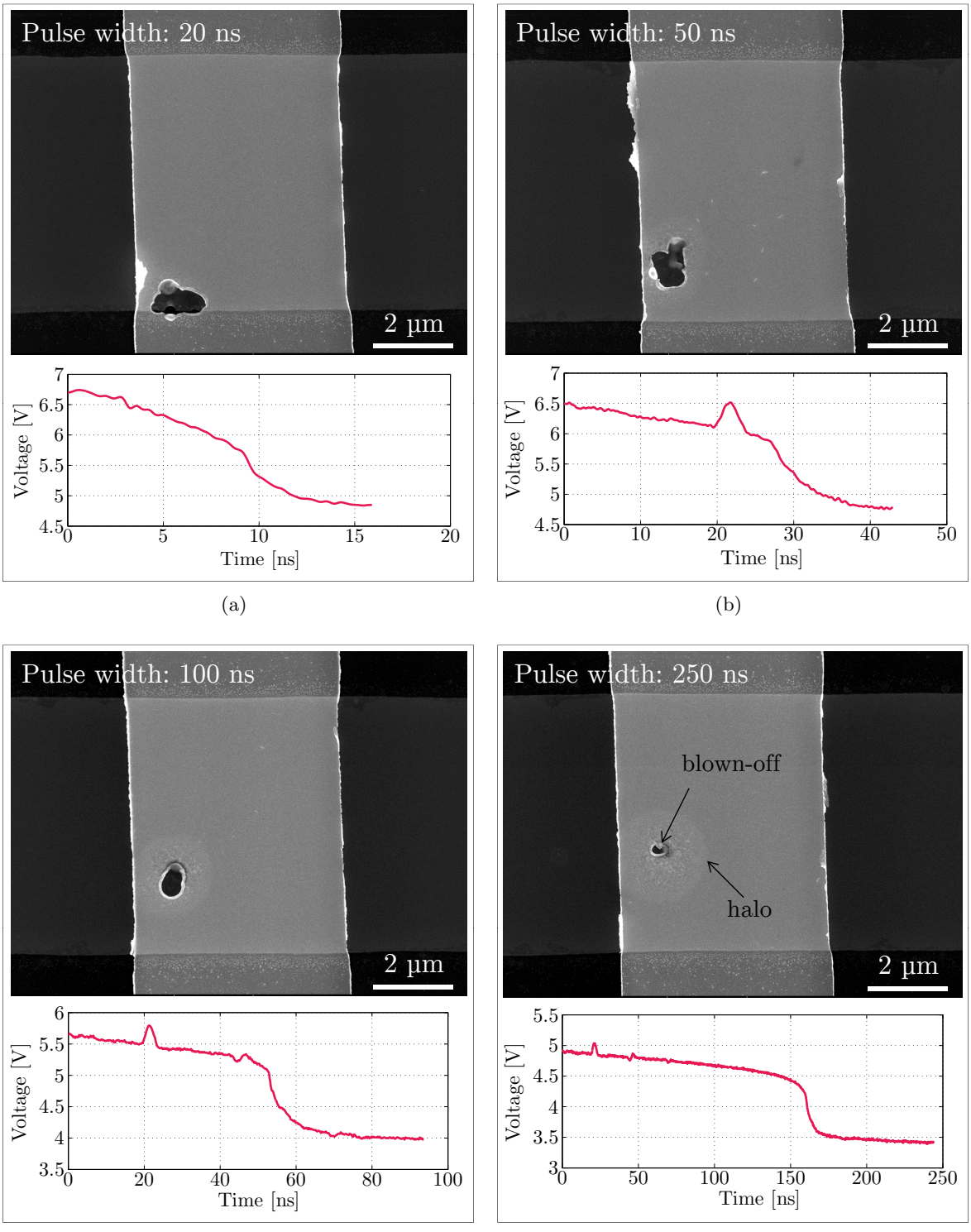
Pulse width: 20 ns
2 µm
Voltage [V]
Time [ns]
(a)
Pulse width: 50 ns
2 µm
Voltage [V]
Time [ns]
(b)
Pulse width: 100 ns
2 µm
Voltage [V]
Time [ns]
(c)
Pulse width: 250 ns
blown-off
halo
2 µm
Voltage [V]
Time [ns]
(d)

Figure 7.1

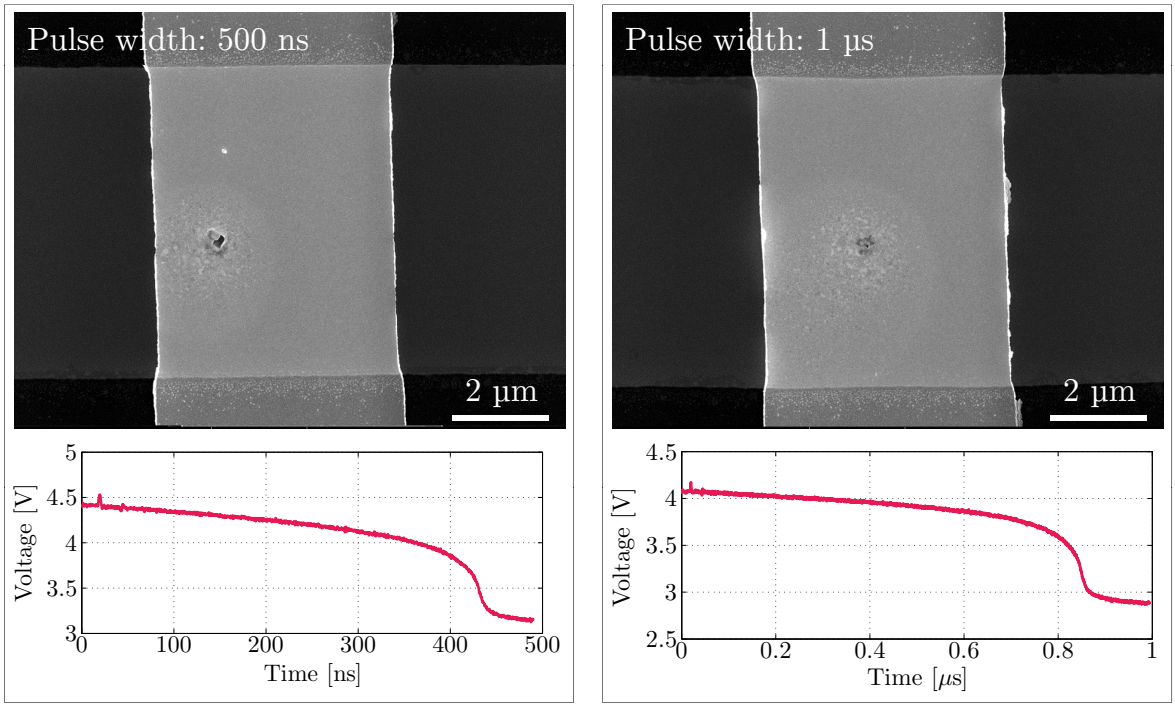

(e) (f)

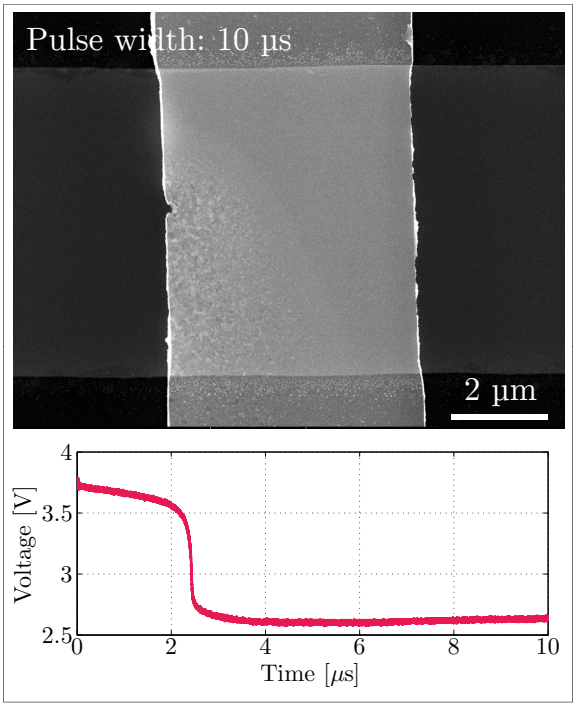

(g)

Figure 7.1: SEM images of morphological changes resulting from electroforming with voltage pulses with widths of 20 ns, 50 ns, 100 ns, 250 ns, 500 ns, 1 µs, and 10 µs in figure (a)-(g), respectively. All experiments were carried out under ambient temperature of 62.5 °C. The vertical metal trace in each image is the top electrode. Each image is accompanied by the associated voltage pulse.

As discussed in chapter 5, the resistance of the devices after electroforming ranged from 120-220 Ω, with smaller resistance values corresponding to cases where electroforming voltage amplitude was large. The blown-off regions and the halos give an indication of the areas that were affected by localized heating. Based on this, it is safe to assume that the filament(s) that gives rise to the low resistance value is located somewhere within these regions. However, it is difficult to estimate the filament size based on these images alone. Considering the short pulse cases (e.g. 20 ns, 50 ns), it is not clear what size of filament caused a blown-off region that has ≈ 1 μm diameter. It is possible that the size of the filament is either the same as the size of the blown-off region, or the large blown-off region is a result of lateral heat conduction due to a very small filament that gets very hot. The case with the largest halo (e.g. 10 μs pulse) is even more puzzling. Here the halo does not seem to originate from any one spot and radially expand outward, as would be expected if it was generated from a central hot zone caused by a low resistance filament. Rather it is asymmetric in shape, possibly indicating a more distributed nature of the low resistance region.

It is possible that the underlying nature of physical changes in the TiO_2 film for both long and short pulses are very similar. The presence or absence of the blown-off region may be explained by considering the power dissipation level associated with each case. Similarly, size of the halos may be correlated with the pulse widths, since the grain growth in films is a function of both temperature and time [122]. In order to justify any of these arguments, more information is needed about the size of the filaments, and this is the topic of the next section.

7.2 Estimation Of Filament Size

To get a better estimate of the filament size, an electroformed device was cut into several pieces in order to identify the portion of the device responsible for the low resistance. The cutting was performed using a gallium Focused Ion Beam (FIB). The resistance of the device was measured

before and after each cut (at 1 V). Figure 7.2 shows the SEM images of the device after each cut. This particular device was electroformed using a voltage pulse with 4.4 V amplitude and the resistance immediately after electroforming was found to be 160 Ω. Each successive cut isolated specific portion of the device that seemed to have been affected by electroforming (based on the appearance of the morphological changes). Each cut was ensured to be deep enough to go through the entire top-electrode/TiO_2/bottom-electrode stack.

The images in figure 7.2 show the measured resistance after each of the associated cuts. The resistance of the area isolated during each cut (also noted on each image, indicated by arrow) is estimated based on parallel resistor assumption. Since the resistance before, R_{before}, and after, R_{after}, each cut is measured, the resistance of the isolated area, $R_{isolated}$, can be calculated using equation 7.1.

$$R_{isolated} = \left(\frac{1}{R_{before}} - \frac{1}{R_{after}} \right)^{-1} \tag{7.1}$$

From these calculated values, it seems that the initial 160 Ω resistance value was not due to any small isolated low resistance region within the device. Rather, electroforming process reduced the resistance over a large area, and the combined contribution of each portion of this area resulted in the observed low resistance value after electroforming.

At this point, it is instructive to compare the resistivity of the device in various regions based on these measurements. Prior to electroforming, the pristine device was found to have a resistance of ≈ 2 MΩ at 1 V. This equates to a resistivity of ≈ 4000 Ω·m. After all the cuts, in total, roughly about 1/4 of the device area was removed and the resistance of the remainder of the device was ≈ 25 kΩ. If this area had uniform resistivity, it would equate to ≈ 37.5 Ω·m. The area with the lowest resistance was the one shown in figure 7.2h. The resistance was 614 Ω with an area of approximately 1 μm^2. The gives a resistivity of 0.409 Ω·m. It is possible that far way from the regions affected by morphological changes, the resistivity of the TiO_2 film is unchanged from its

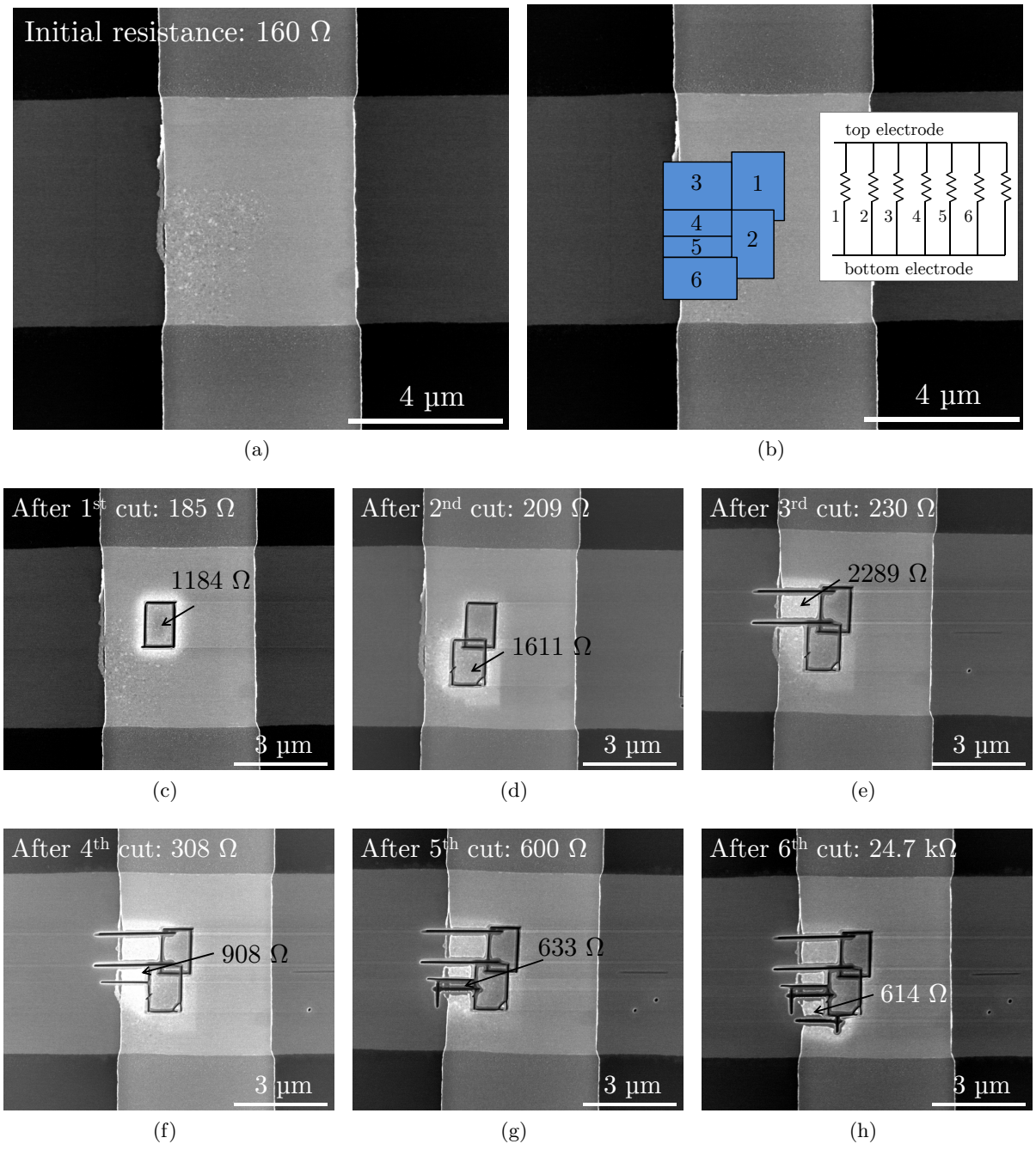

Figure 7.2: (a) SEM image of the device after electroforming with a voltage pulse of 4.4 V amplitude; (b) Schematic of FIB cuts. Each area isolated by the cuts is highlighted. Each of these areas is represented by a resistor connected in parallel with the other areas (inset); (c)-(h) shows SEM images of cuts made using FIB for each area highlighted in (b). Measured resistance after each cut is noted at the top of each picture. The calculated resistance of the isolated region (using equation 7.1) in each case is indicated using the arrow. The vertical and horizontal metal traces in each image are the top and bottom electrodes, respectively.

pristine value. If this is indeed the case, then it would imply that the resistivity changes by almost 5 orders of magnitude between the high and low resistivity areas. Figure 7.2 shows that moving away from the area with the lowest resistance does not result in drastic increase in film resistivity. Therefore this 5 orders of magnitude resistivity change is mostly likely to be gradual in nature rather than abrupt. It is unlikely that a hard boundary can be located between 'filamentary' and 'non-filamentary' regions.

7.3 Evolution Of Morphological Changes

The examples of morphological changes showed what the devices look like after they have experienced the electroforming pulses in their entirety. However, how these changes evolve during the course of the pulse was not captured. Visually observing these changes as a function of time is not possible due to the speed with which the resistance change occurs. The evolution of these morphological changes could be observed if the voltage pulse could be removed arbitrarily at any point during the resistance change process. However, this is a very difficult task. Although the time scale of the electroforming event can be predicted based on prior experiments, the exact time when the resistance change will be initiated during the pulse is still not deterministic in nature. When the pulse amplitude is small, the time over which the resistance change takes place is relatively long (e.g. the 10 μs case shown in figure 7.1g). For this type of cases, there is a better chance of being able to stop the pulse partially into the electroforming process. An experiment was designed where each device was subjected to a series of voltage pulses with the same amplitude where the pulse width was incrementally increased. Once a resistance decrease similar to electroforming was observed, the devices were no longer subjected to any further voltage pulses. This procedure, carried out over a large set of devices, yielded conditions where the electroforming process was halted at various stages of completion on different devices. SEM images of these devices along with the

corresponding pulses are shown in figure 7.3.

In the previous chapter, it was observed that the drastic voltage drop associated with electroforming was not explainable with uniform Joule heating model. The experimental results in figure 7.3 show that as the voltage starts to decrease rapidly, the electric conduction through the device begins to localize as indicated by the appearance of the halos. For the cases where electroforming process was halted early (e.g. cases 1-3), the halos are circular and quite symmetric. However, this symmetry begins to disappear as the process is allowed to continue for longer (e.g. cases 5 and 6). This indicates that the appearance of one locally conductive region does not necessary prevent other nearby regions from going through similar transitions. Therefore, the actual affected area could be quite large, consistent with the results from the FIB experiment in the previous section.

Morphological changes to the top electrode is function of both the power and time, and therefore not all affected areas of the underlying TiO_2 film necessarily exhibit corresponding morphological changes on the top electrode. This is specially significant for the cases were the electroforming pulse widths are short (e.g. 20 and 50 ns cases in figure 7.1). For those cases, only the areas with the lowest resistivity may show any sign of change (the blown-off regions) where enough power was dissipated over the short period of time. The surrounding areas may look to be unaffected judging simply by the morphology of the top electrode. However, the TiO_2 layer in these regions may also have gone through large changes (just not as much as the blown off regions) compared to their pristine state. As a result, the regions responsible for resistive switching does not necessarily have to correspond to the region which first exhibits morphological changes. In fact, this was observed when resistance switching experiments using DC voltage sweeps were performed on these pulsed electroformed devices. An example of this is shown in figure 7.4. Here, a device was electroformed with a 50 ns wide pulse, similar to the one in figure 7.1b. Then several cycles of switching were performed using DC voltage sweeps. The SEM image immediately after electroforming shows no

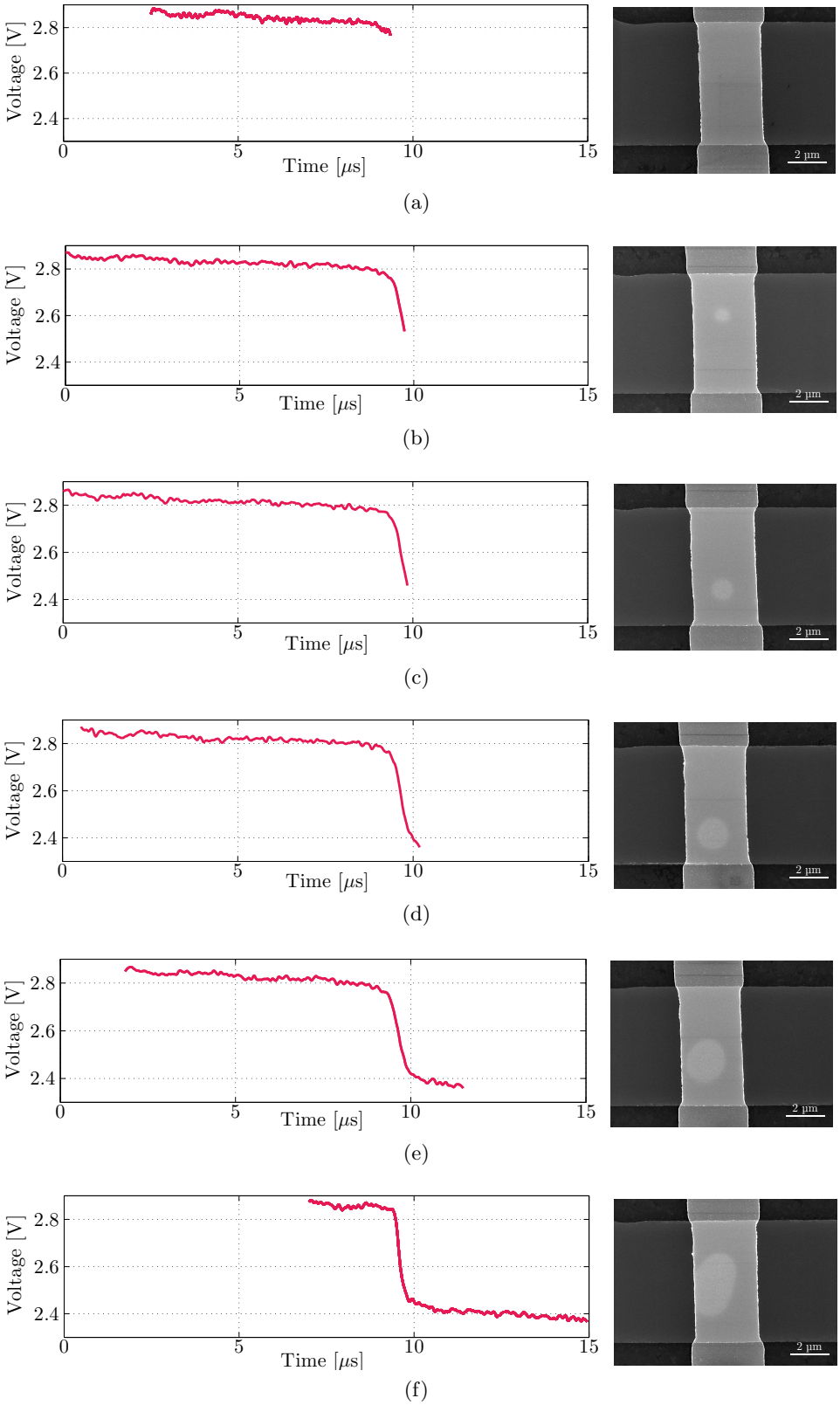

Figure 7.3: SEM images of six different devices where the voltage pulses were abruptly stopped during various stages of completion of the electroforming process. The pulses were shifted along the horizontal axis in order to align the transition periods. The vertical and horizontal metal traces in each image is the top and bottom electrodes, respectively.

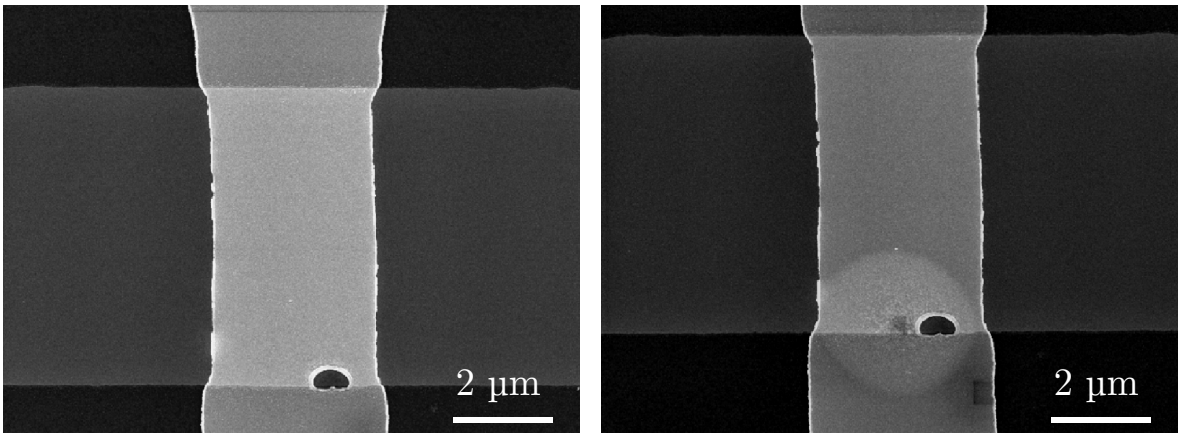

(a) (b)

Figure 7.4: (a) SEM image of a device immediately after electroforming with a voltage pulse with 50 ns width; (b) image of the same device after performing several cycles of switching with DC voltage sweeps.

observable halo near the blown-off area. However, the image after the switching cycles shows large circular shaped halo with a center that is away from the original blown-off region. It appears that the main power dissipation during resistance cycling took place near the center of the halo. Clearly, sufficient changes were induced in the TiO_2 film during the electroforming process in this region that made resistance switching possible during DC sweeps. There changes were not directly reflected in morphological changes observed immediately after electroforming.

7.4 Filament Geometry And Thermal Profile

After electroforming, the resistance of the devices were generally found to be in the range of 120-220 Ω based on various electroforming conditions. Experiments and the results described in the previous two sections suggest that this resistance is a consequence of lowered resistivity of the TiO_2 film over a relatively large area. In this section, an electro-thermal model will be discussed that will be used to determine if the correlation between electroforming conditions and the morphological changes can be supported by the thermal profiles predicted by the model.

Electro-thermal Model

A thermal model for the device was introduced in chapter 5 and it was used in chapter 6 to estimate the temperature rise due to uniform Joule heating. In this chapter, the same model will be used again. However, rather than a just a thermal model, where the power dissipation level is specified as a function of time, an additional DC electrical conduction module is incorporated in order to investigate the electro-thermal interaction. The expression for heat conduction was presented in chapter 5, and is repeated here (equation 7.2) for convenience. The expression for current conduction is given in equation 7.3. Here, J is the current density, ξ is the electric field and σ is the electrical conductivity. The link between the heat and current conduction is established using equation 7.4. The power dissipation due to resistive heating serves as the heat source in the heat conduction equation.

$$Q = \rho C_p \partial T/\partial t + \nabla \cdot (-k_{th} \nabla T) \tag{7.2}$$

$$J = \sigma \xi \tag{7.3}$$

$$Q = J\xi \tag{7.4}$$

In the model, the electrical contact resistance between all the layers are assumed to be negligible. Similar assumption was made about the interface thermal resistance in the previous chapters. However, in this chapter, the effect of including a thin thermally resistive interface layer will be compared with perfect interfaces where no such interface resistance exists. Figure 7.5 schematically shows the simulated structure. It is similar to the one shown in chapter 5, but the electrical boundary conditions are explicitly indicated in this figure.

Using this model, two cases will be examined. 'Case 1' will focus on pulses with 20 ns width and 'case 2' on pulses with 10 μs width. Morphological changes corresponding to electroforming with pulses of these two widths were shown in figures 7.1a and 7.1g. For all simulations, the

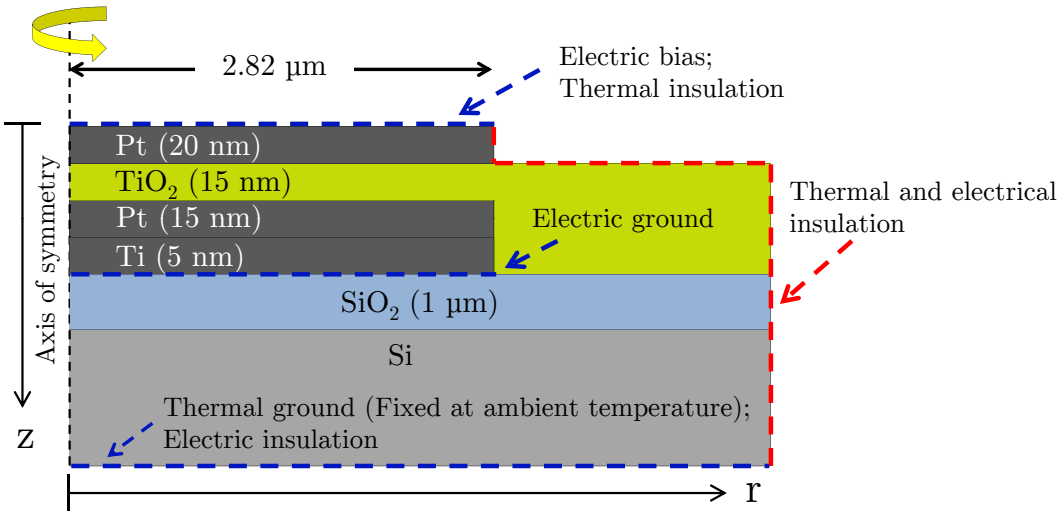

Figure 7.5: Schematic diagram of device geometry used for electro-thermal simulations.

voltage was be kept constant for the entire duration of the pulse. The voltage amplitude and the device resistance were chosen based on the values obtained at the end of the electroforming pulses shown in figures 7.1a and 7.1g. These values, along with other simulation parameters, are summarized in table 7.1. The thermal conductivity for all the materials were kept unchanged from the values given in table 5.1. Strictly speaking, it can be argued that the voltage and resistance levels are not constant during the electroforming process, and therefore these parameters should vary as a function of time to mimic the real electroforming event. However, as figure 7.3 showed, majority of the morphological changes occur after the voltage and resistance transients associated with electroforming become stable. Also, it was observed that after electroforming, subjecting the devices to additional voltage pulses (of the same width and amplitude) did not significantly alter the morphological changes. On these grounds, keeping the voltage and resistance level constant for the entire duration of the pulse seems reasonable, and it greatly simplifies the simulations.

The discussions about simulations are broken into two sections based on the assumptions made about the geometry of the filaments. In the first section it will be assumed that electroforming only affects certain localized regions, and within these regions, the resistivity of TiO_2 is uniformly

Table 7.1: Parameters for electro-thermal simulations

	Case 1	Case 2
Pulse Width	20 ns	10 μs
Voltage	4.85 V	2.63 V
Resistance after electroforming	164 Ω	220 Ω
Pristine TiO_2 resistivity	2.02 Ω·m at 4.85 V	20.9 Ω·m at 2.63 V
TiO_2 filament resistivity	See table 7.2	
Si electrical resistivity	641 Ω·m	
SiO_2 electrical resistivity	1.42×10^{12} Ω·m	
Pt electrical resistivity	1.06×10^{-7} Ω·m	
Ti electrical resistivity	4.2×10^{-7} Ω·m	
Interface thermal conductance	60 MW/m^2K	
Ambient temperature	62.5 °C	

lowered. The resistivity of the filaments will be calculated based on the measured resistance after electroforming (as listed in table 7.1) and the assumed filament size. In the second section, the assumed geometry of the area affected by electroforming will more closely mimic what has been found from the FIB experiment described in section 7.2; the change in resistivity due to electroforming will be more gradual in nature.

Simulation: Isolated Areas Of Low Resistance

For all the simulations in this section, it is assumed that a cylindrical shaped filament of certain radius is responsible for the observed low resistance after electroforming. The filament radii explored are 10 nm, 100 nm, 250nm, 500 nm, 1 μm, and 1.5 μm in size. TiO_2 resistivity in this filament region is calculated based on the post-electroformed resistance (listed in table 7.1) and the assumed radius for each case. The calculated resistivity values are given in table 7.2. Outside of this region, the resistivity of the TiO_2 film is assumed to be unchanged from its pristine value. Of course, as discussed in chapter 6, the current through the pristine device non-linearly depends on the voltage. As a result, two different resistivity values need to be used for the 20 ns and the 10 μs pulses

Table 7.2: Calculated filament resistivity used in electro-thermal simulations

Filament radius	Resistivity (Ω·m)	
	Case 1	Case 2
10 nm	3.4×10^{-6}	4.6×10^{-6}
100 nm	3.4×10^{-4}	4.6×10^{-4}
250 nm	2.1×10^{-3}	2.9×10^{-3}
500 nm	8.6×10^{-3}	1.2×10^{-2}
1 μm	3.4×10^{-2}	4.6×10^{-2}
1.5 μm	7.7×10^{-2}	1.0×10^{-1}

since the applied voltage is different for the two cases. These values are indicated as 'pristine TiO_2 resistivity' in table 7.1.

Two sample thermal profiles corresponding to filament radius of 500 nm subjected to 20 ns pulse are shown in figure 7.6. The temperature shown in this figure corresponds to the temperature at the end of the 20 ns pulse. In figure 7.6a, the interface thermal conductance between all layers is assumed to be infinitely high (therefore, no thermal boundary layer), whereas in figure 7.6b it is assumed to be 60 MW/m^2 K. The interface thermal conductance at the lateral boundary between the filament and the pristine TiO_2 region is always assumed to be infinitely high for both cases.

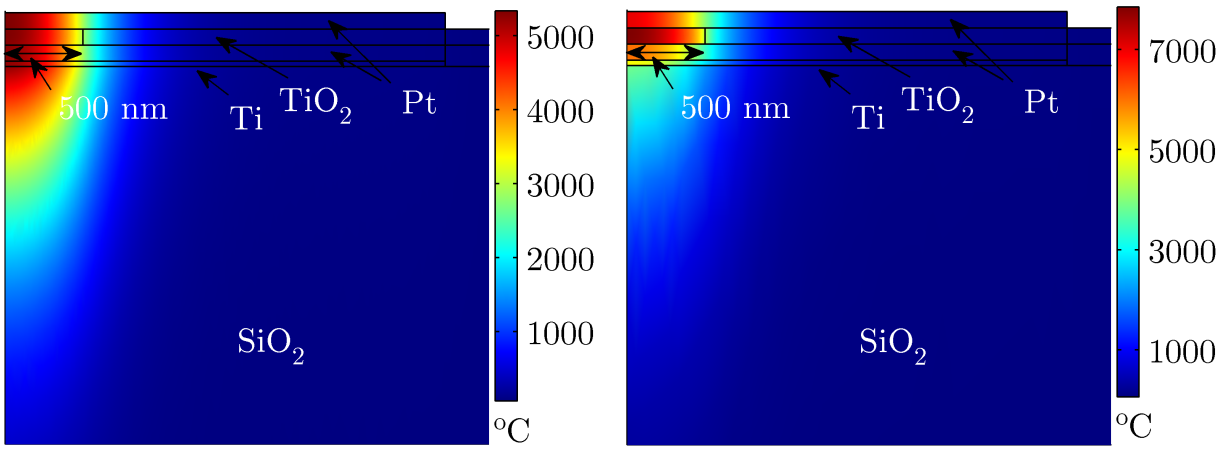

(a) (b)

Figure 7.6: Simulated thermal profiles for a filament with 500 nm radius at the end of subjecting the device to a 20 ns voltage pulse with 4.85 V amplitude. Effect of excluding and including a thermally resistive boundary layer is shown in (a) and (b), respectively.

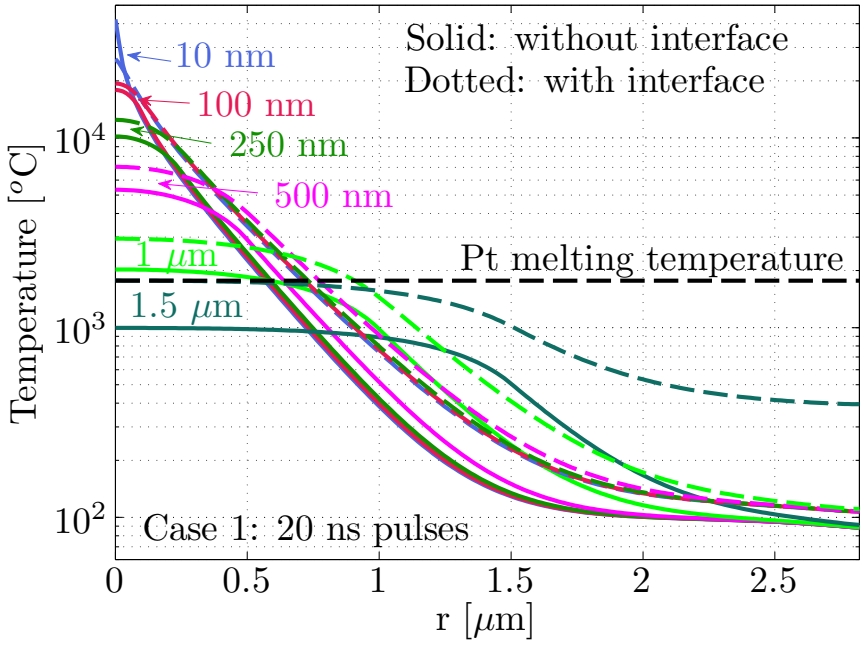

(a)

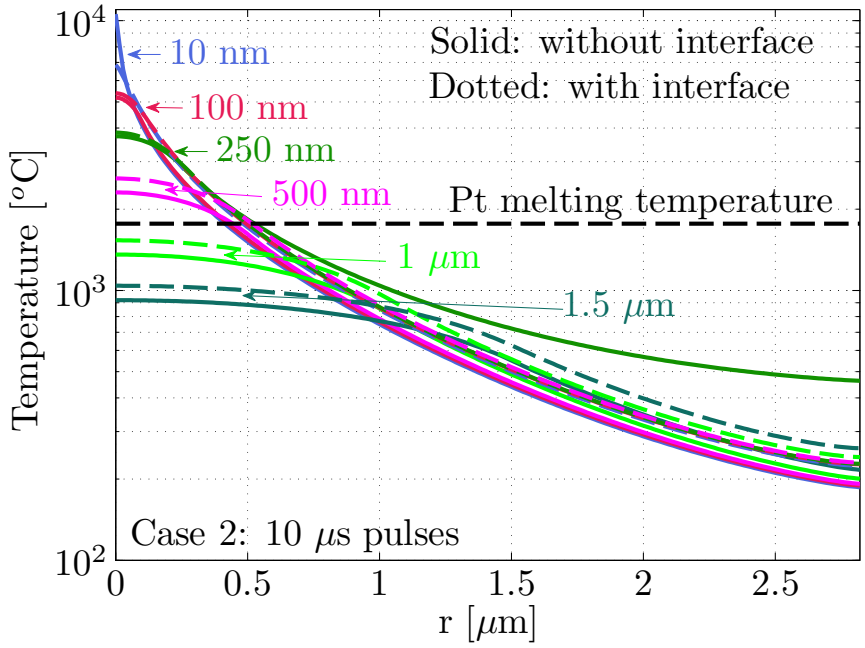

(b)

Figure 7.7: Radial cross-section of the thermal profiles of the top electrode at the end of application of a 20 ns pulse (a) and 10 µs pulse (b) for a variety of filament sizes. Effect of excluding and including a thermally resistive boundary layer is shown in solid and dotted lines respectively for each case. Vertically, this cross-section is taken 1 nm away from the TiO_2 and top electrode interface.

The presence of the thermally resistive interface layers cause the temperature of the filament region to be higher compared to the case where there are no such interface layers. This in turn leads to higher temperature at both the top and the bottom electrodes adjacent to the filament region. Figure 7.7 shows the radial cross-section of the temperature profiles at the top electrode for all the different filament sizes for both 20 ns and 10 μs pulse cases. Vertically, this cross-section is taken 1 nm away from the Pt top electrode and TiO_2 interface. In these plots, the dotted and solid lines represent the temperature with and without the thermal interface layers, respectively. The full 2-D temperature profiles for all these cases can be found in appendix A. For the 20 ns pulse cases (figure 7.7a), the temperatures toward the center either exceeds or comes very close to the melting temperature of Pt for all the filament sizes. The only exception is when the filament radius is 1.5 μm with no thermal interface layers. This means any of these cases can explain the blown-off region that was observed as a result of performing electroforming with 20 ns pulses (figure 7.1a), assuming those regions resulted from melted Pt. For the very small filament sizes (e.g. 10 nm, 100nm, and 250 nm) the temperatures predicated by the simulation are unphysically large. Nonetheless, it is safe to assume that given the power density, the temperature of the top electrode would exceed the melting temperature of Pt, even if it does not actually reach the many thousand degrees predicted by the simulation. In contrast to electroforming with 20 ns pulses, devices electroformed with 10 μs pulses did not exhibit any blown-off regions (figure 7.1g). Which means, for the 10 μs pulses, the temperature of the top electrodes most likely did not exceed the melting temperature of Pt. This suggests that the filament size could not have been any smaller than 1 μm in radius, since the simulation results (figure 7.7b) predict temperatures higher than Pt melting point for those cases. For large filament sizes (with radius of 1 μm and above), the temperature still reaches 1000 °C or higher in some cases. Given the longer time scale of the pulse and this temperature range, it is conceivable that Pt grains, responsible for the halos, form as a result of these conditions.

None of the simulated conditions satisfactorily explain the thermal behavior that can be correlated with the images in figure 7.1. On the one hand the filament size needs to be large so that the temperature does not reach too high for the 10μs pulses. Only large filaments can ensure that the power density stays low enough so that the melting temperature of Pt is not reached. On the other hand, large filaments give rise to thermal profiles that are generally more uniform. This leads to a situation where the predicted blown-off region (based on the area over which Pt melting temperature is exceeded), caused by 20 ns pulses, becomes too large. For example, both 1 μm and 1.5 μm filament radius assumption leads to condition where Pt would melt over an area with a radius of ≈1 μm. However, experimental results of electroforming with 20 ns pulses only display blown-off regions with a radius of ≈0.5 μm. The assumptions that resistance change induced by electroforming is uniform over a certain isolated region and the size of this region is the same for both 20 ns and 10 μs electroforming pulses, do not lead to any viable thermal profiles that can explain the observations of morphological changes.

Simulation: Distributed Areas Of Low Resistance

The experiment in section 7.2 showed that the geometry of the area affected by electroforming is wide spread and the TiO_2 resistivity varies gradually within this region. Simulations in this section examines the case where the resistivity of TiO_2 more closely mimics this situation. Instead of assuming a certain filament size as was done for the previous simulations, the modeled device is broken up into three regions of low, intermediate, and high resistivity. The resistivity of these three regions are shown in figure 7.8. The low resistivity region is the one closest to the axis of symmetry in the model. The resistivity here is based on figure 7.2h, where an ≈1 μm^2 area was found to had a resistance of 614 Ω, and it was the most conductive portion of the entire device. In the model, this corresponds to a resistivity of 4×10^{-2} Ω·m over a region with a radius of ≈ 564 nm. The high

resistivity region of the device is the outermost portion with r > 1.5 μm. Here the resistivity is set to the value that matches the pristine TiO_2 film. This is based on the assumption that far away from the regions affected by electroforming, properties of TiO_2 does not change. The intermediate resistivity region lies in between these two areas. Here the resistivity is calculated such that the total resistance of the device matches the measure resistance after electroforming, as listed in table 7.1.

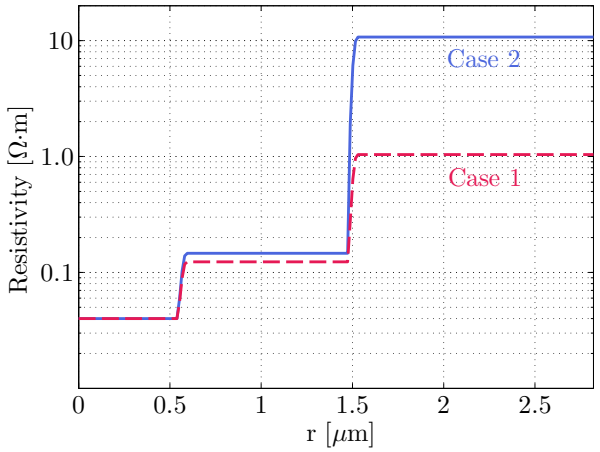

Figure 7.8: Resistivity of the TiO_2 layer used for simulation under the distribued filament model. Case 1 and case 2 corresponds to 20 ns and 10 μs pulse cases respectively as listed in table 7.1.

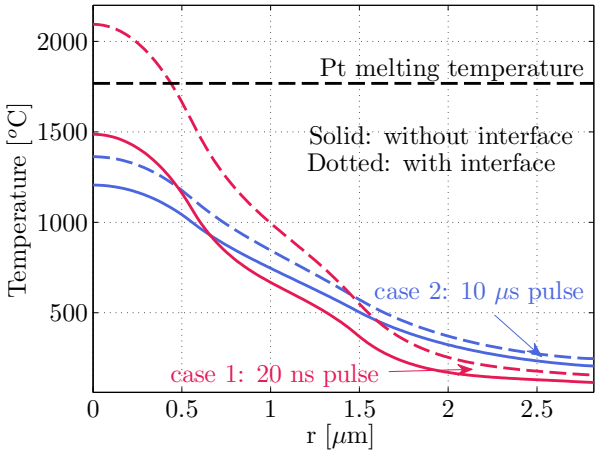

Figure 7.9: Radial cross-section of the thermal profiles of the top electrode at the end of application of 20 ns and 10 μs pulses. Effect of excluding and including thermally resistive boundary layers are shown in solid and dotted lines respectively for each case. Vertically, this cross-section is taken 1 nm away from the TiO_2 and top electrode interface.

Figure 7.9 shows the simulated temperature profiles across the top electrode for both 20 ns and 10 μs pulse cases. Vertically, this cross section is taken 1 nm away from the top electrode and TiO_2 interface. For both cases, the temperature at the electrode is higher when the thermally resistive interface layers are taken into account. Under this condition, the simulation predicts that for the 20 ns pulse case, the temperature will be higher than the Pt melting point in a region that has a radius of approximately 0.5 μm. This is consistent with the size of the blown-off region observed (figure 7.1a) on devices electroformed with 20 ns pulses. For the 10 μs pulse case, the peak temperature is approximately 1350 °C and decrease gradually away from the center of the device. This temperature profile most likely will not produce any blown-off region since the highest temperature is several hundred degrees lower than the Pt melting temperature. However, grain growth due to high temperature and longer timescale under these conditions is still possible. This again is consistent with the experimental observation of large halos seen in figure 7.1g. Dividing the device into three regions of incrementally increasing resistivity is a crude method of approximating the gradual change in resistivity caused by electroforming. However, even with these crude approximations, morphological changes can be explained more consistently compared to the method of the previous section.

7.5 Conclusion

In this chapter, a correlation between various electroforming conditions and the associated morphological changes have been established. It has been found that the nature of morphological changes vary drastically depending on the electroforming conditions. Electroforming pulses with short width and high amplitude (e.g. 20-50 ns and 4-5 V) causes localized blown-off regions on the top electrode that most likely results from molten Pt due to excessive power dissipation. These blown-off regions gradually disappear as the electroforming pulse widths get longer and the amplitude get smaller

(e.g. 500ns-10 μs and 2.5-3.5 V). For the very long pulses, grain growth is observed over large areas of the top Pt electrode. By cutting an electroformed device into several pieces, it was found that the physical extent of the affected region can be quite large in size ($\approx$ 8-9 μm^2), and within this region the resistivity changes gradually over 2-3 orders of magnitude. Electro-thermal simulations show that this gradual resistance change model is able to adequately reproduce thermal profiles that support the different types of morphological changes observed under various types of pulses.

Chapter 8

Conclusion

Migration of oxygen vacancy is believed to be the key mechanism behind resistance switching in TiO_2 based ReRAM devices. Literature review shows that resistance switching is generally a localized event dominated by filaments of more conductive phases of TiO_2. The initial formation of these filaments during the electroforming process and the subsequent modification of their size/shape during repeatable resistance switching is postulated to be a direct result of change in oxygen vacancy concentration in response to applied electric field and related temperature rise.

Often in literature, an exponential dependence of vacancy migration velocity on electric field is invoked in order to explain how both fast switching and long retention time can be obtained just using the vacancy migration mechanism alone. In chapter 4, a model was developed for migration of vacancies to investigate this claim in detail. This model was then implemented in a 1-D device based on parameters of $SrTiO_3$ as the resistance switching oxide. The simulation results showed that no reasonable combination of electric field, temperature, and activation energy can lead to conditions where both 100 ns programming time and 10 years of retention time is possible to achieve. A vacancy migration activation energy of ≈ 1 eV is found to be high enough that can lead to retention time of 10 years, but in order to move sufficient vacancies such that the device can be programmed in 100 ns, an electric field on the order of 10 MV/cm with temperature greater than 2200 °C is needed. The required temperature can be dropped to less than 1000 °C if the electric

field is allowed to be close to 100 MV/cm. This is an enormously large field, translating to over 100 V applied to the device when the oxide thickness is in the range of 10-50 nm. It is often argued that such large electric fields can indeed be achieved during resistive switching using small applied biases because of the existence of conductive filaments which effectively reduce the gap over which the voltage drop occurs. However, how such large electric field can lead to repeatable resistance switching without causing permanent damage to the oxide layer remains a mystery. The simulation results seriously calls into question the vacancy migration model used to explain resistive switching.

The origin of conductive filaments, responsible for resistance switching, is linked to the electroforming process. It was demonstrated that electroforming with DC voltage sweep is inherently a very poorly controlled method that leads to large current overshoot through the device. The magnitude of this overshoot is only limited by the device resistance despite the enforcement of a compliance current, and the time scale is dictated by the measurement equipment. In order to gain more insight into the electroforming process, a pulsed based method was introduced which allowed for characterization of transient voltage, current, resistance, and power dissipation of the device over the entire duration of the electroforming process. Based on these measurements, a novel method was introduced to extract the transient temperature rise during electroforming due to Joule heating. Temperatures obtained using this extraction method was correlated with results from thermal simulations. These pulsed experiments revealed that electroforming time can be changed by 6-7 orders of magnitude based on the pulse amplitude and temperature of the device. This time can be as short as 10 ns for a voltage pulse with 8 V amplitude, or as long as 100 ms for a pulse with 4 V amplitude. The temperature rise due to Joule heating can range from 25-300 °C. In the low voltage regime ($V < 4V$), the electroforming time was found to be a very strong function of temperature, where a 50 °C rise in temperature can lower the electroforming time by 3-4 orders of magnitude. Such strong dependence on temperature was not observed in the high voltage regime.

It was also observed that electroforming process is device history independent, meaning subjecting a device to multiple pulses prior to electroforming did not lead to any observable cumulative effect. The only condition where cumulative effect was observed was when time gap between multiple pulses were lowered below the thermal time constant ($\approx$ 3 μs) of the device so that heating from one pulse affected the device behavior during subsequent pulses.

Based on these observations from the transient electroforming experiments, three different models of oxide breakdown were evaluated. It was found that both oxygen vacancy migration based model and the thermo-chemical model fails to predict the non-linear relationship between the activation energy and the electric field observed during the pulsed electroforming experiments. A model based on injection and trapping of holes due to current flow through the TiO_2 layer predicted an inversely proportional relationship between the activation energy and the electric field. This prediction was closer to the experimental observations. This model was also able to explain the lack of cumulative effect when subjecting a device to multiple pulses prior to electroforming. It is concluded that onset of electroforming is mostly likely an electronic process, as opposed to an ionic one that is often claimed in literature. However, ionic motion is still possible when the localized electric field and temperature increases significantly, bringing about the non-reversible resistance lowering of the device.

Although resistance of all devices after electroforming were found to be in the range of 120-220 Ω, which is at least 5-6 orders of magnitude lower than the pristine device resistance, this low resistance was not a result of any one single isolated conductive filament. Significant decrease in resistivity of the TiO_2 layer was found to occur over half the area of the 5 $\times$ 5 μm devices. All electroformed devices exhibited signs of morphological changes to the top electrode. Pronounced morphological changes were found to result from excessive power dissipation towards the end of the electroforming pulse. The physical extent of the morphological changes, both the halos and blown-

off regions, could be consistently explained using electro-thermal simulation using the assumption of distributed resistance decrease due to electroforming. Such consistency could not be obtained under the assumption that electroforming generates a single dominant small filament (50-500 nm in radius) which alone is responsible for all the observed resistance change.

The primary motivation for this work was to gain a deeper understanding of the electrical and thermal events associated with the electroforming process. The experimentally found relationship among voltage, time, and temperature that triggers electroforming is the first step towards understanding the physical mechanisms that cause formation of conductive filaments. The model based on electric field driven oxygen vacancy migration was found to be a poor fit. This model also fails to explain how large difference between switching and retention times can be achieved using this mechanism alone. Although ReRAM device operation is often attributed to this mechanism, quantitative analysis, as presented in this work revels many discrepancies between the model predictions and the experimental observations. The initial onset of localized current conduction during electroforming is more consistent with a model based on hole trapping. This process gives rise to localized high electric field, which locally increases the current flow and the temperature. These events do not require any vacancy migration. Structural changes in the TiO_2 layer occur under this elevated local temperature condition. Vacancy migration is likely to occur during this step, however the current understanding of the exact mechanism of this process requires significant refinements. It is clear that multiple physical processes are at play during electroforming, and vacancy migration is a small part of the whole story. A unified understanding of the role of each of these mechanisms still remains an open area for future research work.

Appendix A

Thermal Profiles From Electro-thermal Simulations

For each figure below, (a) and (b) shows the thermal profiles at the end of application of a 20 ns pulse. Thermally resistive boundary layer is not taken into account in (a), however it is taken into account in (b). Similarly (c) and (d) shows the thermal profile at the end of application of a 10 μs pulse. Again, thermally resistive boundary layer is not taken into account (c), but it is included in (d). Details of the simulation conditions can be found in chapter 7 section 7.4.

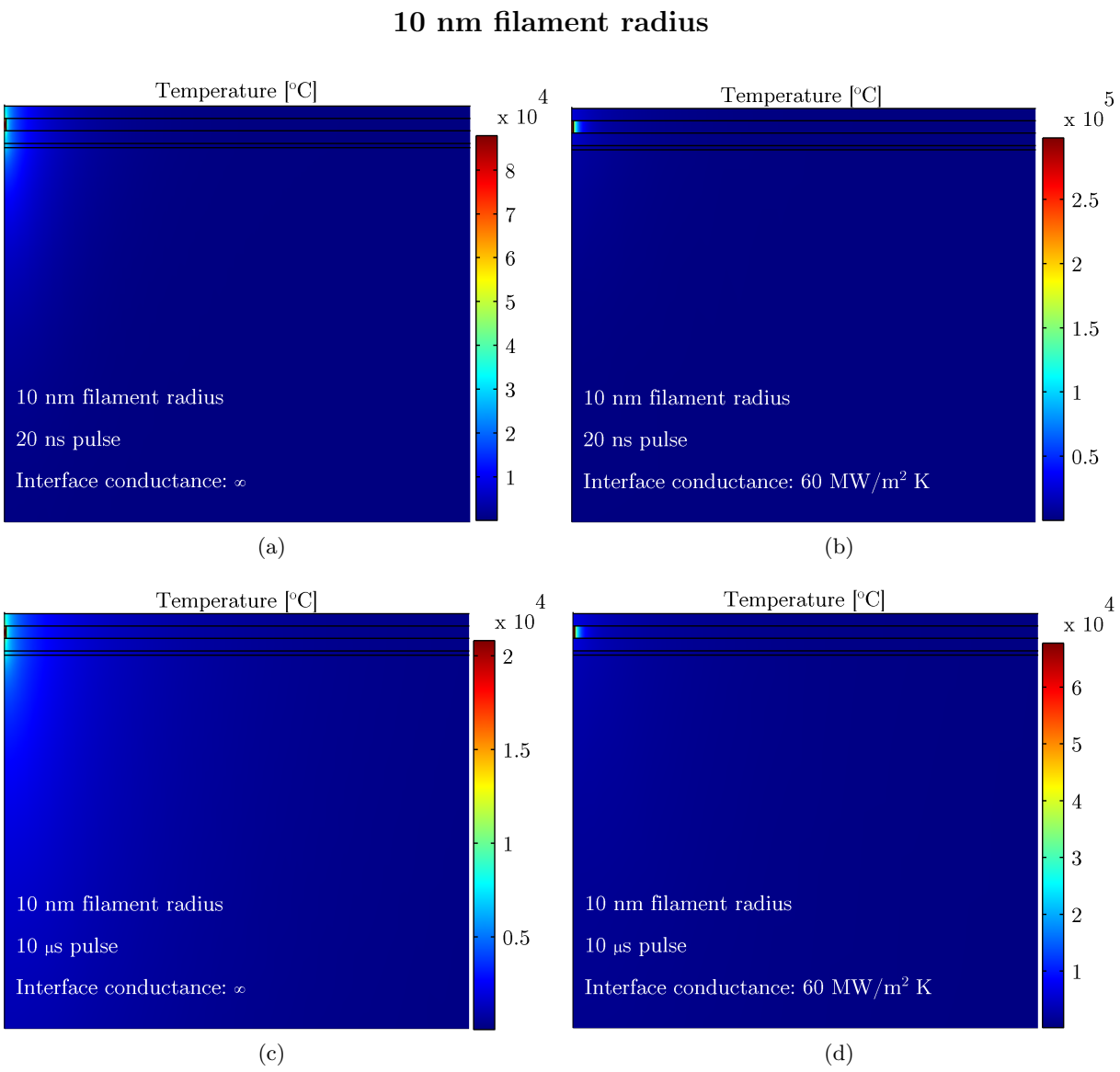

Figure A.1

100 nm filament radius

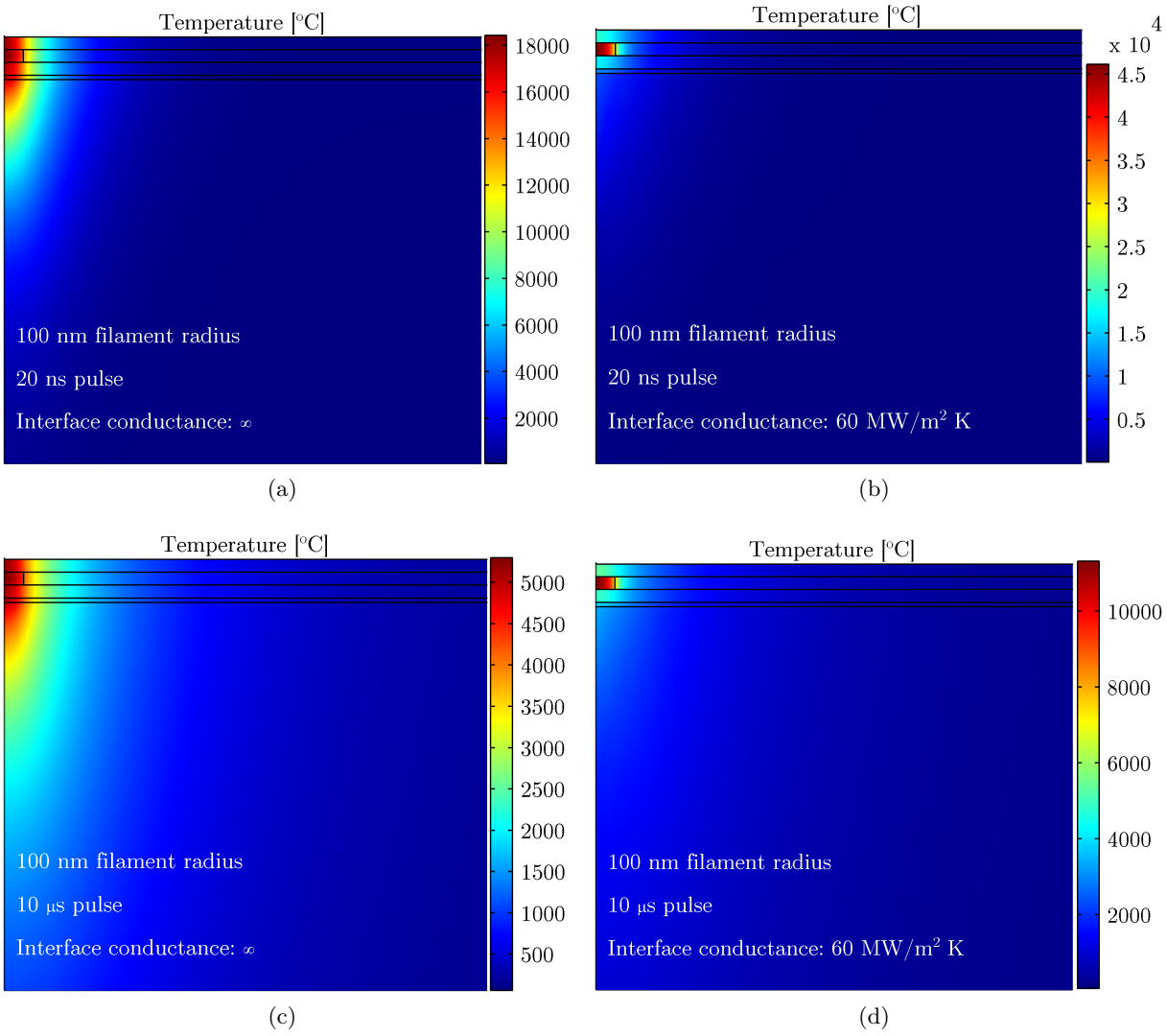

Figure A.2

250 nm filament radius

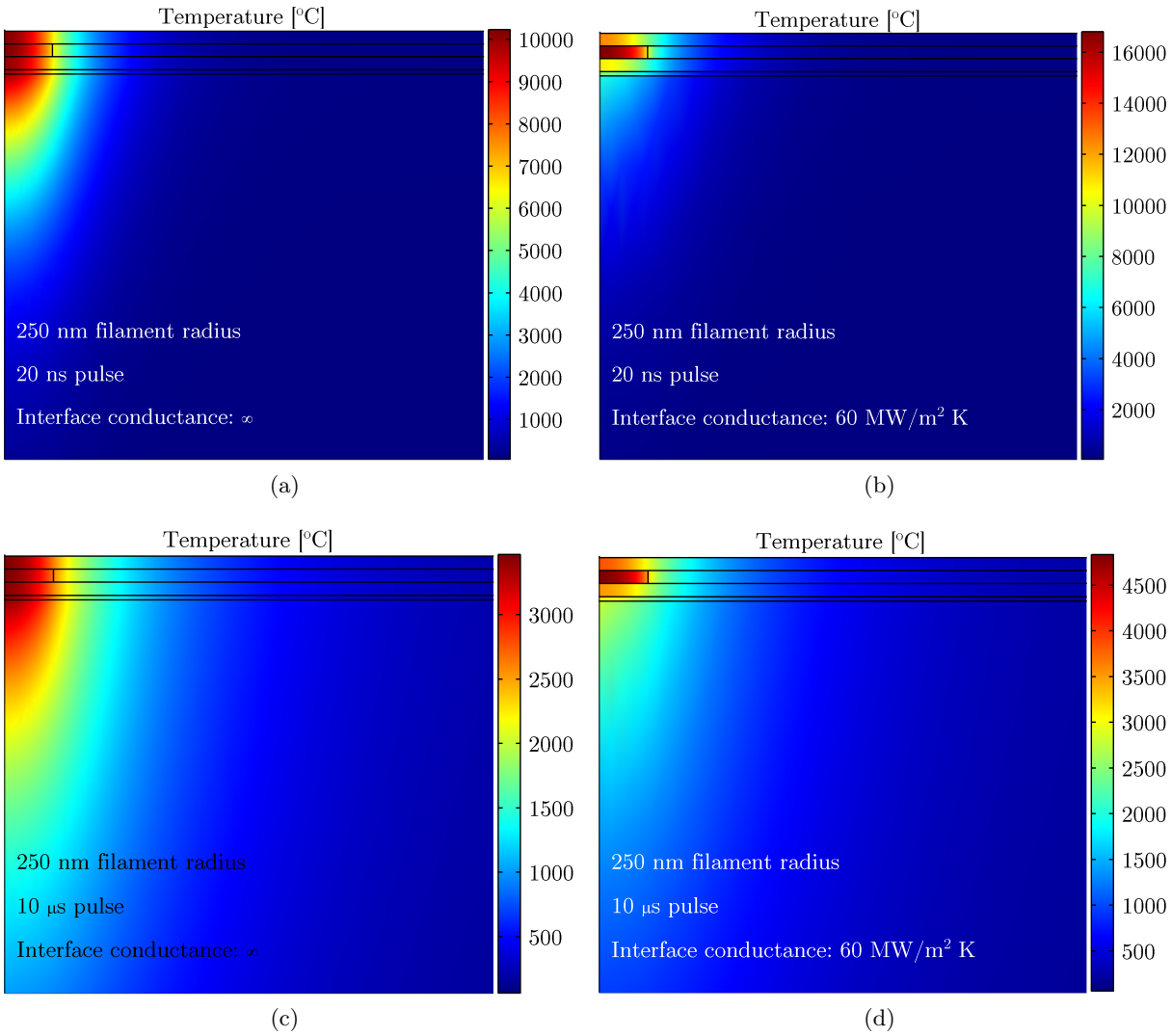

Figure A.3

500 nm filament radius

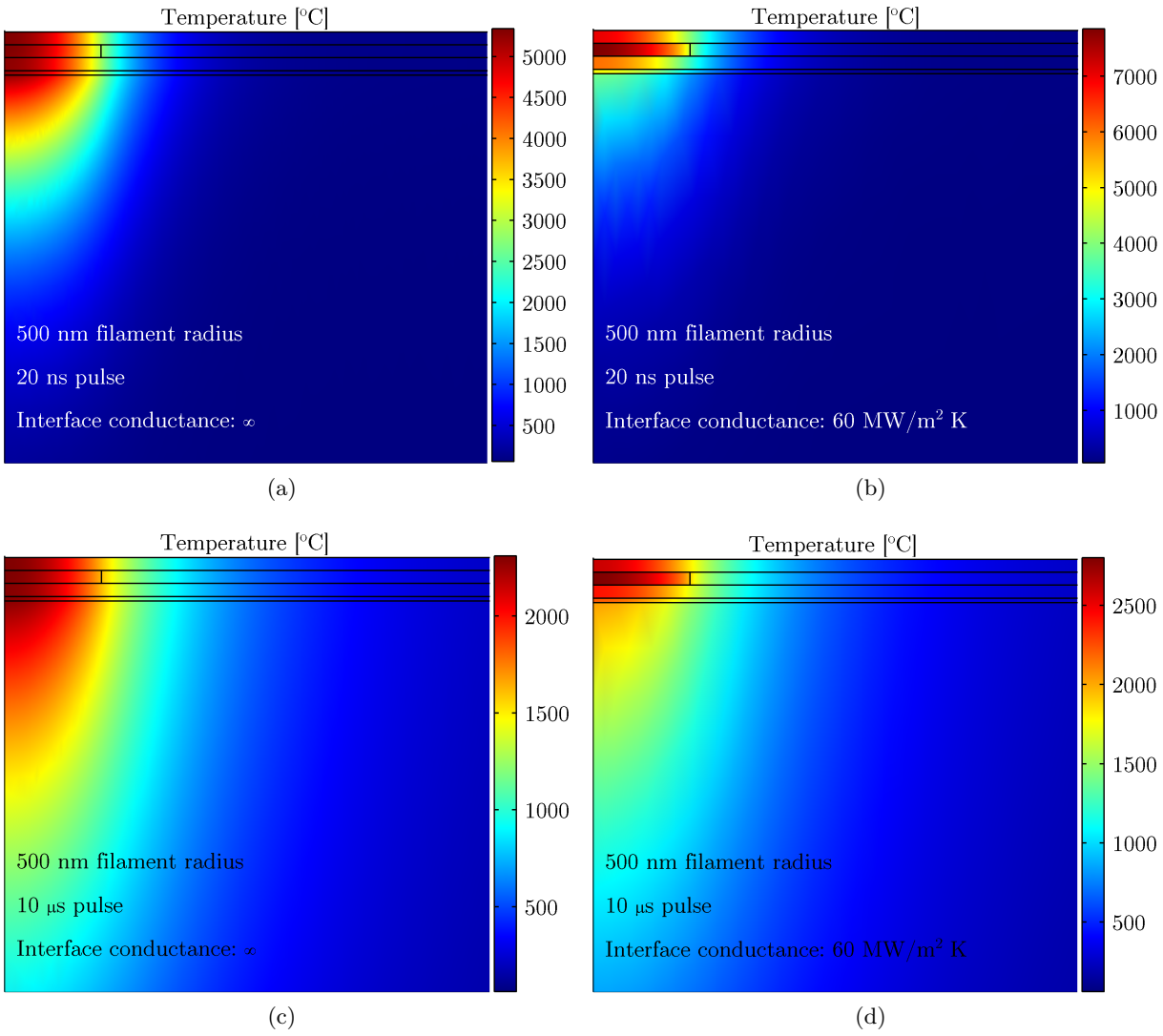

Figure A.4

1 μm filament radius

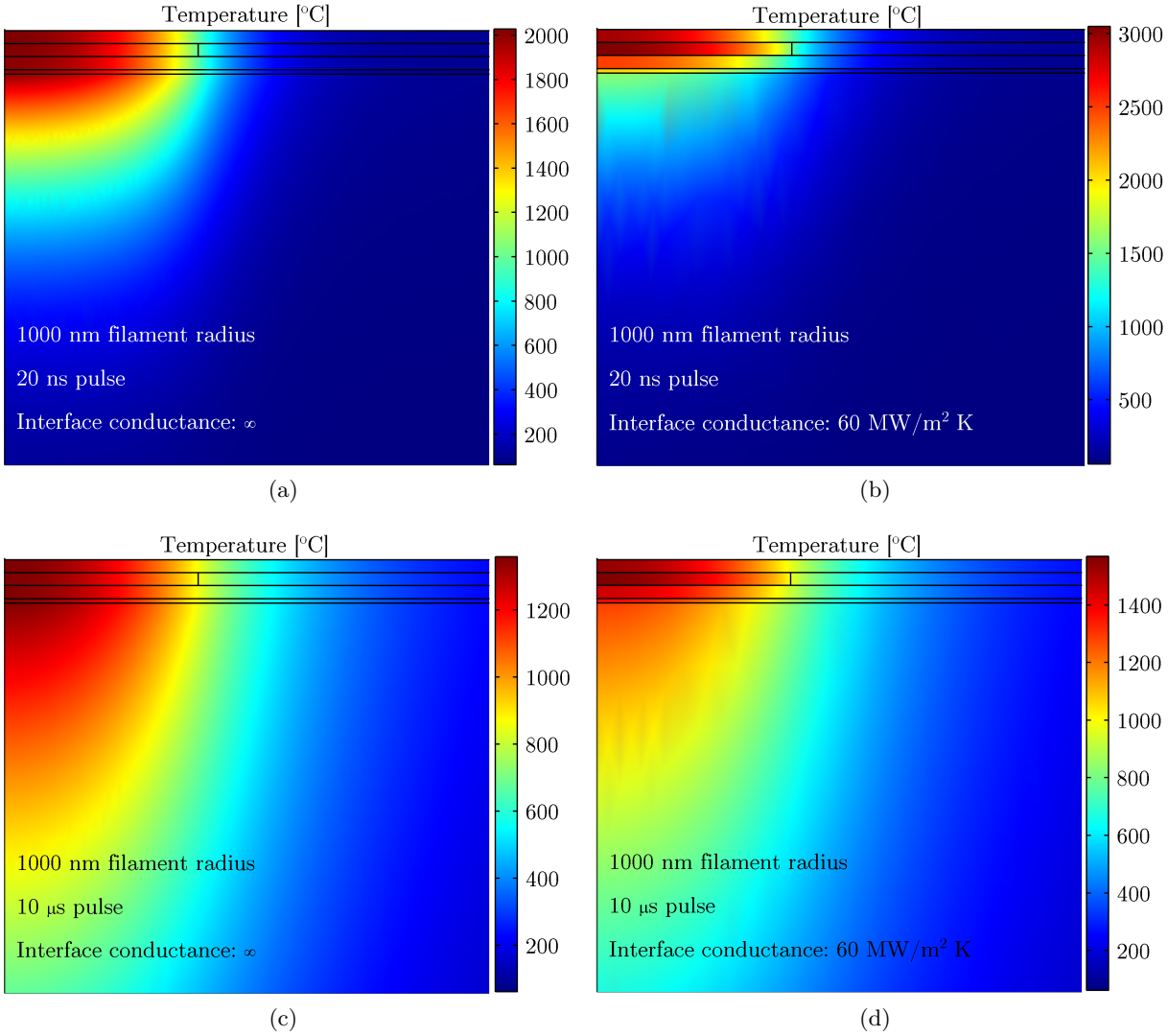

Figure A.5

1.5 μm filament radius

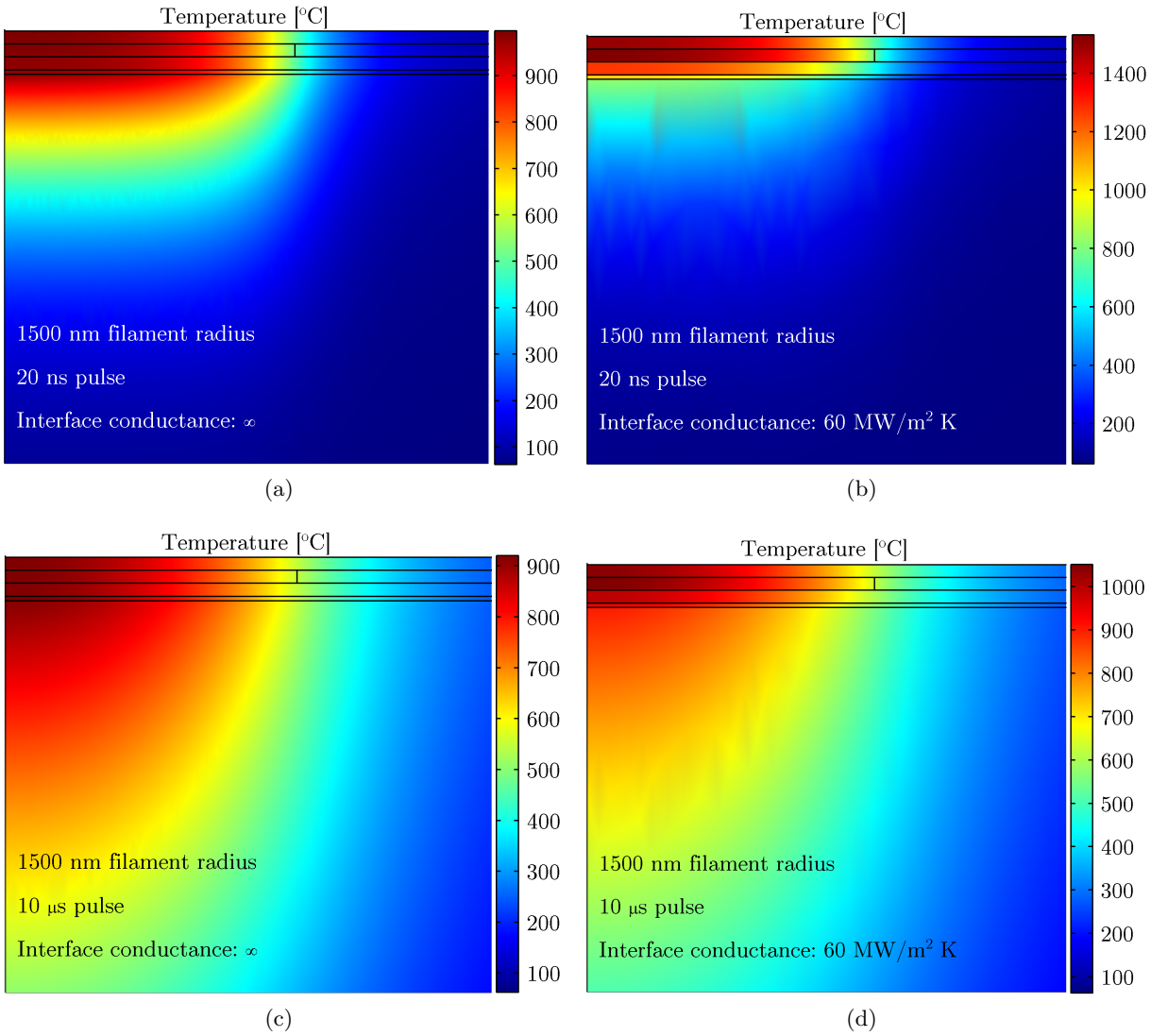

Figure A.6

Appendix B

Images Of Morphological Changes Due to Electroforming

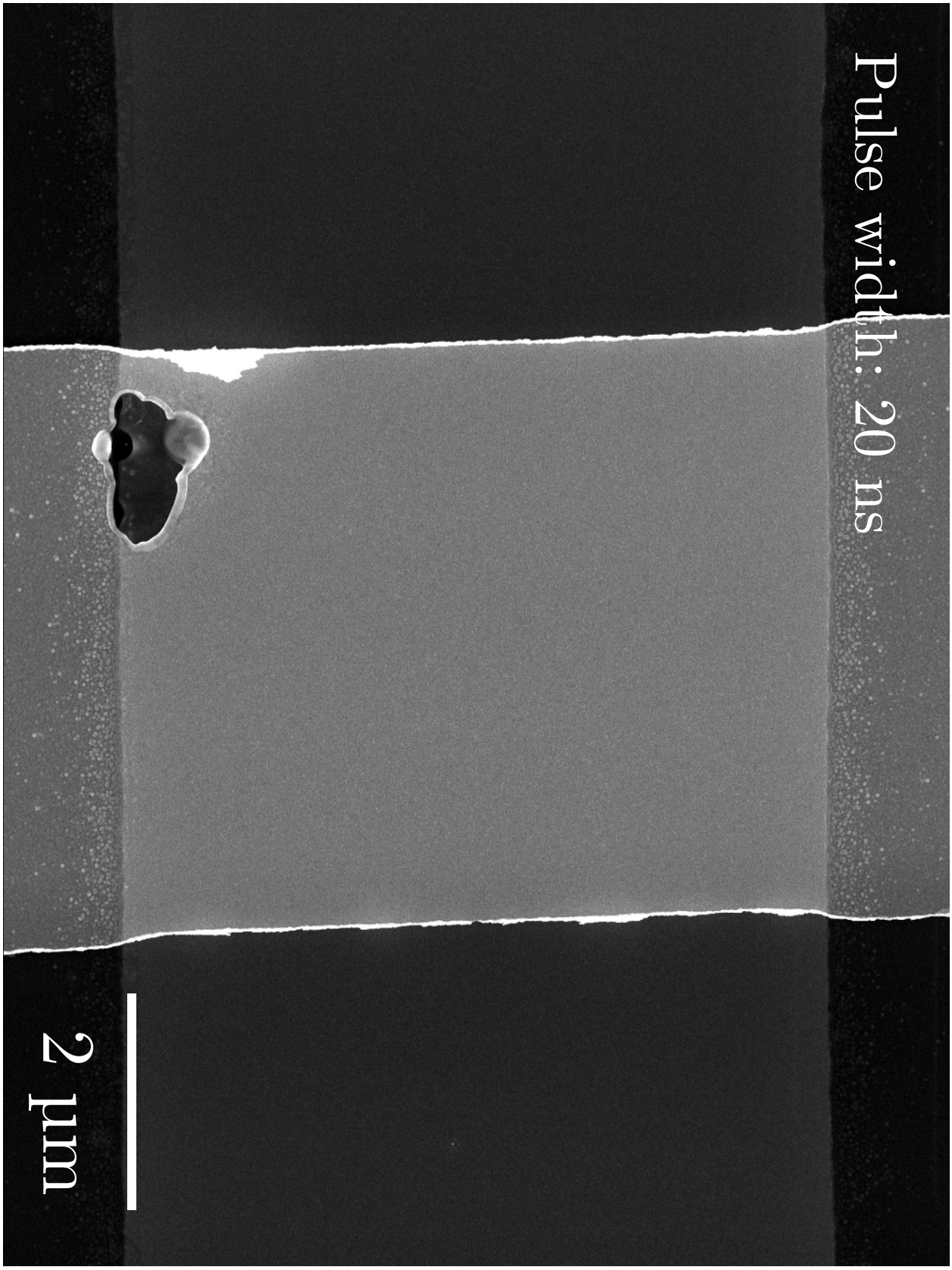

Figure B.1: Morphological changes resulting from electroforming with a 20 ns voltage pulse.

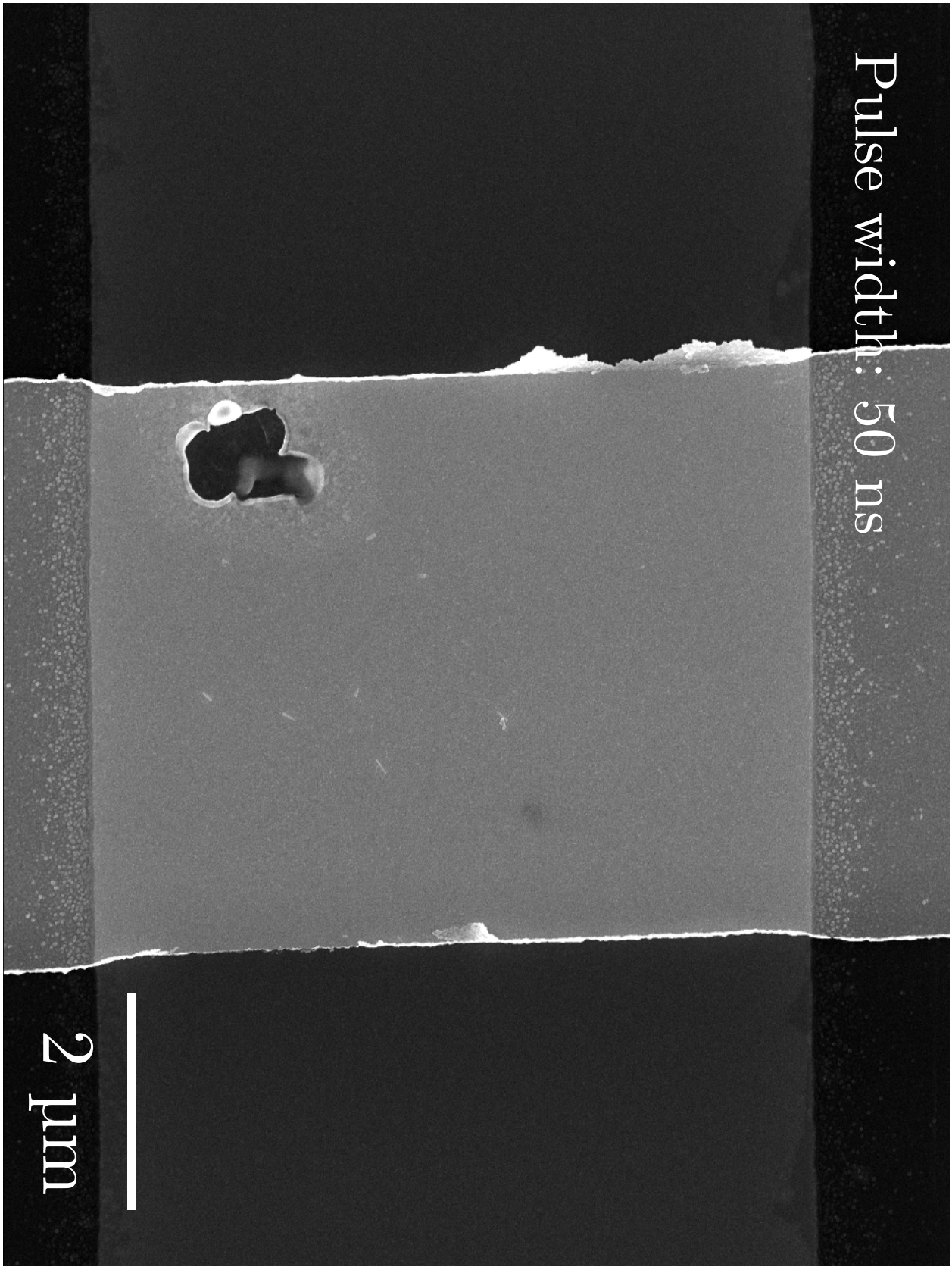

Figure B.2: Morphological changes resulting from electroforming with a 50 ns voltage pulse.

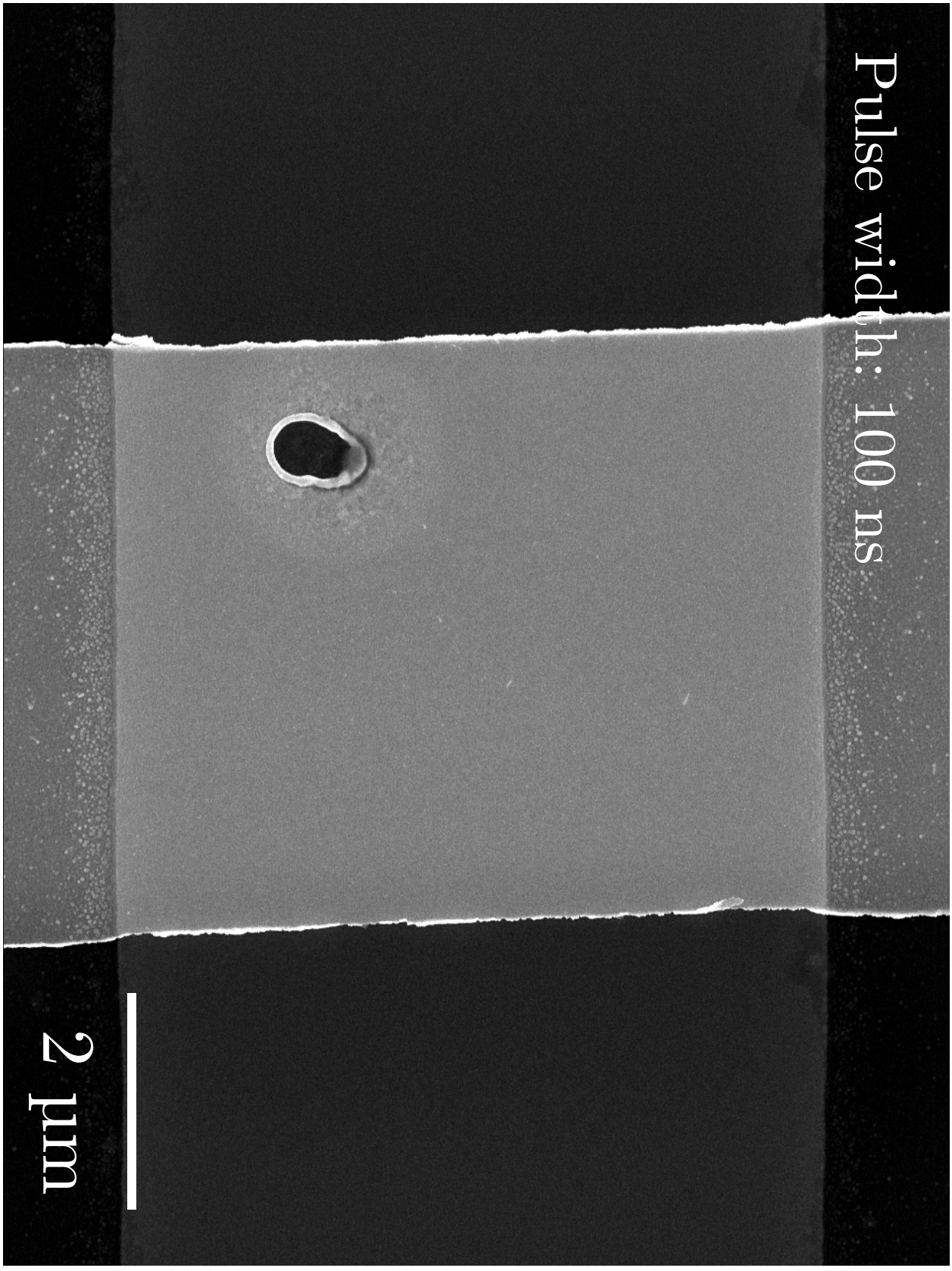

Figure B.3: Morphological changes resulting from electroforming with a 100 ns voltage pulse.

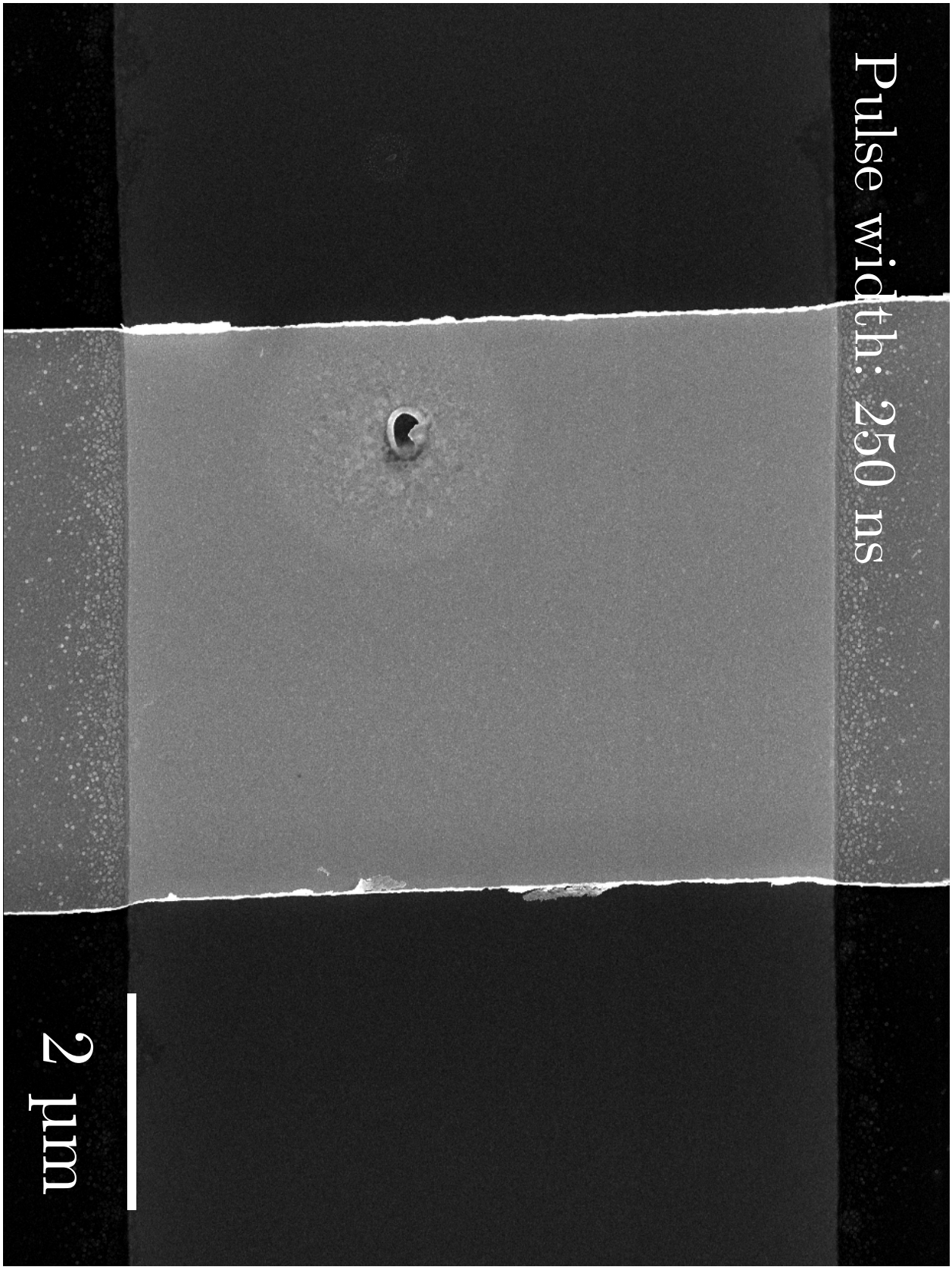

Figure B.4: Morphological changes resulting from electroforming with a 250 ns voltage pulse.

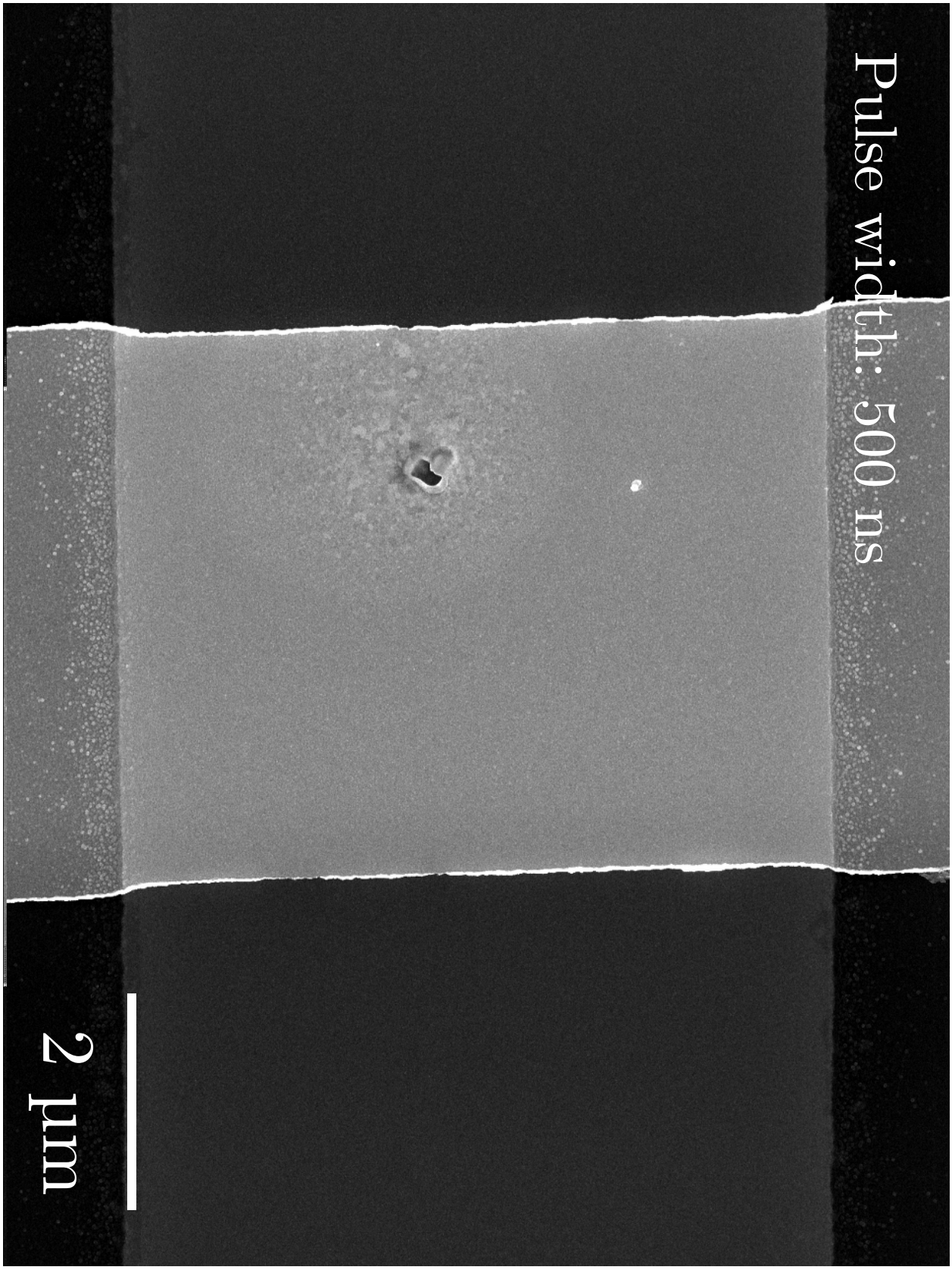

Figure B.5: Morphological changes resulting from electroforming with a 500 ns voltage pulse.

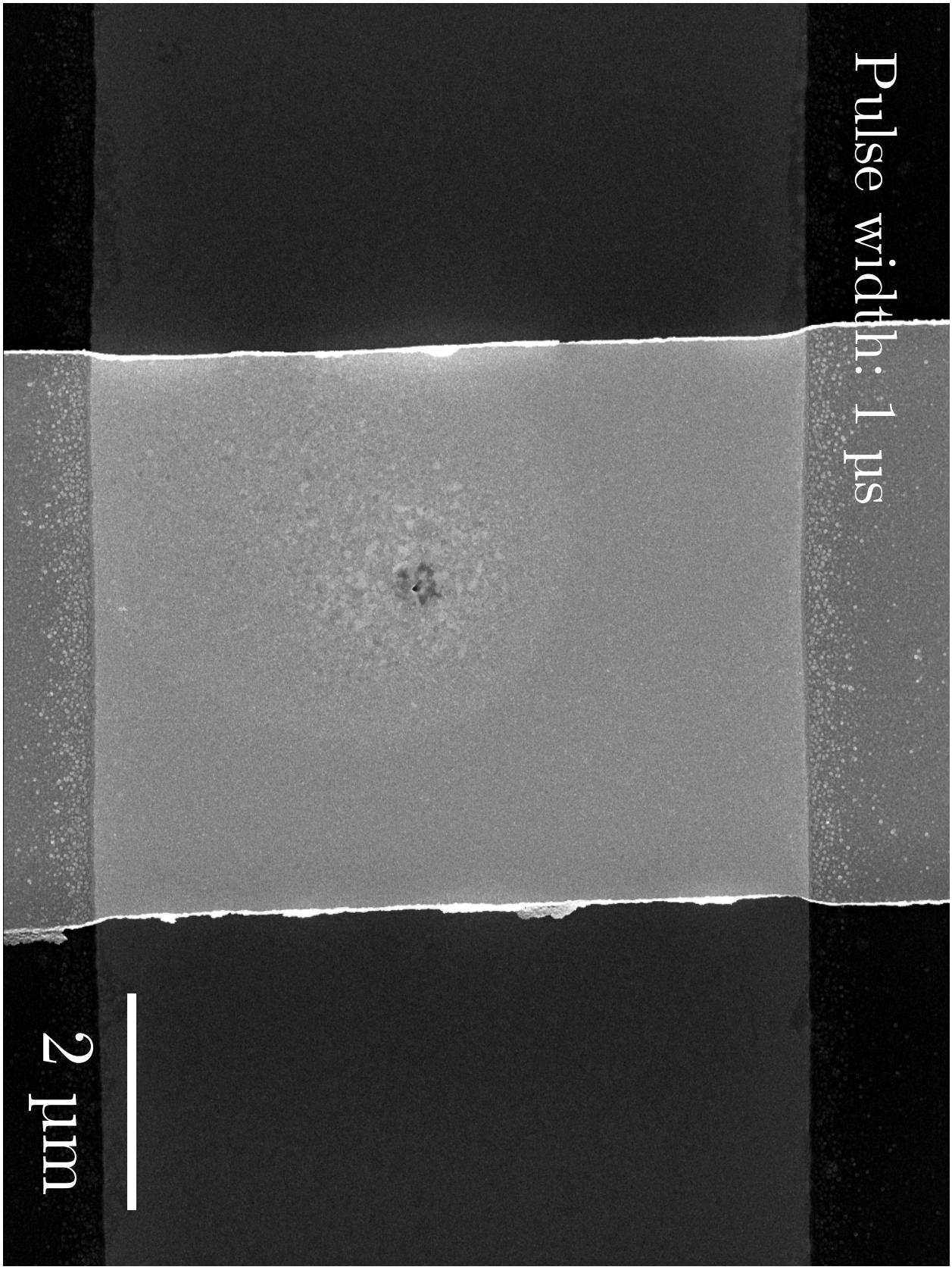

Figure B.6: Morphological changes resulting from electroforming with a 1 μs voltage pulse.

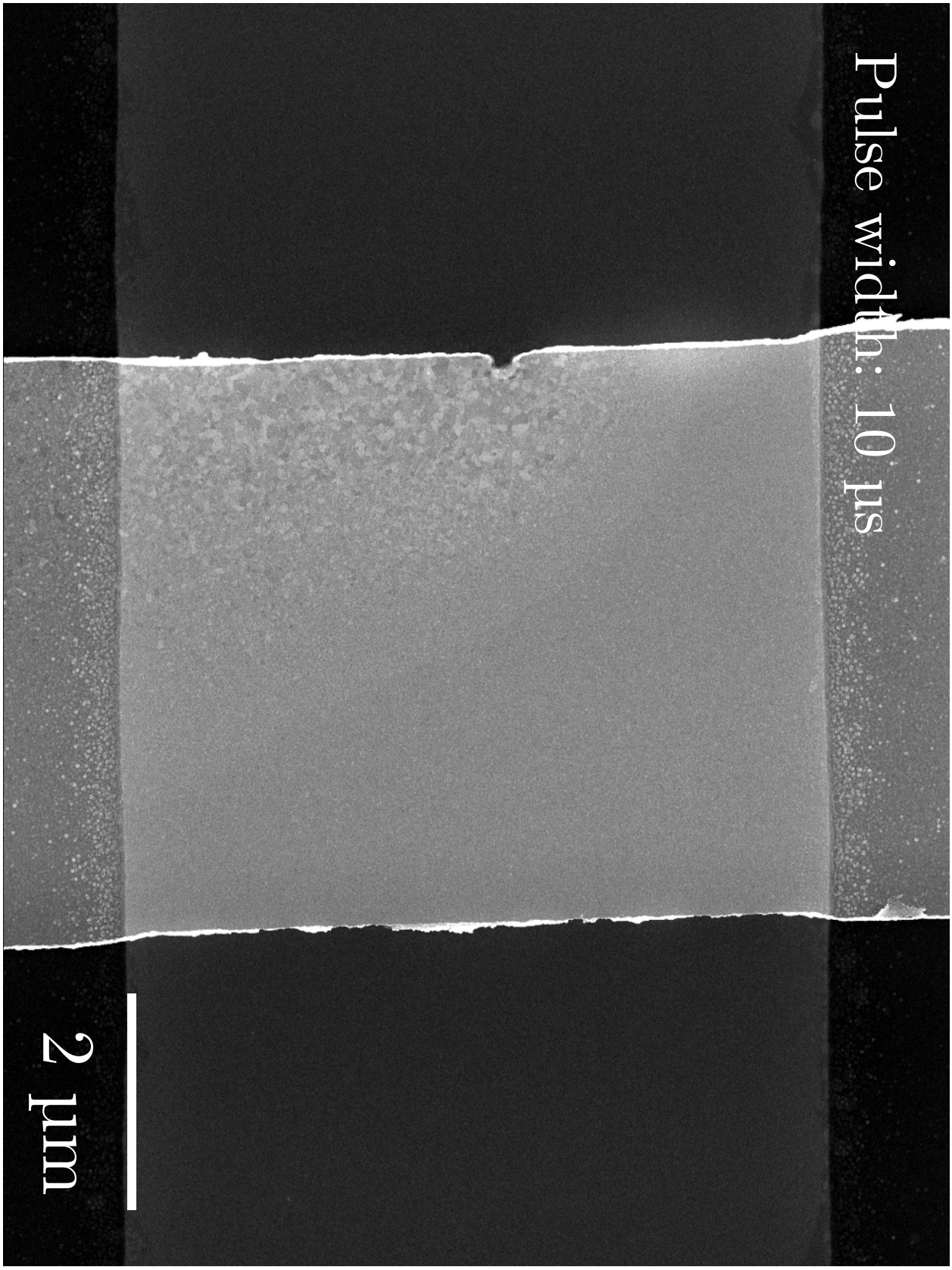

Figure B.7: Morphological changes resulting from electroforming with a 10 μs voltage pulse.

Bibliography

[1] S. Hong, "Memory technology trend and future challenges," *2010 International Electron Devices Meeting*, pp. 12.4.1–12.4.4, Dec. 2010.

[2] S. Lee, "Scaling Challenges in NAND Flash Device toward 10nm Technology," in *2012 4th IEEE International Memory Workshop*, pp. 1–4, IEEE, May 2012.

[3] "International Technology Roadmap For Semiconductors 2011 Edition: Emerging Research Devices (ERD)," *(http://public.itrs.net)*, 2011.

[4] D. B. Strukov, G. S. Snider, D. R. Stewart, and R. S. Williams, "The missing memristor found," *Nature*, vol. 453, pp. 80–3, May 2008.

[5] L. Chua, "Resistance switching memories are memristors," *Applied Physics A*, vol. 102, pp. 765–783, Jan. 2011.

[6] A. Beck, J. G. Bednorz, C. Gerber, C. Rossel, and D. Widmer, "Reproducible switching effect in thin oxide films for memory applications," *Applied Physics Letters*, vol. 77, no. 1, p. 139, 2000.

[7] D. Choi, D. Lee, H. Sim, M. Chang, and H. Hwang, "Reversible resistive switching of $SrTiO_x$ thin films for nonvolatile memory applications," *Applied Physics Letters*, vol. 88, p. 082904, Feb. 2006.

[8] C. Yoshida, K. Tsunoda, H. Noshiro, and Y. Sugiyama, "High speed resistive switching in $Pt/TiO_2/TiN$ film for nonvolatile memory application," *Applied Physics Letters*, vol. 91, p. 223510, Nov. 2007.

[9] W. Robinett, M. Pickett, J. Borghetti, Q. Xia, G. S. Snider, G. Medeiros-Ribeiro, and R. S. Williams, "A memristor-based nonvolatile latch circuit.," *Nanotechnology*, vol. 21, p. 235203, June 2010.

[10] Q. Xia, W. Robinett, M. W. Cumbie, N. Banerjee, T. J. Cardinali, J. J. Yang, W. Wu, X. Li, W. M. Tong, D. B. Strukov, G. S. Snider, G. Medeiros-Ribeiro, and R. S. Williams, "Memristor-CMOS hybrid integrated circuits for reconfigurable logic.," *Nano letters*, vol. 9, pp. 3640–5, Oct. 2009.

[11] J. Borghetti, Z. Li, J. Straznicky, X. Li, D. A. A. Ohlberg, W. Wu, D. R. Stewart, and R. S. Williams, "A hybrid nanomemristor/transistor logic circuit capable of self-programming.," *Proceedings of the National Academy of Sciences of the United States of America*, vol. 106, pp. 1699–703, Feb. 2009.

[12] T. Chang, S.-H. Jo, K.-H. Kim, P. Sheridan, S. Gaba, and W. Lu, "Synaptic behaviors and modeling of a metal oxide memristive device," *Applied Physics A*, vol. 102, pp. 857–863–863, Feb. 2011.

[13] S. H. Jo, T. Chang, I. Ebong, B. B. Bhadviya, P. Mazumder, and W. Lu, "Nanoscale memristor device as synapse in neuromorphic systems.," *Nano letters*, vol. 10, pp. 1297–301, Apr. 2010.

[14] S.-J. Choi, G.-B. Kim, K. Lee, K.-H. Kim, W.-Y. Yang, S. Cho, H.-J. Bae, D.-S. Seo, S.-I. Kim, and K.-J. Lee, "Synaptic behaviors of a single metal-oxide-metal resistive device," *Applied Physics A*, vol. 102, pp. 1019–1025, Jan. 2011.

[15] D. Lee, Y. Sung, I. Lee, J. Kim, H. Sohn, and D.-H. Ko, "Enhanced bipolar resistive switching of HfO_2 with a Ti interlayer," *Applied Physics A*, vol. 102, pp. 997–1001–1001, Feb. 2011.

[16] F. Nardi, S. Larentis, S. Balatti, D. C. Gilmer, and D. Ielmini, "Resistive Switching by Voltage-Driven Ion Migration in Bipolar RRAM-Part I: Experimental Study," *IEEE Transactions on Electron Devices*, vol. 59, pp. 2461–2467, Sept. 2012.

[17] M.-J. Lee, C. B. Lee, D. Lee, S. R. Lee, M. Chang, J. H. Hur, Y.-B. Kim, C.-J. Kim, D. H. Seo, S. Seo, U.-I. Chung, I.-K. Yoo, and K. Kim, "A fast, high-endurance and scalable non-volatile memory device made from asymmetric Ta_2O_{5-x}/TaO_{2-x} bilayer structures.," *Nature materials*, vol. 10, pp. 625–30, Jan. 2011.

[18] J. J. Yang, M.-X. Zhang, J. P. Strachan, F. Miao, M. D. Pickett, R. D. Kelley, G. Medeiros-Ribeiro, and R. S. Williams, "High switching endurance in TaO_x memristive devices," *Applied Physics Letters*, vol. 97, no. 23, p. 232102, 2010.

[19] S. Seo, M. J. Lee, D. H. Seo, E. J. Jeoung, D.-S. Suh, Y. S. Joung, I. K. Yoo, I. R. Hwang, S. H. Kim, I. S. Byun, J.-S. Kim, J. S. Choi, and B. H. Park, "Reproducible resistance switching in polycrystalline NiO films," *Applied Physics Letters*, vol. 85, p. 5655, Dec. 2004.

[20] C. Cagli, F. Nardi, and D. Ielmini, "Modeling of Set/Reset Operations in NiO-Based Resistive-Switching Memory Devices," *IEEE Transactions on Electron Devices*, vol. 56, pp. 1712–1720, Aug. 2009.

[21] D. C. Kim, S. Seo, S. E. Ahn, D.-S. Suh, M. J. Lee, B.-H. Park, I. K. Yoo, I. G. Baek, H.-J. Kim, E. K. Yim, J. E. Lee, S. O. Park, H. S. Kim, U.-I. Chung, J. T. Moon, and B. I. Ryu, "Electrical observations of filamentary conductions for the resistive memory switching in NiO films," *Applied Physics Letters*, vol. 88, no. 20, p. 202102, 2006.

[22] C. H. Kim, H. B. Moon, S. S. Min, Y. H. Jang, and J. H. Cho, "Nanoscale formation mechanism of conducting filaments in NiO thin films," *Solid State Communications*, vol. 149, pp. 1611–1615, Oct. 2009.

[23] X. B. Yan, Y. D. Xia, H. N. Xu, X. Gao, H. T. Li, R. Li, J. Yin, and Z. G. Liu, "Effects of the electroforming polarity on bipolar resistive switching characteristics of $SrTiO_{3-\delta}$ films," *Applied Physics Letters*, vol. 97, no. 11, p. 112101, 2010.

[24] T. Fujii, M. Kawasaki, A. Sawa, H. Akoh, Y. Kawazoe, and Y. Tokura, "Hysteretic current-voltage characteristics and resistance switching at an epitaxial oxide Schottky junction $SrRuO_3SrTi_{0.99}Nb_{0.01}O_3$," *Applied Physics Letters*, vol. 86, no. 1, p. 012107, 2005.

[25] Z. Hong-Jian, Z. Xiao-Ping, and Z. Yong-Gang, "Bipolar Resistance Switching Characteristics of ZnO/Nb-Doped $SrTiO_3$ Heterojunctions," *Chinese Physics Letters*, vol. 26, p. 077303, July 2009.

[26] X. T. Zhang, Q. X. Yu, Y. P. Yao, and X. G. Li, "Ultrafast resistive switching in $SrTiO_3$:Nb single crystal," *Applied Physics Letters*, vol. 97, no. 22, p. 222117, 2010.

[27] K. Szot, W. Speier, G. Bihlmayer, and R. Waser, "Switching the electrical resistance of individual dislocations in single-crystalline $SrTiO_3$.," *Nature materials*, vol. 5, pp. 312–20, Apr. 2006.

[28] C. Lin, J. Yu, and T. Tseng, "Stable resistive switching behaviors of sputter deposited V-doped $SrZrO_3$ thin films," *Thin Solid Films*, vol. 516, pp. 402–406, Dec. 2007.

[29] M.-H. Lin, M.-C. Wu, C.-H. Lin, and T.-Y. Tseng, "Resistive switching characteristics and mechanisms of Pt-embedded $SrZrO_3$ memory devices," *Journal of Applied Physics*, vol. 107, no. 12, p. 124117, 2010.

[30] Y. M. Lu, W. Jiang, M. Noman, J. A. Bain, P. A. Salvador, and M. Skowronski, "Thermographic analysis of localized conductive channels in bipolar resistive switching devices," *Journal of Physics D: Applied Physics*, vol. 44, p. 185103, May 2011.

[31] R. Dong, D. S. Lee, W. F. Xiang, S. J. Oh, D. J. Seong, S. H. Heo, H. J. Choi, M. J. Kwon, S. N. Seo, M. B. Pyun, M. Hasan, and H. Hwang, "Reproducible hysteresis and resistive switching in metal-Cu_xO-metal heterostructures," *Applied Physics Letters*, vol. 90, p. 042107, Jan. 2007.

[32] S. Muraoka, K. Osano, Y. Kanzawa, S. Mitani, S. Fujii, K. Katayama, Y. Katoh, Z. Wei, T. Mikawa, K. Arita, Y. Kawashima, R. Azuma, K. Kawai, K. Shimakawa, A. Odagawa, and T. Takagi, "Fast switching and long retention Fe-O ReRAM and its switching mechanism," in *2007 IEEE International Electron Devices Meeting*, pp. 779–782, IEEE, 2007.

[33] C.-Y. Lin, C.-Y. Wu, C.-Y. Wu, C. Hu, and T.-Y. Tseng, "Bistable Resistive Switching in Al_2O_3 Memory Thin Films," *Journal of The Electrochemical Society*, vol. 154, p. G189, Sept. 2007.

[34] N. Xu, L. Liu, X. Sun, X. Liu, D. Han, Y. Wang, R. Han, J. Kang, and B. Yu, "Characteristics and mechanism of conduction/set process in TiN/ZnO/Pt resistance switching random-access memories," *Applied Physics Letters*, vol. 92, p. 232112, June 2008.

[35] W.-Y. Chang, Y.-C. Lai, T.-B. Wu, S.-F. Wang, F. Chen, and M.-J. Tsai, "Unipolar resistive switching characteristics of ZnO thin films for nonvolatile memory applications," *Applied Physics Letters*, vol. 92, p. 022110, Jan. 2008.

[36] K. Nagashima, T. Yanagida, K. Oka, and T. Kawai, "Unipolar resistive switching characteristics of room temperature grown SnO_2 thin films," *Applied Physics Letters*, vol. 94, p. 242902, June 2009.

[37] S. Long, Q. Liu, H. Lv, Y. Li, Y. Wang, S. Zhang, W. Lian, K. Zhang, M. Wang, H. Xie, and M. Liu, "Resistive switching mechanism of Ag/ZrO_2:Cu/Pt memory cell," *Applied Physics A*, vol. 102, pp. 915–919, Jan. 2011.

[38] Q. Liu, W. Guan, S. Long, M. Liu, S. Zhang, Q. Wang, and J. Chen, "Resistance switching of Au-implanted-ZrO_2 film for nonvolatile memory application," *Journal of Applied Physics*, vol. 104, no. 11, p. 114514, 2008.

[39] C.-Y. Lin, C.-Y. Wu, C.-Y. Wu, T.-C. Lee, F.-L. Yang, C. Hu, and T.-Y. Tseng, "Effect of Top Electrode Material on Resistive Switching Properties of ZrO_2 Film Memory Devices," *IEEE Electron Device Letters*, vol. 28, pp. 366–368, May 2007.

[40] C. Schindler, G. Staikov, and R. Waser, "Electrode kinetics of $CuSiO_2$-based resistive switching cells: Overcoming the voltage-time dilemma of electrochemical metallization memories," *Applied Physics Letters*, vol. 94, p. 072109, Feb. 2009.

[41] C. Schindler, S. C. P. Thermadam, R. Waser, and M. N. Kozicki, "Bipolar and Unipolar Resistive Switching in Cu-Doped SiO_2," *IEEE Transactions on Electron Devices*, vol. 54, pp. 2762–2768, Oct. 2007.

[42] J. Blanc and D. Staebler, "Electrocoloration in $SrTiO_3$: Vacancy Drift and Oxidation-Reduction of Transition Metals," *Physical Review B*, vol. 4, pp. 3548–3557, Nov. 1971.

[43] A. Bagshaw and B. Hyde, "Oxygen tracer diffusion in the magnéli phases Ti_nO_{2n-1}," *Journal of Physics and Chemistry of Solids*, vol. 37, no. 9, pp. 835–838, 1976.

[44] R. Meyer, R. Waser, J. Helmbold, and G. Borchardt, "Observation of Vacancy Defect Migration in the Cation Sublattice of Complex Oxides by O_{18} Tracer Experiments," *Physical Review Letters*, vol. 90, Mar. 2003.

[45] S. Huerth, H. Hallen, and B. Moeckly, "Spectroscopy of voltage dependence of oxygen movement in $YBa_2Cu_3O_{7-\delta}$," *Physical Review B*, vol. 67, May 2003.

[46] J. Kilner, "Fast oxygen transport in acceptor doped oxides," *Solid State Ionics*, vol. 129, pp. 13–23, Apr. 2000.

[47] H.-I. Yoo, M.-W. Chang, T.-S. Oh, C.-E. Lee, and K. D. Becker, "Electrocoloration and oxygen vacancy mobility of $BaTiO_3$," *Journal of Applied Physics*, vol. 102, p. 093701, Nov. 2007.

[48] R. Merkle and J. Maier, "How Is Oxygen Incorporated into Oxides? A Comprehensive Kinetic Study of a Simple Solid-State Reaction with $SrTiO_3$ as a Model Material," *ChemInform*, vol. 39, July 2008.

[49] S. H. Jeon, B. H. Park, J. Lee, B. Lee, and S. Han, "First-principles modeling of resistance switching in perovskite oxide material," *Applied Physics Letters*, vol. 89, p. 042904, July 2006.

[50] K. Szot, M. Rogala, W. Speier, Z. Klusek, A. Besmehn, and R. Waser, "TiO_2-a prototypical memristive material.," *Nanotechnology*, vol. 22, p. 254001, June 2011.

[51] R. Waser, R. Dittmann, G. Staikov, and K. Szot, "Redox-Based Resistive Switching Memories - Nanoionic Mechanisms, Prospects, and Challenges," *Advanced Materials*, vol. 21, pp. 2632–2663, July 2009.

[52] D. B. Strukov and R. S. Williams, "Exponential ionic drift: fast switching and low volatility of thin-film memristors," *Applied Physics A*, vol. 94, pp. 515–519, Nov. 2009.

[53] K. M. Kim, D. S. Jeong, and C. S. Hwang, "Nanofilamentary resistive switching in binary oxide system; a review on the present status and outlook.," *Nanotechnology*, vol. 22, p. 254002, June 2011.

[54] R. Münstermann, J. J. Yang, J. P. Strachan, G. Medeiros-Ribeiro, R. Dittmann, and R. Waser, "Morphological and electrical changes in TiO_2 memristive devices induced by electroforming and switching," *physica status solidi (RRL) - Rapid Research Letters*, vol. 4, pp. 16–18, Feb. 2010.

[55] J. P. Strachan, M. D. Pickett, J. J. Yang, S. Aloni, A. L. David Kilcoyne, G. Medeiros-Ribeiro, and R. Stanley Williams, "Direct identification of the conducting channels in a functioning memristive device.," *Advanced materials*, vol. 22, pp. 3573–7, Aug. 2010.

[56] J. Joshua Yang, F. Miao, M. D. Pickett, D. A. A. Ohlberg, D. R. Stewart, C. N. Lau, and R. S. Williams, "The mechanism of electroforming of metal oxide memristive switches.," *Nanotechnology*, vol. 20, p. 215201, May 2009.

[57] A. Sawa, T. Fujii, M. Kawasaki, and Y. Tokura, "Hysteretic current-voltage characteristics and resistance switching at a rectifying $Ti/Pr_{0.7}Ca_{0.3}MnO_3$ interface," *Applied Physics Letters*, vol. 85, no. 18, p. 4073, 2004.

[58] S. Sakai and R. Ilangovan, "MetalFerroelectricInsulatorSemiconductor Memory FET With Long Retention and High Endurance," *IEEE Electron Device Letters*, vol. 25, pp. 369–371, June 2004.

[59] Y. Hirose and H. Hirose, "Polarity-dependent memory switching and behavior of Ag dendrite in Ag-photodoped amorphous As_2S_3 films," *Journal of Applied Physics*, vol. 47, p. 2767, June 1976.

[60] S. H. Chang, S. C. Chae, S. B. Lee, C. Liu, T. W. Noh, J. S. Lee, B. Kahng, J. H. Jang, M. Y. Kim, D.-W. Kim, and C. U. Jung, "Effects of heat dissipation on unipolar resistance switching in Pt/NiO/Pt capacitors," *Applied Physics Letters*, vol. 92, p. 183507, May 2008.

[61] H. Lee, Y. Chen, P. Chen, T. Wu, F. Chen, C. Wang, P. Tzeng, M.-J. Tsai, and C. Lien, "Low-Power and Nanosecond Switching in Robust Hafnium Oxide Resistive Memory With a Thin Ti Cap," *IEEE Electron Device Letters*, vol. 31, pp. 44–46, Jan. 2010.

[62] D. S. Jeong, H. Schroeder, and R. Waser, "Coexistence of Bipolar and Unipolar Resistive Switching Behaviors in a $Pt/TiO_2/Pt$ Stack," *Electrochemical and Solid-State Letters*, vol. 10, no. 8, p. G51, 2007.

[63] J. J. Yang, J. Borghetti, D. Murphy, D. R. Stewart, and R. S. Williams, "A Family of Electronically Reconfigurable Nanodevices," *Advanced Materials*, vol. 21, pp. 3754–3758, Oct. 2009.

[64] J. J. Yang, J. P. Strachan, F. Miao, M.-X. Zhang, M. D. Pickett, W. Yi, D. A. A. Ohlberg, G. Medeiros-Ribeiro, and R. S. Williams, "$Metal/TiO_2$ interfaces for memristive switches," *Applied Physics A*, vol. 102, pp. 785–789, Jan. 2011.

[65] H. Y. Jeong, S. K. Kim, J. Y. Lee, and S.-Y. Choi, "Impact of amorphous titanium oxide film on the device stability of $Al/TiO_2/Al$ resistive memory," *Applied Physics A*, vol. 102, pp. 967–972, Jan. 2011.

[66] H. Mähne and S. Slesazeck, "The influence of crystallinity on the resistive switching behavior of TiO_2," *Microelectronic Engineering*, vol. 88, no. 7, pp. 1148–1151, 2011.

[67] F. Miao, J. Joshua Yang, J. Borghetti, G. Medeiros-Ribeiro, and R. Stanley Williams, "Observation of two resistance switching modes in TiO_2 memristive devices electroformed at low current.," *Nanotechnology*, vol. 22, p. 254007, June 2011.

[68] K. M. Kim, G. H. Kim, S. J. Song, J. Y. Seok, M. H. Lee, J. H. Yoon, and C. S. Hwang, "Electrically configurable electroforming and bipolar resistive switching in $Pt/TiO_2/Pt$ structures.," *Nanotechnology*, vol. 21, p. 305203, July 2010.

[69] F. Miao, J. P. Strachan, J. J. Yang, M.-X. Zhang, I. Goldfarb, A. C. Torrezan, P. Eschbach, R. D. Kelley, G. Medeiros-Ribeiro, and R. S. Williams, "Anatomy of a nanoscale conduction channel reveals the mechanism of a high-performance memristor," *Advanced materials*, vol. 23, pp. 5633–40, Dec. 2011.

[70] D.-H. Kwon, K. M. Kim, J. H. Jang, J. M. Jeon, M. H. Lee, G. H. Kim, X.-S. Li, G.-S. Park, B. Lee, S. Han, M. Kim, and C. S. Hwang, "Atomic structure of conducting nanofilaments in TiO_2 resistive switching memory.," *Nature nanotechnology*, vol. 5, pp. 148–53, Feb. 2010.

[71] G. Hwan Kim, J. Ho Lee, J. Yeong Seok, S. Ji Song, J. Ho Yoon, K. Jean Yoon, M. Hwan Lee, K. Min Kim, H. Dong Lee, S. Wook Ryu, T. Joo Park, and C. Seong Hwang, "Improved endurance of resistive switching TiO_2 thin film by hourglass shaped Magneli filaments," *Applied Physics Letters*, vol. 98, p. 262901, June 2011.

[72] J.-J. Huang, C.-W. Kuo, W.-C. Chang, and T.-H. Hou, "Transition of stable rectification to resistive-switching in $Ti/TiO_2/Pt$ oxide diode," *Applied Physics Letters*, vol. 96, no. 26, p. 262901, 2010.

[73] H. Shima, N. Zhong, and H. Akinaga, "Switchable rectifier built with $Pt/TiO_x/Pt$ trilayer," *Applied Physics Letters*, vol. 94, no. 8, p. 082905, 2009.

[74] C. Nauenheim, C. Kuegeler, A. Ruediger, and R. Waser, "Investigation of the electroforming process in resistively switching TiO_2 nanocrosspoint junctions," *Applied Physics Letters*, vol. 96, no. 12, p. 122902, 2010.

[75] M. K. Nowotny, T. Bak, and J. Nowotny, "Electrical properties and defect chemistry of TiO_2 single crystal. I. Electrical conductivity.," *The journal of physical chemistry. B*, vol. 110, pp. 16270–82, Aug. 2006.

[76] A. Weibel, R. Bouchet, and P. Knauth, "Electrical properties and defect chemistry of anatase (TiO_2)," *Solid State Ionics*, vol. 177, pp. 229–236, Jan. 2006.

[77] L. Liborio and N. Harrison, "Thermodynamics of oxygen defective Magnéli phases in rutile: A first-principles study," *Physical Review B*, vol. 77, Mar. 2008.

[78] J. J. Yang, M. D. Pickett, X. Li, D. A. A. Ohlberg, D. R. Stewart, and R. S. Williams, "Memristive switching mechanism for metal/oxide/metal nanodevices.," *Nature nanotechnology*, vol. 3, pp. 429–33, July 2008.

[79] M. Noman, W. Jiang, P. A. Salvador, M. Skowronski, and J. A. Bain, "Computational investigations into the operating window formemristive devices based on homogeneous ionic motion," *Applied Physics A*, vol. 102, pp. 877–883–883, Jan. 2011.

[80] R. Bartholomew and D. Frankl, "Electrical Properties of Some Titanium Oxides," *Physical Review*, vol. 187, pp. 828–833, Nov. 1969.

[81] D. S. Jeong, *Resistive Switching in Pt/TiO_2/Pt*. PhD thesis, 2008.

[82] J. P. Strachan, J. Joshua Yang, R. Münstermann, A. Scholl, G. Medeiros-Ribeiro, D. R. Stewart, and R. Stanley Williams, "Structural and chemical characterization of TiO_2 memristive devices by spatially-resolved NEXAFS.," *Nanotechnology*, vol. 20, p. 485701, Dec. 2009.

[83] Y. Lu, *Identification and characterization of localized conductivity changes in resistive switching devices*. PhD thesis, Carnegie Mellon University, 2012.

[84] J. J. Yang, J. P. Strachan, Q. Xia, D. A. A. Ohlberg, P. J. Kuekes, R. D. Kelley, W. F. Stickle, D. R. Stewart, G. Medeiros-Ribeiro, and R. S. Williams, "Diffusion of Adhesion Layer Metals Controls Nanoscale Memristive Switching," *Advanced Materials*, vol. 22, pp. 4034–4038, July 2010.

[85] D. B. Strukov, J. L. Borghetti, and R. S. Williams, "Coupled ionic and electronic transport model of thin-film semiconductor memristive behavior.," *Small*, vol. 5, pp. 1058–63, May 2009.

[86] W. Jiang, D. Evans, J. A. Bain, M. Skowronski, and P. A. Salvador, "Electron beam induced current investigations of Pt/$SrTiO_{3-x}$ interface exposed to chemical and electrical stresses," *Applied Physics Letters*, vol. 96, p. 092102, Mar. 2010.

[87] R. Moos, W. Menesklou, and K. H. Härdtl, "Hall-mobility of undoped n-type conducting strontium titanate single crystal between 19 K and 1373 K," *Applied Physics A*, vol. 61, no. 4, pp. 389–395, 1995.

[88] J. Maier, *Physical Chemistry of Ionic Materials*. Wiley, Weinheim, 2004.

[89] C. R. Crowell and V. L. Rideout, "Normalized thermionic-field (T-F) emission in metal-semiconductor (Schottky) barriers," *Solid-State Electronics*, vol. 12, pp. 89–105, Feb. 1969.

[90] S. A. Chambers, Y. Liang, Z. Yu, R. Droopad, J. Ramdani, and K. Eisenbeiser, "Band discontinuities at epitaxial $SrTiO_3$/Si(001) heterojunctions," *Applied Physics Letters*, vol. 77, no. 11, p. 1662, 2000.

[91] G. Choi, H. Tuller, and D. Goldschmidt, "Electronic-transport behavior in single-crystalline $Ba_{0.03}Sr_{0.97}TiO_3$," *Physical Review B*, vol. 34, pp. 6972–6979, Nov. 1986.

[92] R. Waser, T. Baiatu, and K.-H. Härdtl, "DC Electrical Degradation of Perovskite-Type Titanates: I, Ceramics," *Journal of the American Ceramic Society*, vol. 73, pp. 1645–1653, June 1990.

[93] H.-M. Christen, J. Mannhart, E. Williams, and C. Gerber, "Dielectric properties of sputtered $SrTiO_3$ films," *Physical Review B*, vol. 49, pp. 12095–12104, May 1994.

[94] H. Yamada, "Point defects in reduced strontium titanate," *Journal of Solid State Chemistry*, vol. 6, pp. 169–177, Jan. 1973.

[95] K. Govinda Rajan, P. Parameshwaran, J. Janaki, and T. S. Radhakrishnan, "Electromigration of oxygen in $YBa_2Cu_3O_{7-\delta}$," *Journal of Physics D: Applied Physics*, vol. 23, no. 6, p. 694, 1990.

[96] H. B. Huntington and A. R. Grone, "Current-induced marker motion in gold wires," *Journal of Physics and Chemistry of Solids*, vol. 20, pp. 76–87, June 1961.

[97] L. Errico, G. Fabricius, M. Rentería, P. de La Presa, and M. Forker, "Anisotropic Relaxations Introduced by Cd Impurities in Rutile TiO_2: First-PrinciplesCalculations and Experimental Support," *Physical review letters*, vol. 89, no. 5, p. 55503, 2002.

[98] J. McPherson, J. Kim, A. Shanware, H. Mogul, and J. Rodriguez, "Trends in the ultimate breakdown strength of high dielectric-constant materials," *Electron Devices, IEEE Transactions on*, vol. 50, no. 8, pp. 1771–1778, 2003.

[99] A. Lidiard, "Ionic conductivity," *Handbuch der Physik*, vol. 20, pp. 246–349, 1957.

[100] R W Munn, "Local-field effects on carrier hopping mobilities," *Journal of Physics C: Solid State Physics*, vol. 8, no. 17, p. 2721, 1975.

[101] D. B. Strukov and R. S. Williams, "An ionic bottle for high-speed, long-retention memristive devices," *Applied Physics A*, vol. 102, pp. 1033–1036–1036, Feb. 2011.

[102] S. B. Lee, D.-H. Kwon, K. Kim, H. K. Yoo, S. Sinn, M. Kim, B. Kahng, and B. S. Kang, "Avoiding fatal damage to the top electrodes when forming unipolar resistance switching in nano-thick material systems," *Journal of Physics D: Applied Physics*, vol. 45, p. 255101, June 2012.

[103] S. B. Lee, H. K. Yoo, S. H. Chang, L. G. Gao, B. S. Kang, M.-J. Lee, C. J. Kim, and T. W. Noh, "Time-dependent current-voltage curves during the forming process in unipolar resistance switching," *Applied Physics Letters*, vol. 98, p. 053503, Feb. 2011.

[104] J. Verweij and J. Klootwijk, "Dielectric breakdown I: A review of oxide breakdown," *Microelectronics Journal*, vol. 27, pp. 611–622, Oct. 1996.

[105] K. Schuegraf, "Effects of temperature and defects on breakdown lifetime of thin SiO_2 at very low voltages," *IEEE Transactions on Electron Devices*, vol. 41, pp. 1227–1232, July 1994.

[106] R. Degraeve, J. Ogier, R. Bellens, P. Roussel, G. Groeseneken, and H. Maes, "A new model for the field dependence of intrinsic and extrinsic time-dependent dielectric breakdown," *IEEE Transactions on Electron Devices*, vol. 45, no. 2, pp. 472–481, 1998.

[107] S. Lombardo, A. La Magna, C. Spinella, C. Gerardi, and F. Crupi, "Degradation and hard breakdown transient of thin gate oxides in metal-SiO_2-Si capacitors: Dependence on oxide thickness," *Journal of Applied Physics*, vol. 86, p. 6382, Dec. 1999.

[108] E. Y. Wu and J. Suñé, "Power-law voltage acceleration: A key element for ultra-thin gate oxide reliability," *Microelectronics Reliability*, vol. 45, pp. 1809–1834, Dec. 2005.

[109] K. P. Cheung, "Temperature effect on ultrathin SiO_2 time-dependent-dielectric-breakdown," *Applied Physics Letters*, vol. 83, p. 2399, Sept. 2003.

[110] E. Wu, J. Suñé, W. Lai, E. Nowak, J. McKenna, A. Vayshenker, and D. Harmon, "Interplay of voltage and temperature acceleration of oxide breakdown for ultra-thin gate oxides," *Solid-State Electronics*, vol. 46, pp. 1787–1798, Nov. 2002.

[111] E. Vincent, N. Revil, C. Papadas, and G. Ghibaudo, "Electric field dependence of TDDB activation energy in ultrathin oxides," in *Proceedings of the 7th European Symposium on Reliability of Electron Devices, Failure Physics and Analysis*, vol. 36, pp. 1643–1646, IEEE, 1996.

[112] J. W. McPherson, R. B. Khamankar, and A. Shanware, "Complementary model for intrinsic time-dependent dielectric breakdown in SiO_2 dielectrics," *Journal of Applied Physics*, vol. 88, p. 5351, Nov. 2000.

[113] C.-W. Wang, S.-F. Chen, and G.-T. Chen, "Gamma-ray-irradiation effects on the leakage current and reliability of sputtered TiO_2 gate oxide in metal-oxide-semiconductor capacitors," *Journal of Applied Physics*, vol. 91, p. 9198, June 2002.

[114] M. Kimura, "Oxide breakdown mechanism and quantum physical chemistry for time-dependent dielectric breakdown," in *1997 IEEE International Reliability Physics Symposium Proceedings. 35th Annual*, pp. 190–200, IEEE, 1997.

[115] R. Moazzami, J. Lee, and C. Hu, "Temperature acceleration of time-dependent dielectric breakdown," *IEEE Transactions on Electron Devices*, vol. 36, no. 11, pp. 2462–2465, 1989.

[116] J. W. McPherson and D. A. Baglee, "Acceleration Factors for Thin Oxide Breakdown," *Journal of The Electrochemical Society*, vol. 132, p. 1903, Aug. 1985.

[117] N. Klein and P. Solomon, "Current runaway in insulators affected by impact ionization and recombination," *Journal of Applied Physics*, vol. 47, p. 4364, Oct. 1976.

[118] I.-C. Chen and S. Holland, "Electrical Breakdown in Thin Gate and Tunneling Oxides," *IEEE Journal of Solid-State Circuits*, vol. 20, pp. 333–342, Feb. 1985.

[119] K. Schuegraf and H. Chenming, "Hole injection SiO_2 breakdown model for very low voltage lifetime extrapolation," *IEEE Transactions on Electron Devices*, vol. 41, pp. 761–767, May 1994.

[120] J. Lee, I.-C. Chen, and C. Hu, "Statistical modeling of silicon dioxide reliability," in *26th Annual Proceedings Reliability Physics Symposium 1988*, pp. 131–138, IEEE, 1988.

[121] D. B. Strukov, F. Alibart, and R. Stanley Williams, "Thermophoresis/diffusion as a plausible mechanism for unipolar resistive switching in metaloxidemetal memristors," *Applied Physics A*, vol. 107, pp. 509–518, Mar. 2012.

[122] C. V. Thompson, "Grain Growth in Thin Films," *Annual Review of Materials Science*, vol. 20, pp. 245–268, Aug. 1990.